Ana Paula Nascimento Fernandes

Master of Science in Biochemistry

LIVING CAPACITORS: FUNCTIONAL CHARACTERIZATION OF A NOVEL CYTOCHROME ACTING AS A NANOWIRE

Thesis submitted in partial fulfilment of the requirements for the degree of

Doctor of Philosophy in
Biotechnology

Supervisor: Carlos Alberto Gomes Salgueiro, Associate Professor with Habilitation, Faculdade de Ciências e Tecnologia da Universidade NOVA de Lisboa

Co-supervisor: Catarina Morais Vaz Paquete, Assistant Researcher, Instituto de Tecnologia Química e Biológica António Xavier/Universidade NOVA de Lisboa

Examination Committee:

Chairperson: Prof. Maria João Lobo de Reis Madeira Crispim Romão
Rapporteurs: Prof. Rui Manuel Pontes Meireles Ferreira de Brito
Prof. António Eduardo do Nascimento Ferreira

Members: Prof. Carlos Alberto Gomes Salgueiro
Prof. Américo José Gonzalez Duarte

FACULDADE DE CIÊNCIAS E TECNOLOGIA
UNIVERSIDADE NOVA DE LISBOA

September, 2019

LIVING CAPACITORS: FUNCTIONAL CHARACTERIZATION OF A NOVEL CYTOCHROME ACTING AS A NANOWIRE

To my son, my husband
and my parents

ACKNOWLEDGEMENTS

Science is a team effort and therefore, no PhD is the work of a single person.

In that sense, I express my appreciation to all the people that, in one way or another, helped me to reach this moment. Sometimes, in a hard path, being heard is all we need…

At the top of my gratitude, my supervisor Prof. Carlos Salgueiro and my co-supervisor Dr. Catarina Paquete. I thank you both for the opportunities, for the challenge, for the knowledge, for the availability, for the encouragement to follow different and, sometimes, unconventional directions, for the support and above all, for the enormous patience with me in these tough years, which yielded some accomplishments and countless frustrations…

I'm thankful to Dr. Ricardo O. Louro for helpful discussions, NMR lifesaving tutorials and for harboring me at the Inorganic Biochemistry and NMR Laboratory (ITQB). I would like to thank Dr. Isabel Couto for the opportunity in new directions. I thank Dr. David Turner for the assistance in NMR related calculations. I also thank Dr. Yuri Y. Londer and Dr. Marianne Schiffer from Biosciences Divison, Argonne National Laboratory (Argonne, IL, USA) for the coding plasmids and *E. coli* strain JCB7123; to Prof. Derek R. Lovley for the *G. sulfurreducens* PCA strain used for genomic DNA extraction and to Dr. Liang Shi and Dr. Johannes Gescher for *S. oneidensis* mutant strains used in expression tests.

I'm thankful to my colleagues Tiago Nunes, Marisa Ferreira and Liliana Teixeira for the sharing moments and for the highly needed companionship. I thank Mónica Alves, Inês Trindade, Marta Silva, Luis Rosa, Leonor Morgado, Tomás Fernandes, Názua Costa, Bruno Fonseca, Sónia Neto and Isabel Pacheco for all the support.

I'm grateful to the groups and research facilities that made this work possible – The Biochemistry and Bioenergetics of Heme Proteins Research Group, UCIBIO-REQUIMTE and LabRMN at FCT-UNL; IBN Laboratory and CERMAX at ITQB and Rede Nacional de RMN for access to the facilities.

I acknowledge the support and funding from the Fundação para a Ciência e Tecnologia through SFRH/BD/86439/2012 doctoral grant and from the PTDC/BBB-BQB/3554/2014 and UID/MULTI/04378/2013 projects, co-financed by ERDF through national funds under the Partnership Agreement PT2020 (POCI-01-0145-FEDER-007728).

I thank my friends Teresa, Pedro, Lucia and Vitor for the care, laughs and tears over the years... And to my dearest friends that have become bright stars in the sky and keep inspiring me – Paula and Ana. Miss you so much!

I am very grateful to my mom and dad – for care and support, for pushing me to do better, for being proud! Wish you were here!

I am thankful to my father-in-law and my mother-in-law, Artur and Clara, for all the concern and affection.

My deepest gratitude goes to those that kept me floating, even in the darker moments – my dearest son Henrique and my dearest husband Paulo. Thank you for all the encouragement, for the unconditional support, for your patience and especially for your love! This almost never ending story has come to an end thanks to you and your persuasive power… Thank you for believing!

And finally, to Keanu and Jackie, that are always here for me without questioning, just caring…

ABSTRACT

In an Era where environmental issues are a growing concern, microorganisms that have remarkable features, such as extracellular electron transfer (EET) ability, present major opportunities in diverse biotechnological fields. *Geobacter* bacteria have shown an extraordinary respiratory flexibility, with its dissimilatory metal reduction ability and EET to electrode surfaces, and numerous *c*-type cytochromes were pointed as key players. However, the understanding of the mechanisms involved and hence, the advances in practical applications, are still in its early days and it is crucial to move further and unveil not only the components involved, but also their roles and partners in electron transfer.

The dodecaheme GSU1996, composed of four similar triheme domains (A–D), was proposed to work as a natural nanowire, owing to its linear structure and large number of hemes. In this work, the *in vitro* functional characterization of the GSU1996 was attempted, in a modular characterization based strategy. Here, the triheme domains C and D assisted in the characterization of the C-terminal end of GSU1996, the hexaheme fragment CD. The first step encompassed the assignment of the heme groups signals in the nuclear magnetic resonance spectra of the triheme domains and of the hexaheme fragment, which is the protein with the highest number of hemes assigned to date. The second step comprised the determination of the microscopic thermodynamic parameters of fragment CD. This provided mechanistic information on the dominant microstates and included the determination of the reduction potentials of the hemes, redox interactions between hemes and ionizable centers and among neighboring hemes. The third and final step consisted in the determination of the microscopic kinetic parameters of fragment CD. This unveiled details about the reactivity of the heme groups and included the calculation of the reference rate constants for each heme in the reduction/oxidation process. All combined, the data revealed that a heme located at the end of the C-terminal edge of GSU1996 shows the necessary skills to accept electrons from redox partners.

In vitro interaction studies performed between GSU1996 and the periplasmic cytochrome PpcA and its homologues (PpcC–E), revealed that it is possible that GSU1996 and PpcA may be redox partners in *G. sulfurreducens*, as they form a transient redox complex that involves the C-terminal fragment of GSU1996.

Work has also been started to disclose other electron transfer components of *G. sulfurreducens*, namely, the outer membrane tetraheme cytochrome OmcE; the hexaheme OmcS and the nanowire cytochrome GSU2210. New constructs and expression systems were tested, based in the pBAD vector, albeit none of the attempts have been successful.

Although *in vitro* studies provide information and allow the evaluation of the functional properties of these proteins, *in vivo* studies are essential to assess the actual roles and interacting partners in the cells. Therefore, a novel approach was also tested towards the *in vivo* labeling of *c*-type cytochromes, based in the attachment of a tetracysteine tag that is fluorescent upon binding with commercially available biarsenical dyes. However, no expression of the model tagged protein was accomplished.

Keywords: *Geobacter sulfurreducens*; GSU1996 nanowire *c*-type cytochrome; Electron transfer; Nuclear Magnetic Resonance

RESUMO

Numa Era em que as questões ambientais são uma preocupação crescente, os microrganismos com características distintivas, como a capacidade de realizar transferência electrónica extracelular (TEE), representam oportunidades de avanço em diversos campos biotecnológicos. As bactérias do género *Geobacter* apresentam uma flexibilidade respiratória extraordinária, devido à capacidade de redução dissimilativa de metais e de TEE para superfícies de eléctrodos, na qual foram implicados vários citocromos *c* como elementos-chave. Contudo, a compreensão dos mecanismos envolvidos e, logo, as aplicações práticas, ainda se encontram numa fase embrionária. Assim, é essencial incrementar a informação disponível de modo a revelar os componentes envolvidos, bem como as suas funções e parceiros nos mecanismos de transferência electrónica.

Ao citocromo dodeca-hémico GSU1996, constituído por quatro domínios tri-hémicos semelhantes (A–D), foi associada a função de nanofio natural de hemos, devido à sua estrutura linear e ao elevado número de grupos hemo. Neste trabalho, foi realizada a tentativa de caracterizar o GSU1996 com base numa estratégia de caracterização modular. Os domínio tri-hémicos C e D guiaram a caracterização da região C-terminal do GSU1996, o fragmento hexa-hémico CD. O primeiro passo consistiu na atribuição dos sinais nos espectros obtidos por Ressonância Magnética Nuclear aos grupos hemo dos domínios e de seguida, do fragmento. O fragmento CD é, até à data, a proteína com o maior número de grupos hemo cujos sinais foram atribuídos. Num segundo passo, determinaram-se os parâmetros termodinâmicos microscópicos do fragmento, que providenciaram informação mecanicista acerca dos microestados dominantes e que incluiu o cálculo dos potenciais de redução de cada grupo hemo, das interacções redox-Bohr e entre grupos hemo. O passo final compreendeu a determinação dos parâmetros cinéticos microscópicos do fragmento e revelou detalhes sobre a reactividade dos grupos hemo, incluindo o cálculo das constantes de velocidade para cada grupo hemo no processo de redução/oxidação. Globalmente, os dados mostram que um grupo hemo na região C-terminal do GSU1996 tem as propriedades necessárias para aceitar electrões de parceiros redox.

Estudos de interacção *in vitro* entre o GSU1996 e o citocromo periplasmático PpcA e seus homólogos (PpcC–E), revelaram que entre o PpcA e o GSU1996 se forma um complexo transiente que envolve a região C-terminal deste, podendo ser parceiros redox em *G. sulfurreducens*.

Iniciou-se também o estudo de outros componentes das cadeias de transferência electrónica de *G. sulfurreducens*, nomeadamente dos citocromos OmcE (membrana externa), OmcS (que compõe os pili) e GSU2210 (nanofio). Testaram-se plasmídeos e sistemas de expressão baseados no vetor pBAD, embora nenhuma das tentativas tenha sido bem sucedida.

Embora os estudos *in vitro* permitam a avaliação das propriedades funcionais, é crucial estabelecer *in vivo* quais as actuais funções e parceiros das proteínas nas células. Assim, testou-se uma nova abordagem para marcação de citocromos *c in vivo*, baseada na expressão da proteína com um motivo de tetracisteínas na região C-terminal. Esta fluoresce após ligação a reagentes comerciais, como FlAsH-EDT_2 ou ReAsH-EDT_2. No entanto, não foi conseguida expressão com o citocromo modelo.

Palavras-chave: *Geobacter sulfurreducens*; Citocromos *c* tipo nanofio; Transferência electrónica; Ressonância Magnética Nuclear

CONTENTS

LIST OF FIGURES

CHAPTER 1

CHAPTER 2

CHAPTER 3

CHAPTER 4

CHAPTER 5

CHAPTER 6

LIST OF TABLES

CHAPTER 1

CHAPTER 3

CHAPTER 4

CHAPTER 5

CHAPTER 6

ABBREVIATIONS AND SYMBOLS

1D – One-dimensional

2D – Two-dimensional

AQDS – Anthraquinone-2,6-disulfonate

ATP – Adenosine triphosphate

BES – Bioelectrochemical system

CbcL – *c*- and *b*-type cytochrome for low potential

COSY – Correlation spectroscopy

Cys – Cysteine

DIET – Direct interspecies electron transfer

DMR – Dissimilatory metal reduction

DMRB – Dissimilatory metal reducing bacteria

EDTA – Ethylenediaminetetraacetic acid

EET – Extracellular electron transfer

EXSY – Exchange spectroscopy

$FADH_2$ – Reduced flavin adenine dinucleotide

Gly – Glycine

His – Histidine

HMQC – Heteronuclear multiple quantum correlation spectroscopy

HP – His-patch

HSQC – Heteronuclear single quantum correlation spectroscopy

ImcH – Inner membrane *c*-type cytochrome

IUPAC – International Union of Pure and Applied Chemistry

MacA – Metal reduction associated cytochrome

MDC – Microbial desalination cell

MEC – Microbial electrolysis cell

MES – Microbial electrosynthesis cell

Met – Methionine

MFC – Microbial fuel cell

MHC – Multiheme *c*-type cytochrome

MRC – Microbial remediation cell

MXC – Microbial electrochemical system

NADH – Reduced nicotinamide adenine dinucleotide

NaPi – Sodium phosphate

NBAF – Acetate-fumarate medium

NDH I – NADH dehydrogenase complex I

NMR – Nuclear magnetic resonance

NOE – Nuclear Overhauser effect

NOESY – Nuclear Overhauser spectroscopy
ORF – Open reading frame
PDB – Protein data bank
Phe – Phenylalanine
PpcA-E – Periplasmic *c*-type cytochrome A-E
Pro – Proline
Q – Menaquinone
QH_2 – Menaquinol
RMSD – Root-mean-square deviation
SDS-PAGE – Sodium dodecyl sulfate-polyacrylamide gel electrophoresis
SHE – Standard hydrogen electrode
spp. – Species
STC – Small Tetraheme Cytochrome
TOCSY – Total correlation spectroscopy
Tyr – Tyrosine

Å – Ångström
^{1}H – Proton, Hydrogen-1 nuclei
^{13}C – Carbon-13 nucleus
^{15}N – Nitrogen-15 nucleus
$^{2}H_2O$ – Deuterium oxide
kHz – Kilohertz
mAu – Milli absorbance units
meV – Millielectron volt
MHz – Megahertz
mM – Millimolar
mV – Millivolt
ppm – Parts per million
µM – Micromolar

CHAPTER 1

INTRODUCTION

Contents

ON THE QUEST FOR SUSTAINABILITY: ENVIRONMENTAL BIOTECHNOLOGY

Biotechnology primarily emerged as the incorporation of the processes performed by natural biological systems to achieve desired purposes (1). More recently, a new approach has emerged in the form of Environmental Biotechnology, which combines the application of diverse branches of science, such as animal and plant sciences, chemical engineering, genetics, molecular biology, microbiology and biochemistry to answer environmental issues and requirements, in fields such as agriculture, resource preservation, environmental conservation, waste management and pollution prevention and bioremediation (2,3). Consequently, Environmental Biotechnology arises as a propelling force for a sustainable growth, crucial for mankind welfare and prosperity over future generations (3).

Biogeochemistry encompasses the study of the complex processes that underlie the flow and distribution of chemical elements throughout living organisms and their environments (4). In this context, biogeochemical cycles cover the qualitative and quantitative comprehension of the migration and conversion of substances within natural and man-made environments, as the case of prime elements such as carbon, nitrogen or phosphorous (4). These are frequently mediated by microorganisms, for instance, *Archaea* and *Bacteria* (5). Indeed, complex microbial communities that populate soils, waters and sediments play major roles in the transformation and recycling of organic and inorganic compounds in order to sustain the biosphere (5). However, there is still a large void in the understanding of the fundamental mechanisms that trigger these microbially mediated reactions, either from relatively well studied processes such as photosynthesis or respiration, or from more unusual ones, as the extracellular electron transfer (EET) mechanisms that allow for the dissimilatory metal reduction (DMR) and direct interspecies electron transfer (DIET) processes (5).

The convergence of Biogeochemistry and Environmental Biotechnology is inevitable and only multidisciplinary data will open routes to the successful understanding of biosphere mechanisms and its practical implementation towards meeting human needs and keeping environmental homeostasis (5). Therefore, in order to carry out biotechnological enterprises based in the effective large multipowering microbial communities with environmental and industrial scale sustainability, it is imperative to provide such level of primary details. This will contribute to the conception of new applications and improve the already existing ones, that are still limited to laboratory and small-scale technologies (5).

BIOELECTROCHEMICAL SYSTEMS

Research in microbial systems have demonstrated the real-world utility of electron transfer mechanisms evolved by microorganisms to interact with the environments (6). As an example, Fe(II)-oxidizing microorganisms are already employed at an industrial scale in the biomining of ores, as in the extraction of gold, copper, nickel, and zinc (7,8).

Microbial EET directed towards the oxidation of Fe(II) or reduction of minerals such as Fe(III), Se(IV)/Se(VI) or Pd(II) (9–12) are promising in the production of Fe(III), Fe(II), Se(0) and Pd(0) biogenic nanomaterials that can be employed in industry as catalysts and semiconductors, in the bioremediation

of soil and water contaminants and even in medical fields such as in cancer treatment procedures (10,11,13).

Electrodes are also suitable for microorganisms both as electron donors (cathodes) and electron acceptors (anodes) (14,15). Bioelectrochemical systems (BESs) may occur as microbial fuel cells (MFCs, Figure 1.1), where electrons are harvested from microorganisms to produce electricity, or as microbial electrolysis cells (MECs, Figure 1.2), in which power is used to feed microorganisms to promote electricity-driven synthesis (15).

In MFCs, chemical energy enclosed in organic matter present in wastewaters can be converted to electricity (16). In this case, Fe(III)- and Mn(IV)-reducing microorganisms such as *Shewanella* and *Geobacter* spp. carry out the oxidation of organic compounds and perform EET to the surface of an electrode with the concomitant electricity generation (14,17). So far, these systems meet the energy demands for low-power devices (18), although advances are on the way towards scaling up apparatuses (19–21). In mixed cultures setups that include methanogens, methane biofuel may as well be obtained (22,23).

Exoelectrogen microorganisms are able to directly or indirectly transfer electrons onto the surfaces of electrodes in MFCs, by means of *c*-type cytochromes or pili or by electron shuttles, e.g., flavins or pyocyanin, respectively (24). They can form electroactive biofilms and produce an exopolysaccharide matrix and cyclopropane fatty acids that allow the surface charge modification and creates anchor points for *c*-type cytochromes (24). In the case of *Shewanella oneidensis*, flavin-cytochrome complexes are used to promote electron transfer to electrodes, while *Geobacter sulfurreducens* relies on pili and *c*-type cytochromes for this purpose (24).

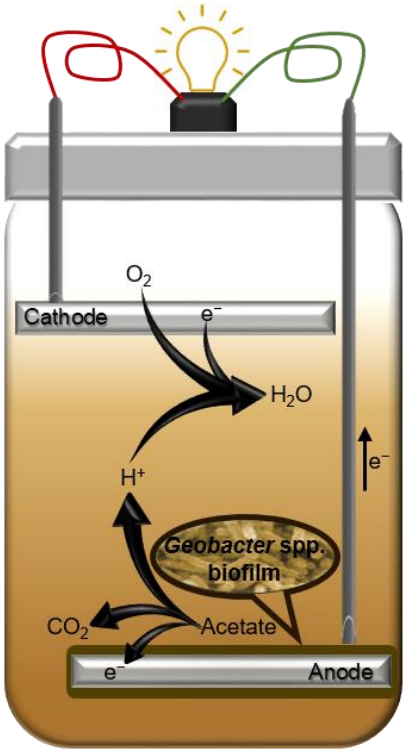

Figure 1.1 – Illustration of a soil MFC. Adapted from Wikimedia Commons/MFCGuy2010, available in https://en.wikipedia.org/wiki/File:SoilMFC.png.

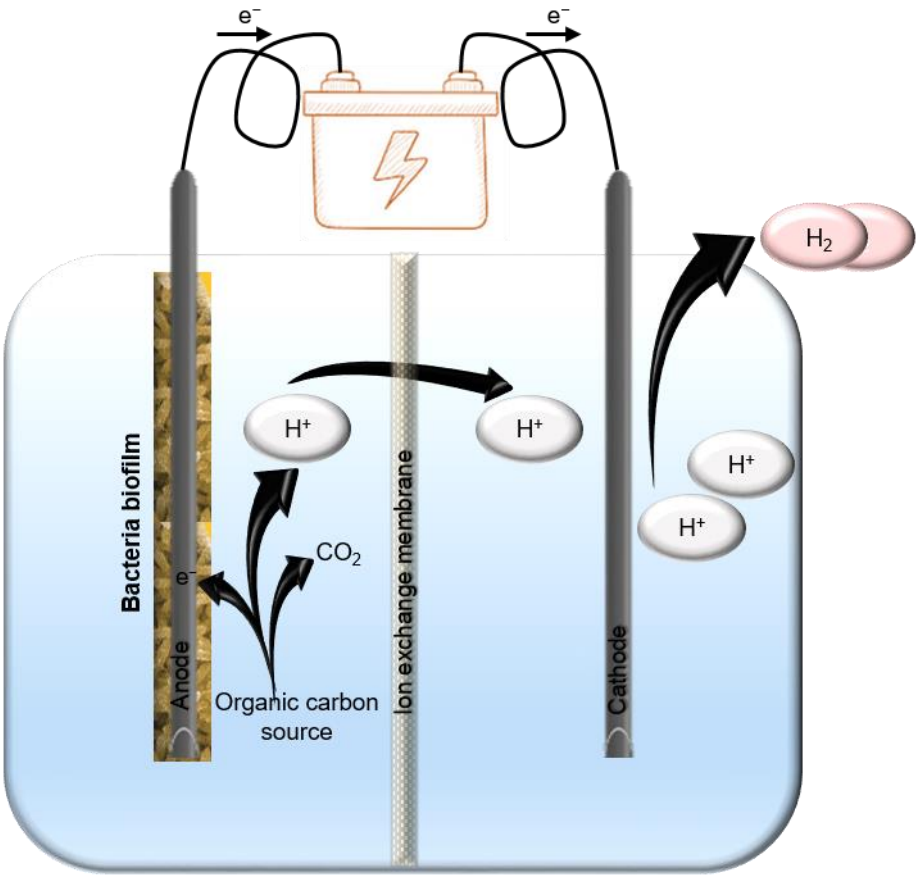

Figure 1.2 – Schematic representation of a MEC.

When electrons are provided to *G. sulfurreducens*, this bacterium is able to apply it in the reduction of protons to H_2 (25) and this microorganism can be explored as self-renewable and low-cost catalyst in hydrogen production (26).

In mixed microbial communities from natural and/or laboratory sources, *Geobacter* and akin species are usually the top colonizers found in electrodes, particularly in anaerobic growth conditions (26). Indeed, the larger current densities in microbial fuel cells were observed with *Geobacter* spp. (26). *Geobacter* spp. are also of interest in the field of bioelectronics, as electroactive biomaterials are innocuous and can be produced from rather economical raw materials and also by the indirect application of such abilities in the design of new and more efficient biomimetic systems (27). In this sense, increase of the current output and added-values production may be achieved by strain selection or engineering (28,29) or by improvements in microbial fuel cells, such as anode surface alteration with nanoparticles or by novel designs (19,24). Therefore, one of the constraints in scaling-up is the current knowledge on microbial electron transfer chains.

In light of recent findings, microbial electrosynthesis processes have also been probed (15). In microbial electrosynthesis processes, microorganisms are used as biocatalysts, where oxidizing or reducing power is used to drive biochemical reactions, such as in the oxidative production of ethanol from glycerol (30) or the reductive conversion of CO_2 to acetate or from fumarate to succinate (15,31,32).

Illustrations of the microbial reduction abilities displayed by various microorganisms are outlined next, together with a brief state of the art around the microbial electron transfer mechanisms underlying it and some examples of their practical applications.

Dissimilatory metal reduction

Diverse *Archaea* and *Bacteria* are able to use metals and other compounds as electron acceptors in anaerobic respiration without performing uptake and/or incorporation directly into cell components (33). This is called DMR, where microorganisms conserve energy from the oxidation of aromatic molecules, organic acids, alcohols and/or H_2 and couple it to the reduction of metals in the course of non-assimilatory metabolic activities (33–35). DMR plays major roles in the biogeochemical cycles of a wide range of organic and inorganic compounds in different environments, from ground to underground soils and waters. It also establishes the foundations towards the development of new and improved pioneering biotechnological applications in fields such as bioremediation or bioenergy production (34,36).

The full molecular mechanisms that underlie the respiratory reduction of metals are still to unveil, and it is expected that the availability of more complete genome sequences from DMR organisms together with genomic and proteomic advances may shed light into these processes (36).

Metals – Iron and Manganese

Iron tends to coordinate with organic and inorganic ligands to originate a large number of different minerals that have key roles in environmental chemistry owing to their high reactivity (37). In physiological conditions, iron is usually found in the oxidized ferric – Fe(III) – and in the reduced ferrous – Fe(II) – redox states and may be in high or low spin states according to its ligands. Its chemistry may also vary with the pH and with the temperature, among other factors (37,38).

The natural abundance of iron on planet Earth and its versatile properties may have elected this element as the ideal candidate for the incorporation in biomolecules from early periods and along life's evolutionary stages (39). Indeed, iron acts as a cofactor in many proteins as mono- or binuclear species or incorporated in heme groups or iron-sulfur clusters as a biocatalyst or electron transporter (38). Under specific local environment, its geometry, spin state and redox potential (extending from −300 to +700 mV) can be modelled within particular ranges headed for its biological purposes (38). These roles are played in numerous primary processes such as gene regulation and DNA synthesis, respiration, photosynthesis, oxygen transport and methanogenesis (38).

Globally, the dissimilatory Fe(III) reduction presents a higher influence in the environmental ecology than other metals reduction (34) as it performs major roles in processes as the decomposition of organic matter and contaminating aromatic compounds; in the formation of magnetite – Fe_3O_4 ($Fe^{2+}O.Fe^{3+}{}_2O_3$) – in aquatic sediments and its increase around hydrocarbon seeps; in the generation of siderite – $Fe^{2+}CO_3$ – and vivianite – $Fe^{2+}Fe^{2+}{}_2(PO_4)_2{\cdot}8H_2O$ –; in the accumulation of high amounts of iron in deep aquifers and steel corrosion; in the release of phosphate and trace minerals to water sources, and in the regulation of methane generation in shallow waters (34,40).

In sedimentary environments, amino acids and sugars are metabolized by diverse microorganisms with the release of the standard prime products of fermentation – acids and alcohols and molecular hydrogen (41,42). Fermentation products, such as acetate, formate and H_2, can then be used by Fe(III)-reducing microorganisms as *Geobacter*, *Shewanella* and *Desulfuromonas* species to conserve the necessary energy to support growth with the Fe(III) reduction to Fe(II) (43–45). Although Fe(III)-reducing microorganisms environmental distribution is not yet well known, many reports revealed that *Geobacteraceae* family constitutes a main piece of these subsurface communities (33,46). *Geobacter metallireducens* GS-15 is able to couple the oxidative degradation of aromatic hydrocarbon pollutants, as the cases of phenol, toluene and benzene, to the reduction of Fe(III) (47). The oxidation of acetate by *G. sulfurreducens* PCA can also be coupled to the reductive dechlorination of trichloroethene by *Desulfitobacterium* and *Dehalococcoides* spp. by means of electrically conductive minerals, such as magnetite (48).

Under anaerobic conditions, *S. oneidensis* MR-1 reduces Fe(III) to Fe(II) and in aerobic conditions it is able to produce hydrogen peroxide (H_2O_2) (49). Interestingly, in the Fenton reaction Fe(II) reacts with H_2O_2 to reoxidize iron and produce hydroxyl ions (OH^-) and radicals ($HO^\bullet$). These radicals can oxidize several organic toxic compounds, as 1,4-dioxane, which is used as a stabilizer for chlorinated industrial solvents and also produced as a by-product of plastic manufacturing industries (49). Hence, a bioremediation strategy that couples lactate oxidation to 1,4-dioxane oxidative degradation can be successfully carried by switching between *S. oneidensis* MR-1 aerobic and anaerobic growth (49).

The majority of the microorganisms that act in Fe(III) reduction processes are also skilled to sustain growth via Mn(IV) to Mn(II) reduction (50) and this occurs either by direct reduction mechanisms departing from similar electron donors or as an indirect side-reaction performed by Fe(II) that originates from Fe(III) reduction mechanisms (34,45,51). Nonetheless, Mn(IV) is more prone to be reduced by nonenzymatic mechanisms than Fe(III) (40). As in the Fe(III) case, Mn(IV) reduction can be important at the levels of the decomposition of organic matter and contaminating aromatic compounds, in the generation of manganese minerals and in the release of trace metals from manganese oxides (40).

Although Fe(III) and Mn(IV) reduction mechanisms are of major environmental significance, these processes may likewise have a negative effect in the biogeochemistry if toxic levels of Fe(II) and Mn(II) and other bound trace minerals are released (33).

Metals radionuclides – Uranium, Neptunium, Plutonium and Technetium

While nuclear technology moves further, it leaves a superfluous trail of radionuclides in the environments that largely exceeds natural radioactivity sources and overwhelms its removal mechanisms.

Reduction of the soluble U(VI) (uranyl ion; UO_2^{2+}) to its precipitated form U(IV) (uraninite; UO_2) represents an important step in the biogeochemical cycle of uranium and in the decontamination of natural environments (52–54). Generally, in natural water environments, U(VI) is found as uranyl-carbonate complexes (55), that are also the usual dissolved forms of anthropogenic origin (56). *G. metallireducens* and *S. oneidensis* MR-1 have been shown to be able to use such complexes as

external electron acceptors to conserve energy for anaerobic growth with the extracellular precipitation of uraninite (34,57–59) (Figure 1.3).

Although *Desulfovibrio desulfuricans*, *Desulfovibrio vulgaris* and *Clostridium* spp. are able to reduce uranium, they cannot conserve energy for growth from this process. *In vitro* studies showed that in *D. vulgaris* this can be performed by the tetraheme cytochrome c_3 with electrons donated by its physiological partner hydrogenase. *In vivo* studies with a *D. desulfuricans* cytochrome c_3 mutant corroborated its involvement in U(VI) reduction, and also pointed for the existence of alternative routes for this reduction to occur (60).

The removal of the soluble U(VI) with the aid of microorganisms presents benefits over other means of decontamination, such as the recovery of this metal in an extremely pure and concentrated form with high yields; its precipitation from carbonated complexes; the potential for *in situ* bioremediation of contaminated areas and the possibility of simultaneously decontaminate organic and U(VI) compounds by coupling the oxidation of the former with the reduction of the latter (34,61).

The extremely soluble Np(V) (NpO_2^+) can also be reduced to the soluble form Np(IV) by *S. oneidensis* MR-1, that can then be transformed into an insoluble phosphate biocomplex by *Citrobacter* sp. aimed at its easier removal (62). It is possible that Pu(IV) may be amenable for reduction by Fe(III) reducing organisms such as *Geobacter* spp., but Pu(III) may also be susceptible of spontaneous reoxidation (63).

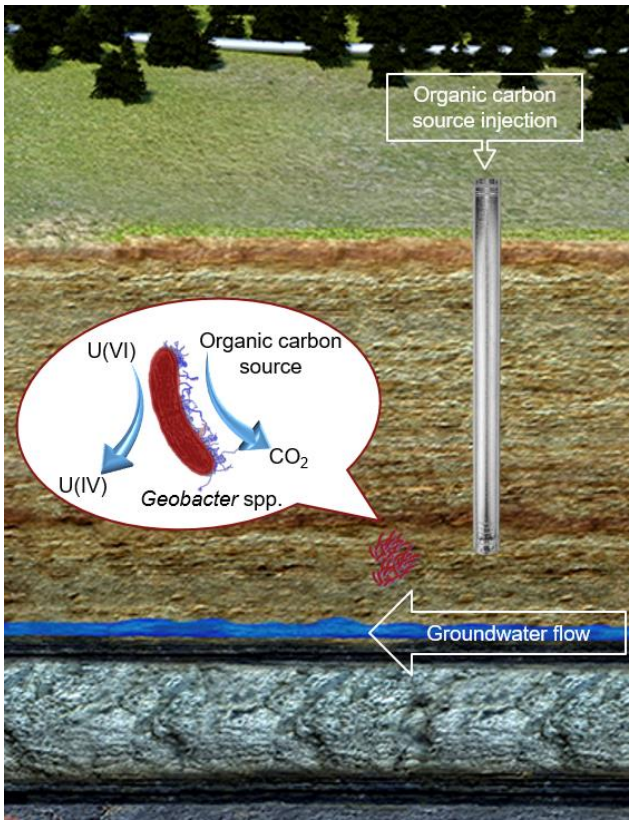

Figure 1.3 – An *in situ* uranium bioremediation strategy with resource to *Geobacter* spp.. Adapted from US Department of Energy, Genomics:GTL Roadmap (p. 219).

The soluble and mobile Tc(VII) (pertechnetate, TcO_4^-) can be bioreduced to its insoluble form Tc(IV) by microorganisms belonging to *Geobacter* spp. or *Escherichia coli* (64,65). In the last case, electrons from formate or H_2 flow to Tc(VII) in a reaction catalyzed by hydrogenase 3 from a formate hydrogenlyase complex (64). In the sulfate reducing bacterium *D. desulfuricans*, a formate dehydrogenase coupled to a hydrogenase via a cytochrome can also use formate to precipitate Tc(IV) in the periplasm (36). In *Desulfovibrio fructosovorans*, the periplasmic Ni-Fe hydrogenase was likewise shown by genetic studies to play a role in Tc(VII) reduction (66).

Other metals – Silver, Mercury, Cobalt, Chromium, Copper, Gold, Vanadium, Molybdenum, and Palladium

The reduction of Ag(I) has been associated to the resistance ability to the metal in several microorganisms (67). In some cases, it was reported the reduction of Ag(I) to Ag(0) after its biosorption to the surface of the cells (e.g. *Lactobacillus* sp.) (68). Another metal resistance example is that of mercury, usually encoded in a *mer* resistance operon that enables the transport of Hg(II) to the interior of the cells by the MerT transporter protein, where it is reduced by the intracellular mercuric reductase MerA to the comparatively non-hazardous and volatile elemental mercury (69). In *G. metallireducens*, *c*-type cytochromes that reduce Hg(II) were described (43) and in *Thiobacillus ferrooxidans* a mechanism that depends on Fe(II) and may involve cytochrome *c* oxidase was also reported (70), although no evidence supports cellular growth. Practical uses can easily be pointed in the bioremediation of mercury contaminated environments and in the conception of Hg(II) biosensors (35).

Radioactive cobalt-60 is a challenging contaminant as its strong association with ethylene diamine tetraacetic acid (EDTA) makes it highly mobile. Fe(III)-reducing microorganisms, such as *G. sulfurreducens*, have the ability to reduce Co(III) to Co(II) that does not complex so easily with EDTA and can be immobilized *in situ* as it remains absorbed to the contaminated soils (33,71).

Although chromium is necessary in trace amounts for organisms to perform metabolic processes, as in lipid metabolism for instance, Cr(VI) contamination is a growing problem as chromium became widely employed in industry (72). The highly toxic and mobile Cr(VI) can be reduced to the less toxic and soluble form Cr(III) by several microorganisms, such as *S. oneidensis* MR-1 and *E. coli*, with higher activity in anaerobic conditions (72). In co-cultures of *Pseudomonas putida* DMP-1 and *E. coli* ATCC 33456, the simultaneous decomposition of aromatic compounds by the former was coupled to the reduction of Cr(VI) by the latter (73). In *Pseudomonas ambigua* G-1 and *P. putida* DMP-1, NAD(P)H-dependent reductases have been associated to aerobic reduction of chromium (74,75). Both in *Pseudomonas* and *Shewanella* it was observed that the reduction of Cr(VI) appears to start by one-electron transfer from the reductase, with the formation of the intermediate Cr(V) (75,76). Cytochromes have also been enrolled in Cr(VI) reduction, as is the case of cytochrome c_3 from *D. vulgaris* (77), cytochrome *c* from *Enterobacter cloacae* (78) and cytochromes *b* and *d* from *E. coli* (79).

Several Fe(III)-reducing *Bacteria*, such as *Thermotoga maritima*, *Shewanella algae* and *Geovibrio ferrireducens*, and *Archaea*, as the cases of *Pyrobaculum islandicum* and *Pyrococcus furiosus*, inhabit sediments that harbor gold deposits and are able to reduce soluble Au(III) to its insoluble Au(0) form (80). While in *G. ferrireducens* Au(0) precipitates in the periplasm, in the majority of the species this

occurs on the surface of the cells (80). The necessity of hydrogen as electron donor pointed in the direction that a hydrogenase could play a role in Au(III) reduction, as observed in metals for other cases (36,64). In *G. metallireducens* it was hypothesized that *c*-type cytochromes were responsible for this electron transfer (43).

It is possible that the reduction of V(V), an ability that appears to be generalized among soil bacteria and fungi (81), leads to its environmental sedimentation in anaerobic conditions and can be explored to bioremediate ore-processing wastes (82). It was found that *G. metallireducens* is able to conserve energy for growth from the oxidation of acetate coupled to the reduction of V(V) to V(IV) (82). Work with *Pseudomonas vanadiumreductans* and *Pseudomonas isachenkovii* showed that with diverse electron donors such as H_2, sugars and amino acids, anaerobic cells were able to promote the reduction of V(V) to V(IV) (blue colored) and probably to V(III) (black colored precipitate) (83).

The biogeochemical cycle of molybdenum may be affected by Mo(VI) microbial reduction, e.g., by means of the ore leaching that occurs under acidic reduction environment (34) and by the variation in the concentration of insoluble molybdenum in active reduction rocks sites and anoxic marine sediments under nearly neutral reduction conditions (84,85). *T. ferrooxidans* and the thermophilic acidophiles *Sulfolobus acidocaldarius* and *Sulfolobus brierleyi* were reported to be able to couple elemental sulfur oxidation to Mo(VI) reduction (86,87).

The microbial reduction of the soluble Pd(II) to its insoluble form Pd(0) is commercially relevant, as it allows the recovery of palladium from industrial catalysts and the development of bioinorganic nanocatalysts (33). Early studies with *D. desulfuricans* enrolled a periplasmic hydrogenase in the reduction of Pd(II) (88). Studies on the delivery of reducing power to an immobilized biocatalyst in bioreactors have also been performed with biofilms of *D. desulfuricans* in a Pd-Ag membrane that provided atomic hydrogen to the cells (89). Pd(0) biorecovered in this clean and affordable process was shown to be a more effective catalyst that its chemical counterpart, with no secondary wastes produced (89).

Metalloids – Arsenic, Selenium and Tellurium

In oxidized environments, arsenic occurs as the arsenate anion As(V) that is tightly bound to sediments, but in anaerobic conditions it is reduced to the more toxic and mobile As(III) (90). It was suggested that in West Bengal sediments *Geobacter* spp. may perform leading roles in microbially mediated arsenic release from metal hydroxides that occurs after Fe(III) reduction (91). In fact, these microorganisms are capable to thrive in such toxic environments due to the existence of genes that code for an arsenic detoxification system (*ars* operon) (92). In several species, genes necessary for arsenic respiration (*arr* operon) and arsenic methylation (*ars*M) were also identified (92).

Some of the microorganisms known to be able to grow by dissimilatory reduction of As(V) are the strict anaerobe *Chrysiogenes arsenatis* (93) and the Gram-negatives microaerophilic sulfur-reducing bacteria *Sulfurospirillum arsenophilum* and *Sulfurospirillum barnesii* (94). In *C. arsenatis* this type of respiration is supported by a periplasmic arsenate reductase composed by Mo, Fe, S and Zn cofactors (95).

In nature, the metalloid selenium is essentially present as Se(VI) (selenate, SeO_4^{2-}), as Se(IV) (selenite, SeO_3^{2-}), Se(0) (elemental form) and Se(−II) (selenide) (96). Bioremediation of waters contaminated by toxic Se(VI) and Se(IV) to its elemental form can be achieved by organisms such as *Thauera selenatis*, that is able to conserve energy from growth with selenium. This organism was shown to bear a periplasmic complex reductase that contains molybdenum, iron and acid-labile sulfur (97).

The resistance mechanisms to the toxic oxyanion tellurite (TeO_3^{2-}), that acts as an antibiotic, have been studied and basal levels of resistance in *E. coli* include its reduction by the activity of a membrane bound nitrate reductase (98).

AN OVERVIEW INTO EXTRACELLULAR ELECTRON TRANSFER MECHANISMS

Microorganisms have evolved different strategies to perform the transfer of electrons from the microbial intracellular redox transporters to the external electron acceptors and vice-versa. This process is denoted as microbial EET. In order to perform EET, microorganisms need to overcome the constraints imposed by the cytoplasmic membrane, the first barrier to external hazards and the main electron transfer center in energy generation. They also need to overwhelm other existing external structural components, as the outer membrane or peptidoglycan that do not allow the entrance of the majority of organic and inorganic compounds and are electrically nonconductive (6,99,100).

Several microorganisms are able to use soluble metal compounds and minerals as electron donors, as in the case of Fe(II) oxidizing bacteria, that is coupled to the reduction of terminal acceptors such as oxygen in the case of aerobes, or nitrate in case of anaerobes as *Dechloromonas* spp.. Electrons that arise from Fe(II) oxidation on the cell surface are carried across the periplasm to the cytoplasmic membrane in order to assist in the reduction of NAD^+ and in the generation of a proton motive force for ATP synthesis (101).

Microorganisms also use carbon sources as electron donors, which are oxidized in the cytoplasm and give rise to reduced NADH or $FADH_2$. In the cytoplasmic membrane, electron carriers are oxidized and protons are transported across the membrane with the concomitant generation of a proton motive force that is applied for the synthesis of ATP. Electrons piled in the periplasm are transferred extracellularly across the cell surface (outer membrane in Gram-negative bacteria and cell wall in Gram-positive bacteria) (101). Some bacteria are able to contact directly with the external electron acceptors through multiheme *c*-type cytochromes (MHCs) in the outer membrane or pili to perform electron transfer (102). Others transfer electrons at a distance, by means of the release of chelators that trap electron acceptors and bring them into the cell for reduction purposes (103) or by the use of extracellular electron shuttles that transfer electrons from the cell towards the extracellular electron acceptors (104).

The case of the metal reducing *G. sulfurreducens* will be outlined in the next section, together with known details about the microorganism electron transfer chains.

BRIDGING THE GAPS: *GEOBACTER* SPP. CONTRIBUTION

Geobacter species have been studied as model organisms in electron transfer mechanisms, specially *G. sulfurreducens* (71), as they are relatively amenable for laboratory purposes, from culture handling to genetic manipulation and physiological analyses (105–109).

Geobacter spp. are Gram-negative δ-proteobacteria shaped rods, whose trademark feature is their proficiency towards the complete oxidation of acetate – a crucial intermediary in the anaerobic degradation of organic matter – coupled to the reduction of extracellular Fe(III) soluble and insoluble forms, in a way that provides energy conservation for cellular growth (110). Acetate is oxidized via tricarboxylic acid cycle and the genomes of diverse *Geobacter* spp. present highly conserved genes for its metabolism (105).

They form the predominant microbial communities in diverse anaerobic natural environments where iron reduction processes play a key role, as water sediments, flooded rice fields and underground habitats where they are protagonists in its biogeochemistry (40,43,71). Probably, the foundations for this prevalence rely on *Geobacter* spp. distinctive mechanisms concerning Fe(III) and Mn(IV) reduction (111), during which they straightforwardly locate and directly interact with the metal oxides (112,113). Other advantages may arise from their capability to oxidize to completion various organic compounds with diverse electron acceptors (26,114) towards rapidly populate anaerobic environments (115). Their low maintenance energy requirements (116) and even their ability to momentarily sustain metabolic activities in starvation conditions (117,118) may also contribute to this preponderance. Interestingly, *Geobacter* spp. are also able to fix nitrogen (119) and they can thrive in oxidative stress conditions, as they are equipped with a number of mechanisms that allow for their survival in such adverse environments (120).

In addition to the several electron donors/acceptors supported by *Geobacter* spp. (Table 1.1), they can also exchange electrons with other syntrophic species. Indeed, association between *G. sulfurreducens* and *G. metallireducens* and between *Geobacter* spp. and methanogens were reported (22,23,121,122).

A remarkable characteristic of *Geobacter* spp. is the high number and diversity of *c*-type cytochromes encoded in its genomes. In fact, it was reported, from a comparison of six different *Geobacter* genomes, an average of 79 *c*-type cytochromes per genome, many of them with multiple hemes (105).

They are consistently kept in high abundance along the different species but, although essential for EET, these cytochromes show low level of conservation which may indicate different routes for electron transfer across the cells. Indeed, only nine protein families were found to be conserved. One of these contains the triheme c_7 cytochrome PpcA and it was found that it bears more than one homologue in several of the genomes studied and another four of these families may code simultaneously for a quinone:ferricytochrome *c* oxidoreductase (105).

Beyond the EET role, an additional hypothesis was suggested for the occurrence of such a large abundance of *c*-type cytochromes bearing multiple hemes, which is their involvement in the supercapacitance skills of *Geobacter* spp. (105,117,118).

Table 1.1 – Examples of electron donors and acceptors of diverse *Geobacter* spp. Adapted from Lovley *et al.*, 2011 (26).

***Geobacter* spp.**		**Electron donors**	**Electron acceptors**
G. argillaceus (123)	Acetate	butanol, butyrate, ethanol, glycerol, lactate, pyruvate, valerate	Fe(III)-citrate, Fe(III)-nitrilotriacetic acid, Fe(III)-pyrophosphate, poorly crystalline iron oxides, nitrate, Mn(IV), S(0), U(VI)
G. bemidjiensis (124)		benzoate, butanol, butyrate, ethanol, fumarate, H_2, isobutyrate, lactate, malate, propionate, pyruvate, succinate, valerate	Fe(III)-citrate, Fe(III)-nitrilotriacetic acid, Fe(III)-pyrophosphate, poorly crystalline iron oxides, AQDS, fumarate, malate, Mn(IV)
G. bremensis (125)		benzoate, butanol, butyrate, ethanol, formate, fumarate, H_2, lactate, malate, propanol, propionate, pyruvate, succinate	poorly crystalline iron oxides, fumarate, malate, Mn(IV), S(0)
G. chapellei (126)		ethanol, formate, lactate	Fe(III)-nitrilotriacetic acid, poorly crystalline iron oxides, AQDS, Mn(IV)
G. daltonii (127)		benzoate, butyrate, formate, toluene	Fe(III)-citrate, poorly crystalline iron oxides, fumarate, malate, S(0), U(VI)
G. grbiciae (126)		butyrate, ethanol, formate, propionate, pyruvate	Fe(III)-citrate, poorly crystalline iron oxides, AQDS
G. hydrogenophilus (126)		benzoate, butyrate, ethanol, formate, H_2, propionate, pyruvate, succinate	Fe(III)-citrate, poorly crystalline iron oxides, fumarate, AQDS
G. lovleyi (128)		benzene, benzoate, butyrate, citrate, ethanol, formate, glucose, lactate, methanol, propionate, succinate, toluene, yeast extract	Fe(III)-citrate, poorly crystalline iron oxides, fumarate, malate, nitrate, tetrachloroethylene, trichloroethylene, Mn(IV), S(0), U(VI)
G. metallireducens (43)		benzaldehyde, benzene, benzoate, benzylalcohol, butyrate, butanol, *p*-cresol, ethanol, *p*-hydroxybenzaldehyde, *p*-hydroxybenzylalcohol, isobutyrate, isovalerate, phenol, propanol, propionate, pyruvate, toluene, valerate	Fe(III)-citrate, poorly crystalline iron oxides, humics, nitrate, AQDS, Mn(IV), Tc(VII), U(VI)
G. pelophilus (125)		ethanol, formate, fumarate, H_2, malate, propanol, propionate, pyruvate, succinate	poorly crystalline iron oxides, fumarate, malate, Mn(IV), S(0)
G. pickeringii (123)		butanol, butyrate, ethanol, glycerol, lactate, methanol, pyruvate, succinate, valerate	Fe(III)-citrate, Fe(III)-nitrilotriacetic acid, Fe(III)-pyrophosphate, poorly crystalline iron oxides, fumarate, malate, Mn(IV), S(0), U(VI)
G. psychrophilus (124)		butanol, ethanol, formate, lactate, malate, pyruvate, succinate	Fe(III)-citrate, Fe(III)-nitrilotriacetic acid, Fe(III)-pyrophosphate, poorly crystalline iron oxides, fumarate, malate, electrodes, AQDS, Mn(IV)
G. sulfurreducens (71)		H_2	Fe(III)-citrate, Fe(III)-pyrophosphate, poorly crystalline iron oxides, fumarate, malate, AQDS, Tc(VII), Co(III), U(VI), S(0), O_2
G. thiogenes (129,130)		acetoin, H_2	Fe(III)-nitrilotriacetic acid, fumarate, malate, nitrate, trichloroacetic acid, S(0)
G. toluenoxydans (131)		benzaldehyde, benzoate, benzylalcohol, butyrate, *m*-cresol, *p*-cresol, formate, phenol, propionate, pyruvate, toluene	Fe(III)-citrate, poorly crystalline iron oxides, fumarate
G. uraniireducens (132)		ethanol, lactate, pyruvate	Fe(III)-nitrilotriacetic acid, Fe(III)-pyrophosphate, poorly crystalline iron oxides, smectite, fumarate, malate, AQDS, Mn(IV), U(VI)

Indeed, it was reported that hemes in cytochromes of *G. sulfurreducens* are able to stockpile about 10^7 electrons per cell and in the lack of extracellular electron acceptors they may act as temporary storage units for electrons arising from energy metabolism (111,117). Thus, respiration can proceed towards conserving energy as inner membrane electron carriers are able to readily transfer electrons to the oxidized cytochromes in the periplasm that will further discharge as soon as electron acceptors become available (26).

The metal-reducing *G. sulfurreducens*

G. sulfurreducens was initially recovered from the surface of sediments of a hydrocarbon-contaminated ditch in Norman, Oklahoma (United States) (71). It is a chemoorganotroph, non-fermenting and non-forming spores rod shaped bacterium, with dimensions of approx. 2 to 3 µm in length by 0.5 µm wide (Figure 1.4). *G. sulfurreducens* is able to use the same metal electron acceptors than other *Geobacter* species and is also capable to grow in the presence of fumarate as an alternate electron acceptor (Table 1.1) (71). Its optimum temperature of growth is around 35°C and it is able to tolerate sodium chloride concentrations in the medium that can go up to half the sea water concentration (10 g/L) (66). While it was originally classified as a strict anaerobe, later studies revealed that it can thrive when exposed to atmospheric oxygen, and it is even able to grow in conditions of up to 10% O_2 (120). The ability to tolerate oxygen and use it as final electron acceptor may be an explanation for the presence of *G. sulfurreducens* in oxidative environments at the subsurface, as well as for its predominance as Fe(III)-reducing microorganism in these same environments when the oxygen levels decrease (133).

It was found for the first time with *G. sulfurreducens* PCA the ability of *Geobacter* spp. to use hydrogen and elemental sulfur, respectively as electron donor and acceptor (71). Although *G. metallireducens* has been the earliest of *Geobacter* spp. to be discovered (43), *G. sulfurreducens* was the first with its genome unveiled (134) and a genetic system fully developed (106). For these reasons, and also because it is directly related to other *Geobacter* species and is highly suitable for large scale growth meeting laboratory purposes, *G. sulfurreducens* has been widely studied as a prototype organism for *Geobacter* family.

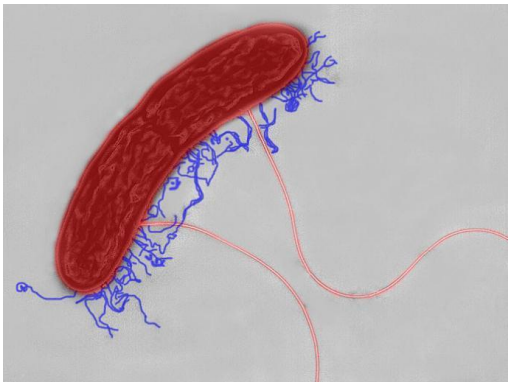

Figure 1.4 – Bacterium *G. sulfurreducens* with its pilin-like filaments. These pilin take part in the extracellular electron transfer to insoluble electron acceptors, as the case of natural iron minerals and electrodes. Credits to Derek R. Lovley, Gemma Reguera and Kevin D. McCarthy.

DIVING INTO THE CYTOCHROMES

The high and diverse number of cytochromes in *Geobacter* spp., most of them bearing multiple redox centers, constitute an added-value in the electron transfer processes as they assist in electron transport across long distances and extend the redox-active range through interactions with neighboring redox centers (heme-heme interactions) and ultimately, contribute to the increase of the reduction power of the cells (117,135). As other *Geobacter* spp., *G. sulfurreducens* contains a high number of *c*-type cytochromes and its genome has revealed the existence of 111 coding genes connected to multiple and diverse roles, 73 of which encode MHCs (134).

Cytochromes are conjugated proteins that have hemes as prosthetic groups. The heme group consists of a protoporphyrin IX that contains iron and can be in the ferrous (Fe^{2+}) or ferric (Fe^{3+}) oxidation states (136). The iron can exist in low-spin or high-spin conformations, respectively with paired and unpaired electrons. In the low-spin conformation, the heme has two strong-field axial ligands, whereas in high-spin conformation only one axial coordination is established, and the other is kept available for linkage with molecules such as NO, CO, O_2 and cyanide (137).

Electron transfer can be carried in cytochromes with hemes *a*, *b* and/or *c* in which iron usually appears hexacoordinated (138) (Figure 1.5). These hemes show typical absorption features of visible light from which they can be easily differentiated. Indeed, in its reduced state (Fe^{2+}), three absorption bands are distinguishable in the visible range named γ (Soret), α and β (139).

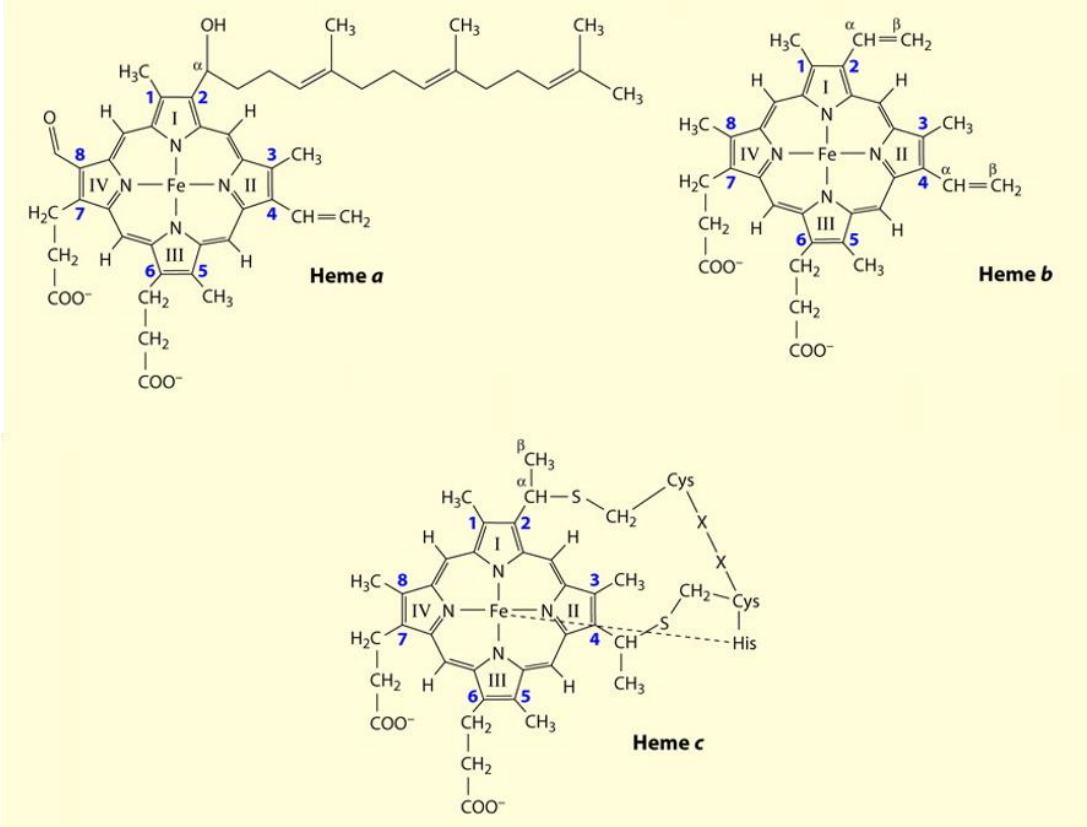

Figure 1.5 – The different types of electron transfer heme structures. Numbering follows the Fischer system. Adapted from Kranz *et al.*, 2009 (158).

Generally, *a*-type cytochromes present a maximum for the α-band between 580–590 nm, *b*-type cytochromes between 556–558 nm and *c*-type cytochromes show a maximum in the range of 549–551 nm (140).

Hemes *a* and *b* are firmly bound to the polypeptide chains in the protein, although they do not present covalent linkages. Heme *a* is a derivative of heme *b*, which usually has in the porphyrin position C2 a hydroxyethylfarnesyl group instead of a vinyl side group and in position C8 a formyl group instead of a methyl side group (141). In the case of heme *a*, the iron has two axial histidine ligands and an elongated isoprenoid tail is connected to the porphyrin (139). In heme *b*, iron has two histidines or one histidine and one methionine axial ligands, and the heme position and conformation in the molecule is controlled by hydrogen bonds and hydrophobic interactions with neighboring amino acid residues (138).

Only heme *c* is covalently attached to the polypeptide chain, by the vinyl groups of the protoporphyrin IX that are connected by thioether bonds to the sulfhydryl groups of two cysteine residues of a CX_nCH motif, where X represents variable amino acid residues and a histidine is one of the axial ligands (142). One of the most common motifs is the CX_2CH motif, although other motifs have been identified, as the CX_3CH, the CX_4CH and the $CX_{15}CH$ motifs (142–144).

According to sequence homology, *c*-type cytochromes can be grouped in four general classes (138,145,146):

- Class I – The heme groups have a histidine and a methionine as axial ligands and the attachment site to the heme is near the N-terminus. It is the most numerous family of *c*-type cytochromes and includes the mitochondrial cytochrome *c* and the cytochrome c_{550} of *Paracoccus denitrificans* (147);
- Class II – It includes the monoheme cytochromes with the attachment to the heme group near the C-terminal of the protein, such as the cytochrome *c'* of *Azotobacter vinelandii* (148) and the cytochrome c_{556} of *Agrobacterium tumefaciens* (149).
- Class III – This class comprises MHCs with axial coordination bis-histidine that is responsible for the low reduction potentials displayed by these proteins. The most well studied are the cytochromes c_3 from iron-sulfur reducing bacteria (150,151). They have around 120 amino acid residues and contain four heme groups, consecutively numbered as I, II, III and IV according to the order of appearance of the cysteine residues to which they are attached in the sequence. Despite the low sequence identity in this class, the positioning and orientation of the hemes is well conserved in the three-dimensional structures (151). Also in this class are the triheme c_7 cytochromes from the dissimilatory metal reducing bacteria (152–154), which are structurally very similar to the c_3 cytochromes but have no heme II nor the sequence of amino acid residues that connects it to the structure. Due to its homology and for comparison purposes simplification, the hemes are numbered as I, III and IV according to the nomenclature of the cytochromes c_3 (155).
- Class IV – In this class are typically included MHCs with both axial coordination bis-histidine and histidine-methionine, as the photosynthetic reaction center of *Rhodopseudomonas viridis* (156).

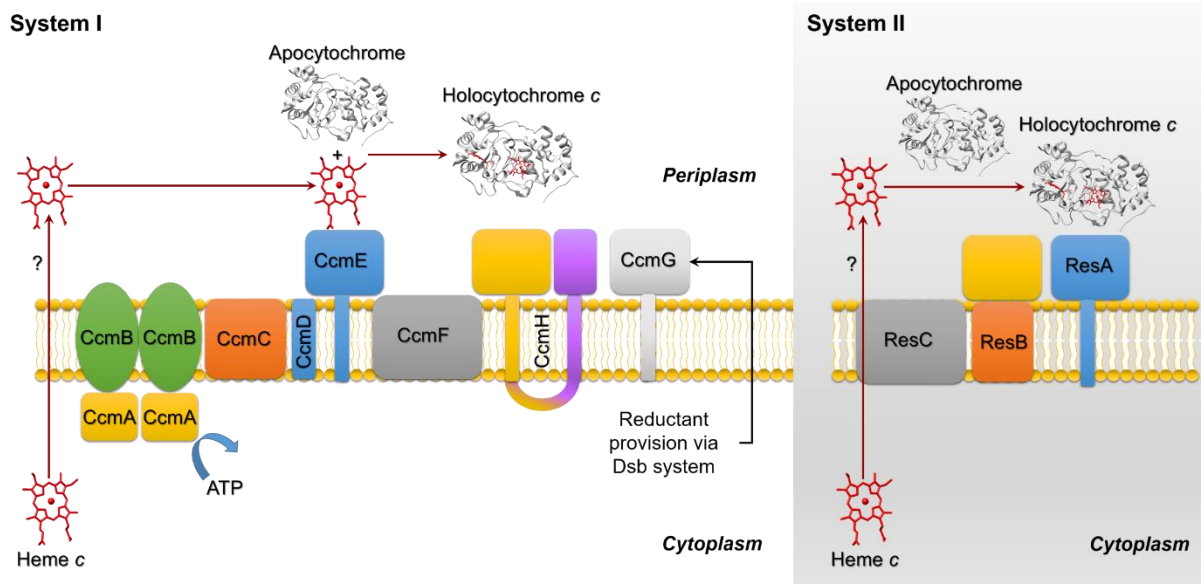

Figure 1.6 – **Illustration of the key constituents of Systems I and II.** The former is based in *E. coli* and the latter in *Bacillus subtilis*. Adapted from Mavridou *et al.*, 2013 (319).

The hemes are covalently attached to the heme binding motifs in post-translational catalyzed processes mediated by other proteins. In *Bacteria*, Systems I and II are responsible for the heme attachment process in the periplasm (Figure 1.6).

System I occurs in α- and γ-proteobacteria and in some β- and δ-proteobacteria (157,158). In *E. coli* this system comprises the cluster of proteins CcmABCDEFGH and is expressed solely under anaerobic growth conditions (159). System II is present in Gram-positive bacteria, cyanobacteria, ε-proteobacteria, most β-proteobacteria and some δ-proteobacteria and comprises three or four membrane-bound proteins that compose the cytochrome *c* synthase (CcsA or ResC and CcsB or ResB) and generate the reduced heme attachment motif (CcdA and CcsX or ResA) (158,160).

Co-expression in *E. coli* of Systems I or II (161,162) together with a target cytochrome *c* has been a methodology extensively used towards the successful expression of recombinant proteins in aerobic conditions, even in the cases of MHCs (143).

As described above, the apo-protein needs to be translocated to the periplasm, where the hemes are assembled (158,163). This process relies upon a short signal peptide sequence, which has a N-terminus positively charged, a hydrophobic region (H-region) and a neutral C-terminus for recognition by the periplasmic signal peptidases (164,165). The recognition of the N-terminal and translocation of the apo-protein in Gram-positive and Gram-negative bacteria is performed by the Sec pathway. It catalyzes the transmembrane translocation of proteins in their unfolded conformation, although with a peptidase cleavage site quite different – seven to nine and three to seven residues from the C-terminal end of the H-region, respectively for Gram-positive and Gram-negative bacteria (166,167).

The extracellular electron transfer pathway of *G. sulfurreducens*

In *G. sulfurreducens* PCA and DL-1 it has been proposed that a porin-cytochrome pathway is responsible for the extracellular electron transfer process (168) (Figure 1.7).

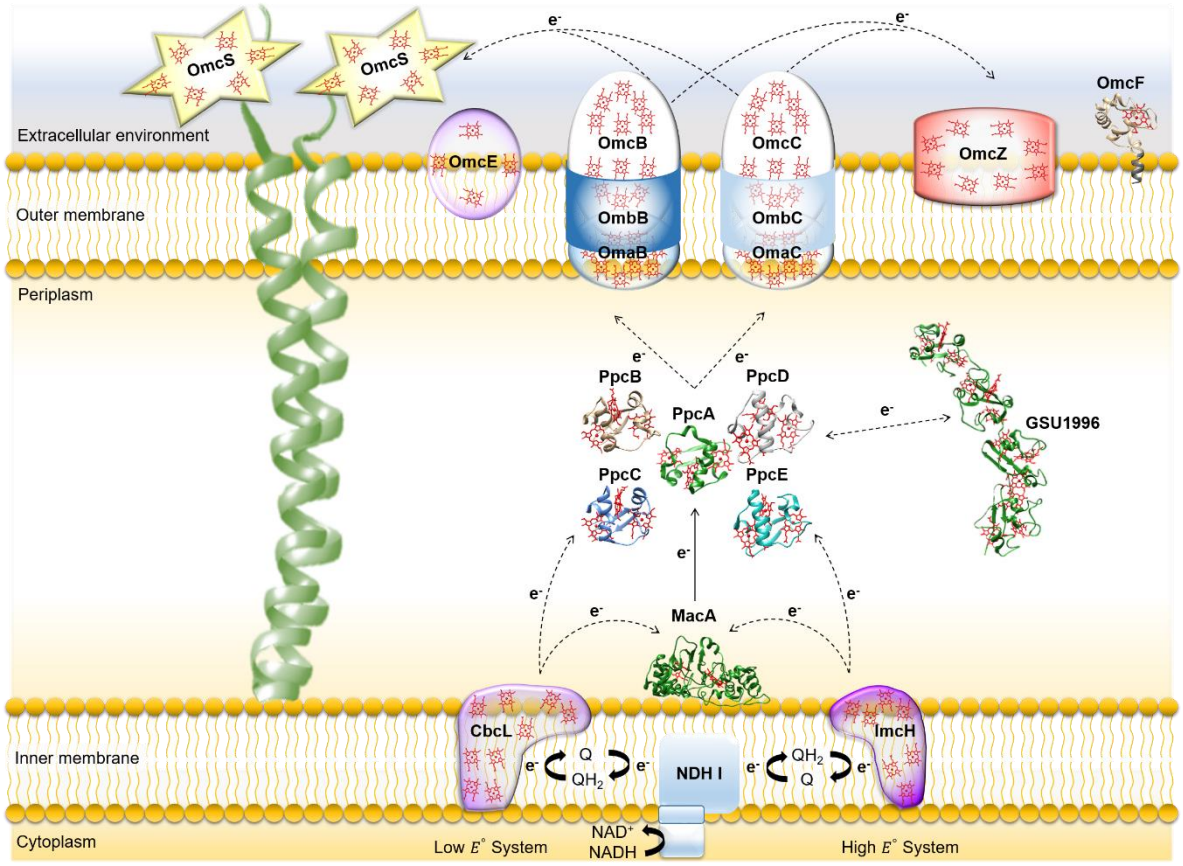

Figure 1.7 – Porin-cytochrome pathway of *G. sulfurreducens*. Molecular structures of known cytochromes were performed with the UCSF Chimera package (320) from PDB files 4AAL (MacA), 2LDO (PpcA), 3BXU (PpcB), 3H33 (PpcC), 3H4N (PpcD), 3H34 (PpcE), 5MCS (OmcF) and 3OV0 (GSU1996) (321). Inner-membrane cytochromes are represented by CbcL and ImcH; outer-membrane cytochromes by OmcE, OmcS and OmcZ and outer-membrane porin-cytochrome complexes by OmaB/C, OmbB/C to OmcB/C, with the respective number of heme groups associated. Adapted from Santos *et al.*, 2015 (135).

Two different constitutive inner membrane pathways were already identified for the transport of electrons from the inner membrane quinone pool to the external environmental acceptors: the CbcL and the ImcH-dependent pathways (from GSU0274 and GSU3259 inner membrane cytochromes *c*, respectively) (169–172). The constitutive pathway CbcL is a low potential pathway necessary for growth with electron acceptors and electrodes at or below potentials of −0.10 V (versus standard hydrogen electrode (SHE)), while the ImcH is a high potential pathway crucial at redox potentials above this value.

Data points out that the CbcL-dependent pathway allows respiration in the vicinity of thermodynamic equilibrium conditions and that ImcH allows the harvesting of additional energy when it is available (171,172). These inner membrane cytochromes carry electrons from the quinone pool to inner membrane cytochromes, like the inner membrane associated diheme cytochrome MacA (GSU0466).

However, although MacA has been pointed as an electron carrier by some studies, other work indicates that the inhibition of Fe(III) reduction observed when *macA* is deleted is a consequence of the negative impact on the expression of the outer-membrane *c*-type cytochrome OmcB (GSU2737), that has an important role in Fe(III) reduction (173,174), instead of its direct participation in EET as electron carrier (175). The same result was observed by deletion of the outer-membrane *c*-type cytochrome,

OmcF (GSU2432) (109). In this sense, it is conceivable that these proteins may be involved in the control of the expression of OmcB. The lack of MacA/OmcF may cause an electron flow disruption or result in improper assembly of protein complexes and indirectly affect *omcB* transcription (175). Indeed, MacA has electrochemical properties identical to other bacterial diheme cytochrome *c* peroxidases and it is capable of electrochemically mediate electron transfer to the periplasmic triheme c_7 cytochrome PpcA (GSU0612) through a labile interaction (176). It was also proposed that they may interact under environmental oxidative stress to prevent oxidative hazards due to hydrogen peroxide generation as a consequence of one-electron reduction in Fe(III) oxyhydroxide (177,178).

PpcA occurs in high abundance in the periplasm and it has been shown to be involved in the mechanism that couples acetate oxidation with soluble Fe(III) reduction (153). In this sense, multiheme periplasmic cytochromes, such as PpcA and its homologues PpcB-E (GSU0364, GSU0365, GSU1024 and GSU1760, respectively) ensure electron transfer between the cytoplasm and the outer membrane electron transfer components (134). Even though this family of cytochromes has been associated to Fe(III) reduction pathways, their precise roles and physiologic partners are still to unveil.

In the model proposed by Santos and co-workers, PpcA putatively interacts with another cytochrome, the nanowire like cytochrome GSU1996, which is also supposed to be found in the periplasm and was mostly found in growth conditions where soluble Fe(III) citrate was used as an electron acceptor instead of insoluble forms of Fe(III) oxide (135,179).

In the outer membrane, the periplasmic octaheme cytochromes OmaB (GSU2738) and OmaC (GSU2732) associate with the porin-like outer membrane proteins OmbB (GSU2739) and OmbC (GSU2733) and with the outer membrane dodecaheme cytochromes OmcB and OmcC (GSU2731) to generate two porin-cytochrome trans-outer membrane protein complexes responsible to transfer the electrons for the reduction of extracellular electron acceptors (168,173,180,181).

Other outer membrane cytochrome, OmcE (GSU0618), has also been enrolled in the EET as genomic data showed that it is involved in the reduction pathways of Fe(III) and Mn(IV) oxides and U(VI) (177,182–184).

The outer-surface, *c*-type cytochrome OmcZ (GSU2076) that is found loosely bound to the outer-surface matrix, is crucial in current production in *G. sulfurreducens*. Under current-producing environments, OmcZ is positioned at the anode surface and it has been proposed to act as an electrochemical gateway to assist in the electron transfer from *G. sulfurreducens* biofilms to the anode surface (185,186).

Geobacter spp., as *G. sulfurreducens* PCA and *G. metallireducens* GS-15, express nanowires – pili anchored to the cell envelope – that were recently reported as filaments composed of micrometer-long polymerization of the hexaheme cytochrome OmcS. These nanowires are enrolled in the electron transfer among cells as well as with electrodes, Fe(III) oxides and oxyhydroxides and in the reduction of manganese oxides (121,184,187,188). In *G. metallireducens* GS-15, nanowires were suggested to carry electrons directly to *Archaea* methanogens (23). It was proposed that the filament structure, with the hemes tightly packed across its micrometer length, is responsible for electron transfer in the nanowires (188).

Information gathered with the redox characterization of the cytochromes implicated in extracellular electron transfer mechanisms points to an overlap between the redox-active potential windows. Overall, these cytochromes and porin proteins probably ensure the electron transport from the quinone/quinol pool located in the cytoplasmic membrane across the periplasm and outer membrane of *G. sulfurreducens* and the presence of different protein homologues point for the occurrence of several electron transfer routes that may be active and even occur at the same time according to the environmental surroundings (57,135,168,172,181,189,190) (Figure 1.7).

Nanowire like *c*-type cytochromes of *G. sulfurreducens*

Examples of nanowire like *c*-type cytochromes, first described for *G. sulfurreducens*, are encoded by ORFs 00991, 03300 and 03649. These are named GSU0592, GSU1996 and GSU2210, respectively (134) and counterparts of each of these cytochromes were also found in other *Geobacter* spp. (105). Surprisingly, such odd cytochromes are polymers and their structural units are domains that resemble those of c_7-type cytochromes, as PpcA and its homologues (191). GSU0592 and GSU1996 comprise four c_7-like domains and GSU2210 contains nine of these units. All the polymers consist of homologous repetitions that range from 73 to 82 amino acid residues (192).

It was found that GSU0592, named CbcC, is encoded by the same predicted operon for the *c*-type cytochromes CbcA (GSU0594) and CbcD (GSU0591), the *b*-type cytochrome CbcB (GSU0593) and the membrane protein CbcE (GSU0590). It was suggested that the five proteins may function together as a menaquinol:ferricytochrome *c* oxidoreductase (Cbc5 complex) in the extracellular electron transfer to insoluble electron acceptors, such as Fe(III) and Mn(IV) oxides and gene deletion studies demonstrated that CbcC plays a crucial role in electron transfer to Fe(III) oxide (177). Simultaneously, Bansal *et al.* performed a global proteomic analysis of *G. sulfurreducens* under long term electron acceptor limitation cell growth conditions and detected an increase in the heme cellular content, clearly observable by the reddish cultures color. This was also indicative of a higher cytochrome amount, as confirmed by the proteomic analysis, with the cells in an extremely reduced state and GSU0592 (called OmcQ by Bansal and co-workers) was found to be increased by about three-times in starved cells, which involves this cytochrome in the mechanisms of survival under such adverse environmental conditions (193).

Whole-genome microarray analysis showed that GSU2210 gene was upregulated under growth in the presence of Fe(III) and Mn(IV) oxides (177) and proteome characterization revealed greater quantity of this large cytochrome in cells grown in the presence of Fe(III) oxide (179).

In a work performed by Ding and co-workers (179), where the proteome of *G. sulfurreducens* cells grown with Fe(III) oxide or Fe(III) citrate as electron acceptors was studied, GSU1996 was found to be more expressed in the presence of the soluble iron form (179).

The crystal structure of GSU1996 revealed a one-dimensional array of 12 nm structure in a crescent like design, where the twelve hemes are organized along the polypeptide chain in a nanowire resembling scheme. The 42.3 kDa dodecaheme *c*-type cytochrome GSU1996 is formed by an array of four similar c_7-like domains each with 78-82 amino acid residues with around 11 kDa in average, in a total of 318 amino acid residues (192) (Figure 1.8).

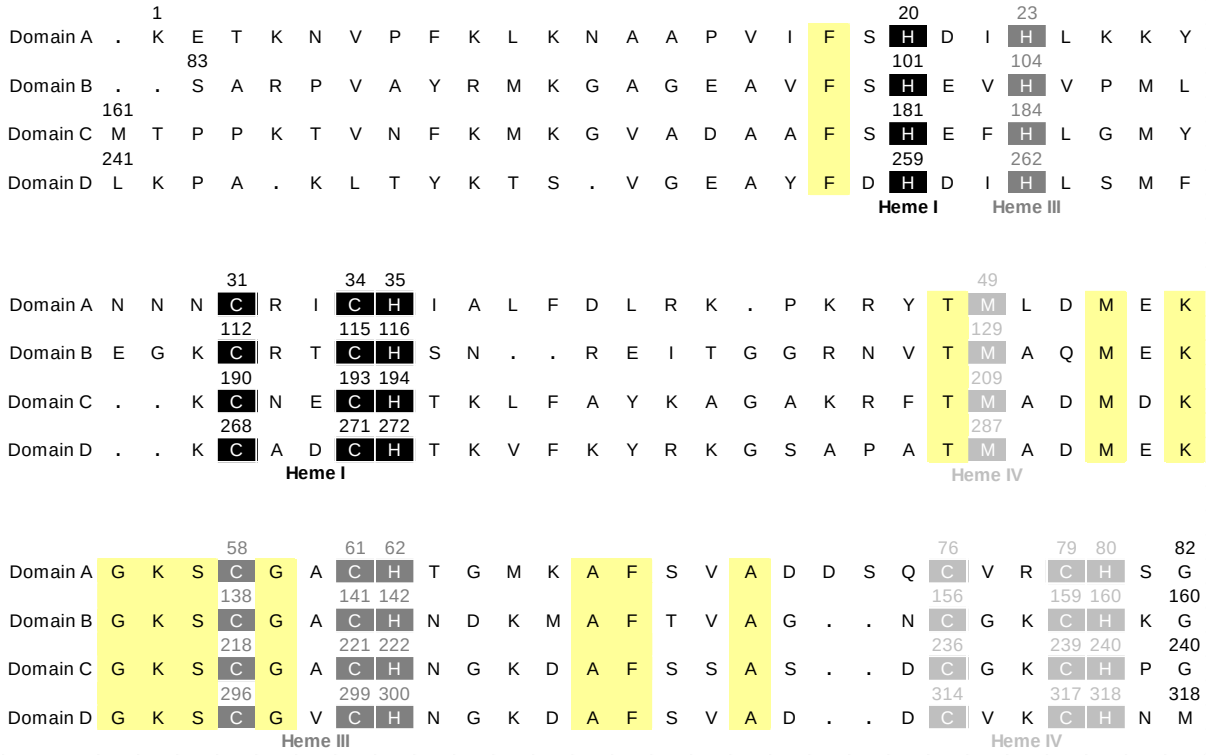

Figure 1.8 – **Sequence alignment of the four domains of GSU1996.** Heme-binding residues are labeled for the respective hemes and non heme-binding conserved residues are highlighted in yellow.

These domains display 40-56% sequence similarity among them and were named sequentially A, B, C and D. Given its structure, it has been proposed that GSU1996 may work as a natural nanowire for electron transfer (194,195) (Figure 1.9).

The N-terminal part of the molecule is formed by the hexaheme fragment AB and appears to behave as one structural unit while the C-terminal, formed by the hexaheme fragment CD, displays a more independent behavior between each of the forming domains. Indeed, the interface between domains A and B revealed an unpredicted interaction that occurs between heme IV from domain A and heme I from domain B where the porphyrin rings show almost parallel stacking while domains C and D are linked by a small four amino acid residues flexible connector.

The c_7-like domains enclose more positively charged residues (lysine and arginine residues) than negatively charged ones (aspartate and glutamate residues), such as found in the c_7 cytochromes. In GSU1996, domain A is the more positively charged and domain D the less positively charged and therefore, the net positive charge of the protein diminishes from the N- to the C-end (195).

Proteomic studies revealed that GSU1996 may be associated to cytoplasmic or outer membranes (182) and it was proposed that the fragment AB may provide an electrostatic interaction site with the membranes (195).

Within each of the triheme domains two hemes have bis-His axial coordination (hemes I and III) and one has His-Met axial coordination (heme IV). All three hemes exhibit low-spin behavior. The iron-iron distances for the adjacent hemes in the domains are within van der Waals range, from 11.2 to 12.1 Å, and allows effective electron exchange amid the hemes (195).

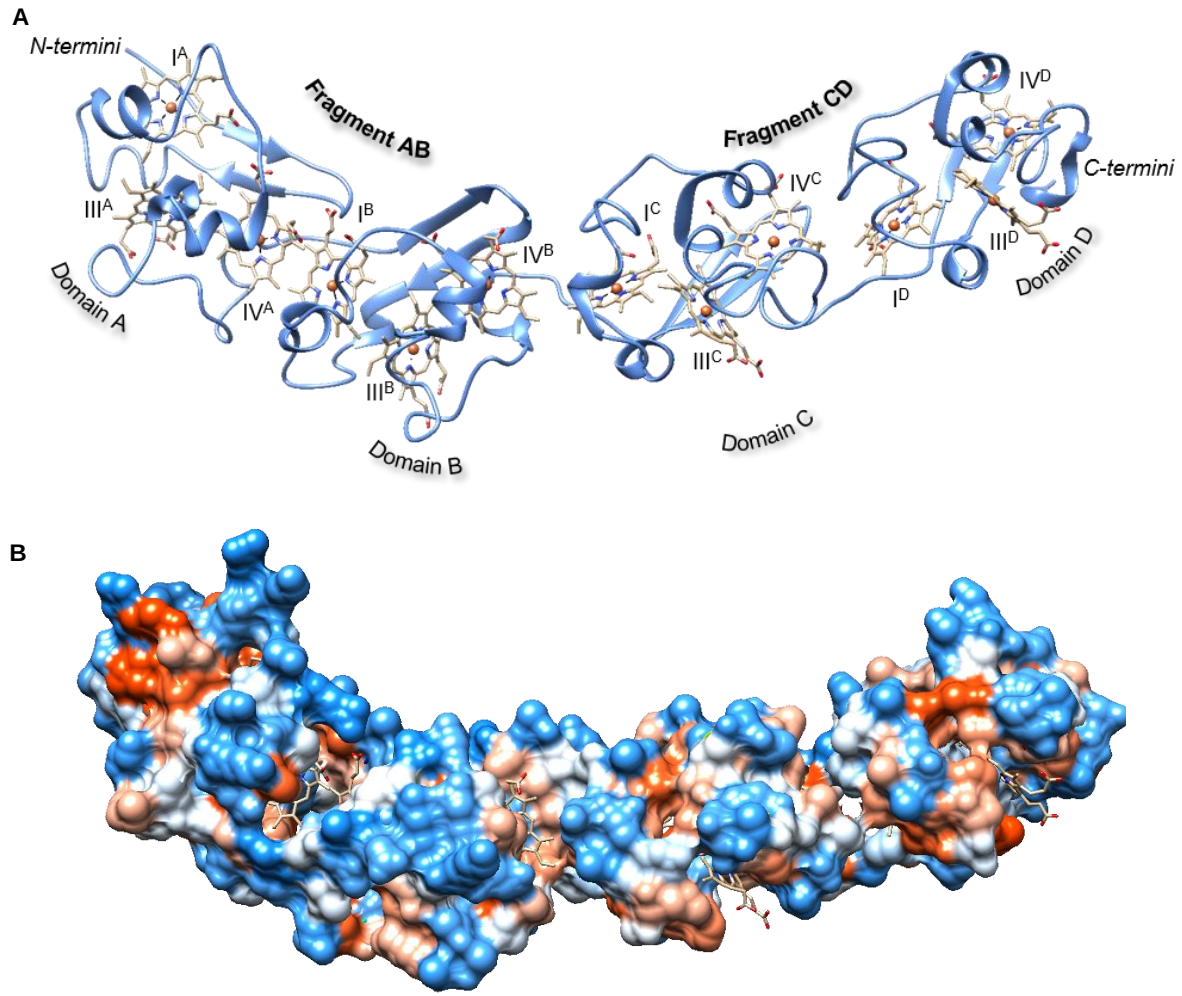

Figure 1.9 – Crescent shaped structure of GSU1996. A) Typically, the domains comprise two antiparallel N-terminal β-strands followed by loops sprinkled with helical fragments that contain the heme-binding residues. B) Hydrophobicity surface. The hydrophobic core of the domains contains the heme groups and a number of aromatic/hydrophobic side chains. The molecular structures of GSU1996 were produced with the UCSF Chimera package (320) from PDB file 3OV0 (321). The hemes are numbered according with the tetraheme cytochrome c_3 heme nomenclature and superscript letters represent their respective domains.

In order to explore the properties of this large and complex multiheme cytochrome, a puzzle based strategy was earlier adopted, where the study of the individual domains and two-domain fragments of GSU1996 assist in the characterization of the full protein (192,194,196). While X-ray crystal data revealed that fragment AB corresponds quite well to its counterpart in the full length GSU1996, the same was not verified in the C-terminal of the molecule. Indeed, a substantial curvature is observed for domains C and D in GSU1996 while in the fragment CD both domains are connected in a linear arrangement, although this may be related to constraints due to crystal lattice interactions (195) (Figure 1.10).

Visible spectroscopy redox titration profiles obtained for GSU1996 and its N- and C-terminal fragments display an analogous macroscopic redox performance. Both fragments exhibit comparable macroscopic reduction potentials (E_{app}) and in the case of the C-terminal, the E_{app} values determined indicate that domain D is more readily oxidizable than domain C (195,197) (Table 1.2).

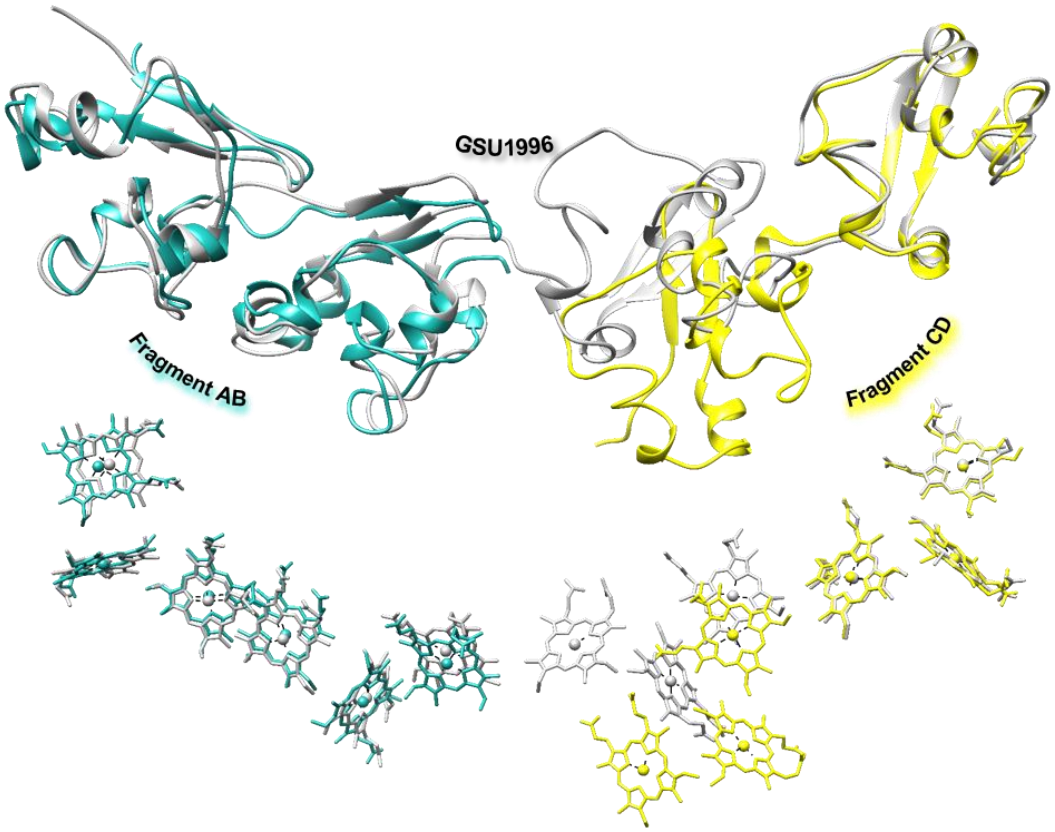

Figure 1.10 – **Overlay of the crystal structures of fragment AB (cyan) and fragment CD (yellow) with GSU1996 (gray).** For better understanding, above it is shown the ribbons overlap and below the respective hemes overlap. The structure comparison was performed with the UCSF Chimera package (320).

Albeit relevant, the E_{app} is far from revealing the behavior of the redox centers within a multiheme protein as a number of intermediary microstates can occur simultaneously between the fully reduced and fully oxidized proteins.

It is then further necessary to monitor the oxidation pattern of the individual hemes to ascertain its microscopic parameters, which comprise the heme reduction potentials, the *pKa* values of the redox-Bohr centers, the heme-heme redox interactions and the redox-Bohr interactions. In the case of GSU1996, this was only achieved so far for domain C and its microscopic characterization exposed that the hemes are heavily modulated by structural traits and redox interactions, heme IV His-Met coordinated did not enclose the highest potential in the domain (197) (Table 1.3).

Table 1.2 – Apparent mid-point reduction potentials (E_{app}) versus standard hydrogen electrode (SHE) determined for full length GSU1996, its N- and C-terminal fragments and single domains C and D at 298 K and pH 7.9 (195,197).

	E_{app} (mV)
GSU1996	−119
Fragment AB	−123
Fragment CD	−122
Domain C	−105
Domain D	−133

Table 1.3 – Microscopic thermodynamic parameters for domain C. The oxidation energies of the hemes and the deprotonating energy for the fully reduced and protonated protein are presented in bold. The non-bold data refers to heme-heme and redox-Bohr interaction energies. The standard errors are shown in parenthesis (197).

	Energies (meV)			
	Heme I	Heme III	Heme IV	Protonatable center
Heme I	**−106 (2)**	44 (2)	7 (2)	−4 (6)
Heme III		**−136 (2)**	40 (2)	−25 (6)
Heme IV			**−125 (2)**	−13 (7)
Protonatable center				**340 (11)**

Although physiologic purpose and interaction partners remain undisclosed, it has been proposed that such large multiheme cytochromes may act as capacitors to ensure survival of cells in periods of environmental stress (182,195).

For that reason, it is imperative to understand the functional properties of these nanowire cytochromes, not only to move forward in the understanding of the electron transfer mechanisms of *Geobacter* spp. and akin microorganisms, but also as they may be reference guides towards the rational design of nanoconductor devices and, as earlier stated, in the improvement and design of new biotechnological applications based in these biosystems (194).

OBJECTIVES

This work had as main goals the determination of the cellular localization of the dodecaheme GSU1996 from *G. sulfurreducens* together with its functional properties and interacting partners.

The functional characterization encompasses the microscopic thermodynamic and kinetic characterization and it is preceded by the heme signals assignment in nuclear magnetic resonance (NMR) spectra. In order to perform the functional characterization of the large size GSU1996, a modular characterization approach was followed. Here, the triheme domains were used as a guide to assist in the study of the hexaheme fragments of GSU1996.

Putative redox partners of GSU1996 – namely PpcA and its homologues –, were probed in order to shed light upon the probable function and electron transfer mechanisms where this nanowire participates.

Furthermore, a strategy towards the accurate cellular localization of *c*-type cytochromes was attempted, based in the expression of tetracysteine-tagged mutant proteins, fluorescent upon binding with biarsenical dyes.

Another goal was to open way to the unveiling of other EET components. In this sense, heterologous expression systems were probed to promote the high yield expression of the outer membrane cytochrome OmcE, of the hexaheme cytochrome OmcS and of the nanowire cytochrome GSU2210.

CHAPTER 2

A BRIEF SYNOPSIS OVER NUCLEAR MAGNETIC RESONANCE AND KINETICS APPLIED TO THE STUDY OF MULTIHEME *C*-TYPE CYTOCHROMES

Contents

INTRODUCTION

Nuclear Magnetic Resonance (NMR) spectroscopy has been widely used in the study of numerous biomolecules, as it is able to provide insights towards structural data at an atomic resolution in its native or close to physiological conditions. It can be applied, for instance, to probe for structural, thermodynamic and kinetic features of protein interactions either with solution components under several conditions of pH, temperature, ionic strength and/or putative partners, proteins or other type of ligands.

In multiheme *c*-type cytochromes (MHCs), electron transfer processes may occur along short distances between interacting proteins or amid proteins and other interacting partners (intermolecular electron transfer) or over long distances across a single protein (intramolecular electron transfer) (198,199). Therefore, in MHCs it is of utmost importance to understand not only the macroscopic aspects that are involved in the intermolecular interactions but also the microscopic parameters that explain how the electron flow occurs within a protein.

NMR spectroscopy has proven to be an exquisite tool to enlighten the redox properties of MHCs, as it allows the discrimination of each individual redox center (200–202). The detailed study of the functional properties of the redox centers in MHCs starts with the assignment of the signals in the NMR spectra to the specific heme protons in the protein in either reduced and/or oxidized states. Next, the signals of the heme protons are monitored by NMR techniques in redox titration experiments in order to establish the order of oxidation/reduction of the respective hemes within the protein. This information combined with data acquired in redox titration experiments followed by UV-visible spectroscopy or by cyclic voltammetry techniques makes it possible to determine the microscopic thermodynamic parameters and disclose the possible electron transfer pathways within the MHC.

Nonetheless, the comprehension of such intricate molecules cannot be complete without the in-depth analysis of their electron transfer rates. Therefore, kinetic properties of such proteins need also to be determined so as to reveal the velocity of each electron transfer event and clarify the actual electron transfer steps that occur in the cytochrome. Given its complexity, kinetic models based on Marcus theory of electron transfer were already proposed (203) for the analysis of the kinetics of electron transfer of MHCs and their electron donors/acceptors. The assumptions considered in such approaches make it possible to differentiate the contribution of each heme to the global oxidation/reduction process.

Below, a brief synopsis of the NMR principles and techniques used in this work is presented and the kinetic models applied to the study of electron transfer properties of MHCs are reviewed.

NMR SPECTROSCOPY OVERVIEW

In the presence of a strong magnetic field, nuclear spins with quantum number (*I*) other than zero are mostly found aligned according to the direction of the applied field. In the particular case of $I = \frac{1}{2}$, the nuclei have two different orientations relative to the applied field, which correspond to two energy levels (Figure 2.1), given by Equation 2.1:

$$E = -\frac{\gamma m h}{2\pi} B_0$$ **Equation 2.1**

In this equation, γ represents the gyromagnetic ratio, that relates the nuclear spin magnetic moment μ with the nuclear spin quantum number I; m represents the quantum magnetic number; h is the Planck's constant and B_0 denotes the magnetic field applied.

At equilibrium, the lowest energy level is aligned with the applied field and it is somewhat more populated. For this reason, there is a global magnetization in this direction. Transitions between the two energy levels can be stimulated by a radiofrequency impulse, where the nuclear spins in the lowest level are momentarily excited and afterwards return to their equilibrium state. The recovery of the initial magnetization is exponential and gives rise to the free induction decay magnetization (FID).

NMR spectroscopy encompasses the analysis of the excitation and following relaxation process of the different spin groups until the equilibrium position is restored. The Fourier transformation is used to process FID and originates the NMR spectra. Signals are called resonances and its frequencies are designated by chemical deviations (δ). Chemical deviations are resonance frequencies expressed relative to the position of a given standard that, by definition, is located at 0 parts per million (ppm) and are independent of the spectrometer frequency (Equation 2.2).

$$\delta = \frac{Signal\ frequency - Standard\ frequency}{Spectrometer\ frequency} \times 10^6$$ **Equation 2.2**

A simple one-dimensional NMR (1D NMR) experiment of a protein consists in the excitation of all nuclei by a non-selective radiofrequency pulse of 90° and in the subsequent acquisition of all spin groups responses until the recovery of the initial magnetization along time *t*.

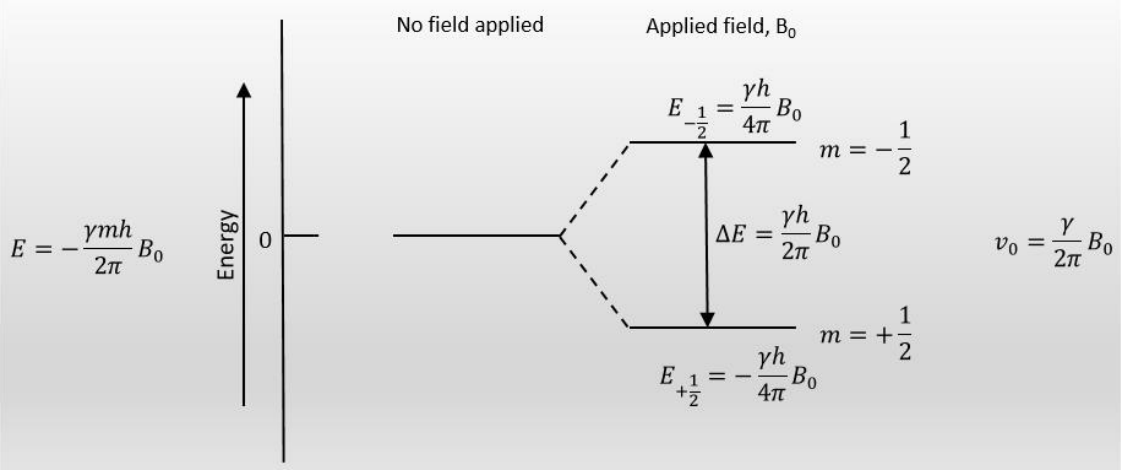

Figure 2.1 – Energy levels upon an applied field. A nuclei with $I = \frac{1}{2}$ may adopt two different orientations in the presence of a magnetic field, B_0, with quantum magnetic numbers $m = +\frac{1}{2}$ and $m = -\frac{1}{2}$ that give rise to two energy levels. Transitions between these energy levels can occur with the application of an electromagnetic radiation of ν frequency, in agreement with Planck's condition. Adapted from Skoog *et al.*, 1998 (322).

In a protein with a high number of amino acid residues, the overlay of signals acquired after FID processing is unavoidable and this is one of the major problems intrinsic to 1D NMR experiments. Fortunately, multidimensional NMR techniques, such as two-dimensional NMR (2D NMR), have made it possible to overcome some of these issues. A 2D NMR experiment consists in a sequence of four states. The preparation state is akin 1D NMR and comprises the excitation of the biomolecules nuclei with a radiofrequency pulse. Next, in the evolution state, the system evolves along a time t_1 until the mixing state, where magnetization transfer between spin groups occurs. The mixing state ends with the beginning of the detection state, where FID is acquired during time t_2 and it is usually preceded by the application of another pulse. Every time that magnetization transfer occurs between groups with different precession frequency[1], the NMR spectrum will show a connectivity between such frequencies. The analysis of different forms of magnetization transfer among spin groups is quite relevant, as it allows the gathering of distinct but complementary information and is briefly explained below.

Transfer of magnetization through chemical bonds

In 2D homonuclear correlation spectroscopy (2D COSY) and total correlation spectroscopy (2D TOCSY), the transfer of magnetization arises from chemical linkages between coupled protons (204). COSY experiments identify coupled spins up to three chemical bounds. Although similar to COSY, TOCSY shows not only directly coupled nuclei but also nuclei that are connected by a chain of couplings and, therefore, protons that belong to the same spin system. In 2D heteronuclear multiple quantum correlation spectroscopy (2D HMQC) and 2D heteronuclear single-quantum correlation (2D HSQC) it is possible to acquire a heteronuclear chemical shift correlation between protons and directly bonded X-heteronuclei, as ^{13}C and ^{15}N. HSQC and HMQC provide similar information but the first is only limited to directly bonded nuclei.

Transfer of magnetization by chemical exchange and/or dipolar relaxation

In 2D nuclear Overhauser spectroscopy (2D NOESY) and exchange spectroscopy (2D EXSY), the transfer of magnetization occurs through chemical exchange and/or dipolar relaxation between two nuclei that are in the vicinity of each other, regardless of the existence of chemical linkage among them (204). Both techniques are based in nuclear Overhauser effect (NOE), where nearby atoms (up to 5 Å) are under the effect of crossed relaxation. A proton NOE is defined as the fractional variation of the intensity of the signal when another resonant signal is saturated and it is influenced by the internuclear distance r (^1H-^1H) and times of correlation τ_c (Equation 2.3) (205).

In Equation 2.3, $f(\tau_c)$ represents the correlation function that describes the modulation of the coupling dipole-dipole with a time of correlation τ_c for a NOE:

$$NOE \propto \frac{1}{\langle r \rangle^6} f(\tau_c) \qquad \textbf{Equation 2.3}$$

[1] The precession frequency refers to the frequency that relates with the energy difference between the energies of two spin states.

For a given ^{1}H-^{1}H couple, the correlation time is determined by the random movement of the molecules in solution as a consequence of the collisions among them (Brownian movement). This depends of the size and shape of the proteins and also of the viscosity (η) of the solvent (Equation 2.4, where *T* represents the temperature and *k* is the Boltzmann constant).

$$\tau_c = \frac{4\pi\eta r^3}{3kT} \qquad \textbf{Equation 2.4}$$

Furthermore, it can be affected by intramolecular movements. Consequently, $f(\tau_c)$ may change considerably for different ^{1}H-^{1}H couples within the same protein (205). Additional ambiguities may arise due to the partial extinction of individual ^{1}H-^{1}H NOE's as a result of competitive processes of relaxation of spin, such as spin diffusion, chemical or conformational exchange and interactions with other electronic or nuclear spins. Alternatively, as a consequence of the fast intramolecular mobility, a given NOE may also be the result of sampling within a certain range of distances between a pair of protons (206).

NOESY techniques are based in the nuclear Overhauser crossed relaxation between nuclear spins over mixing times. Spectra crossed signals connect nuclear resonances that are in close spatial vicinity, unlike COSY technique, where signals reflect chemical linkages. When NOESY is applied in the detection of chemical and conformational exchanges, the technique is called EXSY.

General features of NMR spectra of low spin *c*-type cytochromes

Coordination compounds fall into two classes according to their spin state: high or low spin compounds. The electronic configuration is directly related with the amount of energy necessary to pair electrons within an orbital (low spin configuration, with a minimum of unpaired electrons) *versus* leaving electrons unpaired in different orbitals (high spin, with a maximum of unpaired electrons) (207). Iron coordination compounds may have up to five unpaired electrons, with only one electron in each of the 3*d* orbitals in cases where iron is five-coordinated or, otherwise, they may have one unpaired electron, with the five *d* electrons in the three lowest orbitals in cases where iron is six-coordinated, regardless of its oxidation state (+2 or +3) (Figure 2.2) (207). In NMR spectra both high and low spin configurations can be easily discriminated as high spin *c*-type cytochromes show signals in a broader range than low spin *c*-type cytochromes, both in the reduced and in the oxidized state. Generally, high spin *c*-type cytochromes may present signals above 40 ppm and 15 ppm in the oxidized and reduced state, respectively, while low spin *c*-type cytochromes typically show signals below 40 ppm and 12 ppm.

C-type cytochromes with axial coordination His-Met, as the case of heme IV in each of the GSU1996 domains, are usually low spin proteins and can be detected in the oxidized state by UV-visible spectroscopy techniques, as they present a typical peak at around 695 nm (145).

Low molecular weight cytochromes with iron in low spin configuration present ^{1}H-NMR spectra quite different, although well resolved in both reduced (diamagnetic, $S = 0$) and oxidized (paramagnetic, $S = \frac{1}{2}$) states.

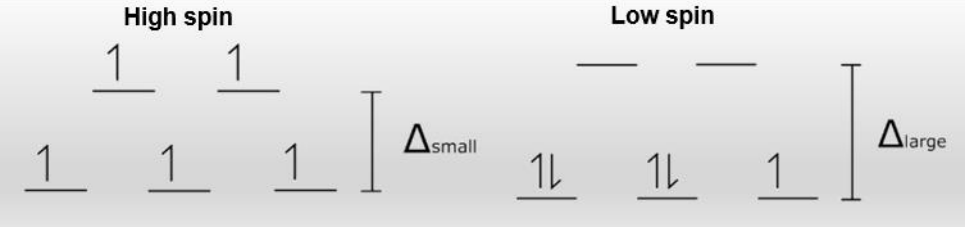

Figure 2.2 – Iron spin states. In cases where orbitals are energetically close (Δ_{small} is smaller than the pairing energy), each electron occupies its own orbital (high spin configuration). On the other hand, when Δ_{large} is higher than the pairing energy, the electrons are found paired (low spin configuration).

Despite its complexity, the presence of the heme groups and the particular state of spin of Fe^{n+} ion allows the identification of several resonances in the NMR spectra, such as the ones from heme protons that provide structural data and allow the following of redox mechanisms and interaction sites and/or partners. The deviations that are caused by ring currents in the diamagnetic form and by the interactions with the unpaired electron in the paramagnetic form shift some of these resonances out of the crowded signal region and simplify its identification (208–210). The signals may be shifted to higher ppm values than expected (low field or high frequency deviations) or may be shifted to lower ppm values (high field or low frequency deviations) (Figure 2.3).

Diamagnetic *c*-type cytochromes in the reduced form have resonances usually ranging from −5 to 12 ppm, with most of the signals between 0 and 5 ppm (Figure 2.4, upper panel). Protons positioned at the heme group plane appear in typical spectrum regions as elucidated in Figure 3.6 from CHAPTER 3. Indeed, meso protons are located between 8 and 10 ppm; methine protons from the thioether bridges range from 5 to 8 ppm; heme methyl groups are found between 2 and 5 ppm and methyl groups from thioether bridges from −1 to 3 ppm.

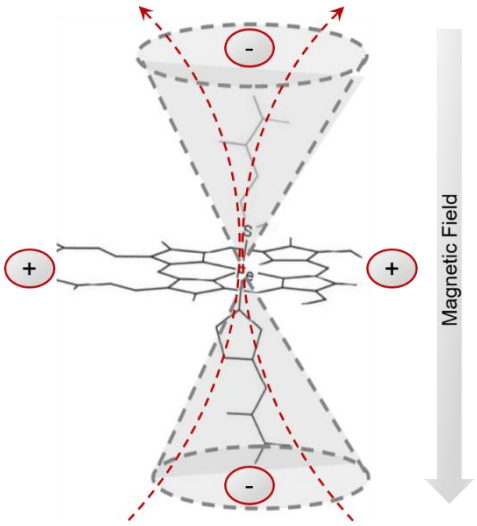

Figure 2.3 – Ring-current effect. Double-cone shaped and magnetic field lines of local ring-current field induced by a static, external magnetic field around the heme group, which behaves like a large aromatic ring. The positive signs point that NMR signals of protons located outside the cone in the protein structure are shifted downfield and the minus signs indicates signals shifted upfield. Adapted from Wüthrich, 2003 (205).

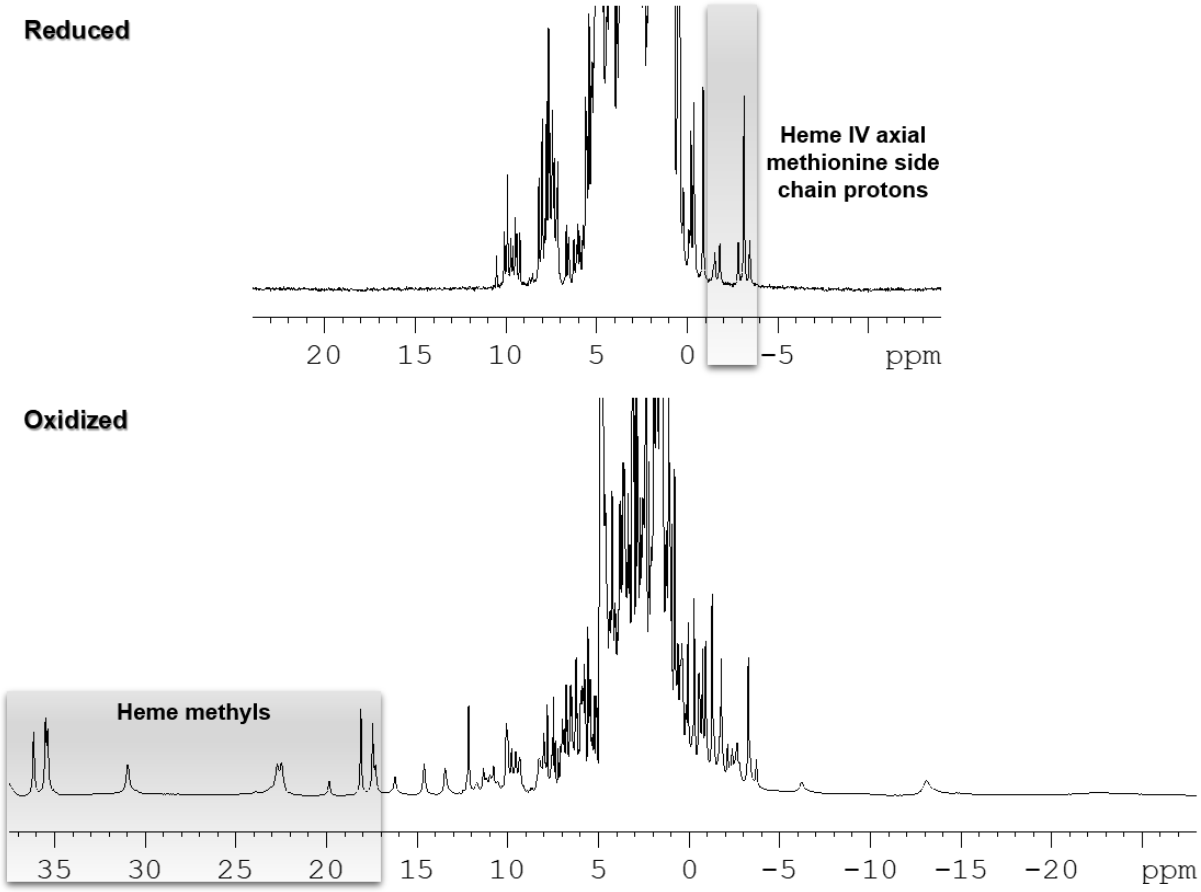

Figure 2.4 – 1D ^{1}H-NMR spectra of domain C from GSU1996 in the reduced (upper panel) and oxidized (lower panel) forms at pH 8.0 and 289.15 K. In the reduced form, heme IV axial methionine side chain protons are signalled and in the oxidized form, the heme methyls most shifted to low field are highlighted.

Although propionate groups do not present typical patterns due to their variable geometry relative to the heme plane, they frequently appear between 2 and 5 ppm.

In contrast, *c*-type cytochromes in the oxidized form present scattered resonances in larger spectral windows and with more undefined regions for chemical deviations as a consequence of the several interactions between the unpaired electron of the heme group iron and the observed nuclei (Figure 2.4, lower panel) (211). As a consequence of this paramagnetic effect, the resonance assignment is harder with only a few exceptions, as the case of some heme group methyls that are typically shifted to low field or protons that belong to axial ligand spin systems shifted to high field.

As the heme methyl substituents appear in distinct areas of the spectra in the oxidized and reduced states, in particular circumstances where the interconversion amid the same oxidation microstates (intramolecular exchange) is fast and the interconversion between different oxidation states (intermolecular exchange) is slow in the NMR time scale, separate resonances can be observed for the heme methyl groups at different stages of oxidation. Heme methyls are the most suitable substituents to follow in such studies, as their resonances are shifted to the less populated signal regions of the spectra across the reoxidation experiments and become easily recognizable, unlike other substituents (197). The chemical shift deviation of each methyl is proportional to the oxidation stage of its respective

heme group and consequently, the variation of the chemical shifts may be used to determine the patterns of oxidation of the heme groups in the protein (200,212,213). Nonetheless, 1D NMR techniques make it quite difficult to determine oxidation patterns and 2D NMR is currently employed to identify the heme oxidation patterns.

Insights of NMR spectroscopy applied to the study of transient complexes

In nature, interactions between proteins are designed with the purpose of providing just the required lifetime to fulfill the particular biomolecular role of a protein complex, rather than aiming towards the formation of high affinity complexes (214). In the case of electron transfer proteins, such as MHCs, a small lifetime is necessary to guarantee a fast turnover to withstand continuous electron flow and, therefore, interactions rely upon the formation of transient complexes (214–216).

In order to promote the formation of a particular complex with suitable affinity in such small times, unique strategies such as electrostatic attraction and preorientation at the encounter event may be employed to enhance the association rate constant to the diffusion limit (214,217). Commonly, the formation of the protein complex involves the formation of an encounter complex prior to the reactive complex. The encounter complex resembles a cluster of orientations. When the proteins are brought close together, oppositely charged regions of the proteins are positioned under the electrostatic force to face each other (Figure 2.5) (214,217,218).

Protein complexes of electron transfer proteins typically present weak affinity and short lifetimes and NMR spectroscopy techniques are especially fitted for its study (214,217).

In chemical shift perturbation experiments, a protein is titrated with its putative partner and changes in the proteins are followed along the experiment. Upon formation of a complex, modifications occur in the chemical environment of nuclei at the interacting interface which results in variations of the chemical shifts of the free proteins (δ_{free}) relative to its bound forms (δ_{bound}) (214,217).

The lifetime of the complex is clearly reflected in the NMR spectra. Therefore, if slow exchange occurs, the lifetime is large when compared with the difference between the chemical shifts of the free and bound proteins ($\Delta\delta_{max}$) and nuclei resonate only at two positions, respectively δ_{free} and δ_{bound} (Figure 2.6, left panel).

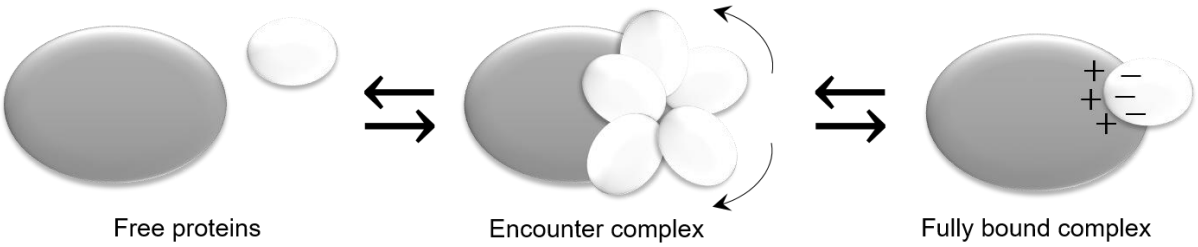

Figure 2.5 – Illustration of transient complex formation. The encounter complex is a dynamic array of orientations, where negligible chemical shift perturbations are observed. On the contrary, in the fully bound complex the proteins adopt a particular orientation in the complex guided by charge interactions and considerable chemical shift perturbations can be detected. Adapted from Ubbink, 2012 (218).

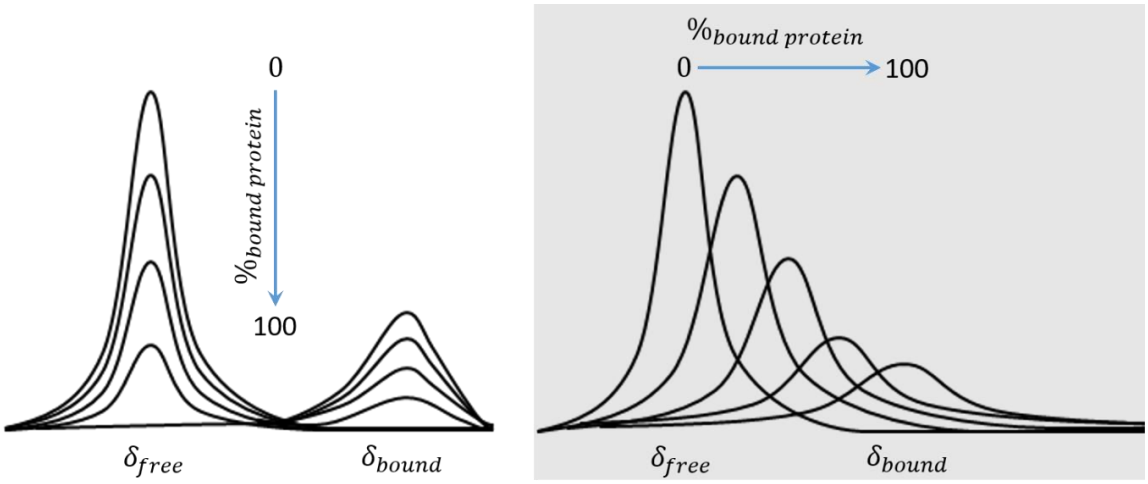

Figure 2.6 – Schematic representation of slow (on the left) and fast exchange (on the right) in a 1D NMR spectrum. In slow exchange, two resonances are observed for the nucleus, one that corresponds to the free protein and the other to the bound protein with intensities that are proportional to the respective fraction of free/bound protein. Linewidths are influenced by the size and shape of the free protein and the complex. In the fast exchange, a single resonance is observed for the nucleus at a weighted average position between free and bound protein, with linewidths also averaged between both states. Adapted from Prudêncio and Ubbink, 2004 (214).

As the partner protein increases along the titration experiment, the resonance intensity diminishes at δ_{free} and rises at δ_{bound} in agreement with the bound fraction of the protein. In cases where moderate exchange occurs, these resonances may show line broadening. When fast exchange takes place, the lifetime is quite smaller than $\Delta\delta_{max}$ and a sole resonance is observed, which corresponds to the weighted average between δ_{free} and δ_{bound} (Figure 2.6, right panel).

The ratio change of the two proteins along the titration experiment is reflected in the proportional shift of the resonance from the δ_{free} to the δ_{bound} position, as the change in the chemical shift ($\Delta\delta_{bind}$) approaches to $\Delta\delta_{max}$.

The complex formation is also accompanied by an overall broadening of the resonances that is due to the larger rotational correlation time of the complex when compared to the free proteins. Similar to chemical shifts, the linewidths of the average resonances correspond to the weighted average of the linewidths between free and bound proteins (214,217).

In the case of fast exchange, binding curves for complex formation may be derived from a function of the $|\Delta\delta_{bind}|$ *versus* the molar ratio of the interacting proteins and the affinity and stoichiometry evaluated (214,217).

KINETICS OF ELECTRON TRANSFER IN MULTIHEME *C*-TYPE CYTOCHROMES

An electron transfer reaction between a given protein and its electron donor involves at least three steps: the complex formation; electron transfer within the complex and finally, its dissociation:

$$Protein^{oxidized} + Electron\ donor^{reduced} \underset{k_{-1}}{\overset{k_{+1}}{\rightleftharpoons}} [P^{ox} - Ed^{red}] \underset{k_{-2}}{\overset{k_{+2}}{\rightleftharpoons}} [P^{red} - Ed^{ox}] \underset{k_{-3}}{\overset{k_{+3}}{\rightleftharpoons}} P^{red} + Ed^{ox}$$

In a MHC the set of steps above and its six respective microscopic rate constants (k) should be accounted for each individual center in the protein, which makes it an unrealistic task.

The kinetic analysis of electron transfer in MHCs applied in this work relies on the models developed by Catarino and Turner (203) and it is suitable for use in situations where intramolecular electron transfer occurs much more rapidly than intermolecular electron transfer and, where applicable, fast proton exchange is experienced in the experiments time-scale. This implies that a thermodynamic equilibrium must be achieved amid the microstates (hemes with the same number of oxidized hemes) in each redox stage and the kinetic models are, therefore, collisional models, applicable under steady-state conditions where electron transfer is rate-limiting.

Indeed, in such cases, the intricate kinetic array that comprises all feasible microscopic electron transfer steps in a MHC with *N* redox centers may be reduced to a sequence of *N* simple successive macroscopic electron transfer steps, where each step represents the electron transfer in a given center i, with rate constants that carry information of the three steps mentioned above:

$$Protein_{center\ i}^{oxidized} + Electron\ donor^{reduced} \underset{k_{-i}}{\overset{k_{+i}}{\rightleftharpoons}} P_i^{red} + Ed^{ox}$$

The determination of each macroscopic rate constant – that is related to the weighted average of the respective step microscopic constants by one of two rational set of assumptions and Marcus theory of electron transfer – is based on the detailed thermodynamic characterization of the protein (203).

In circumstances of moderate ionic strength, where electrostatic interactions and orientation effects are negligible, Marcus theory may then be applied to express the microscopic rate constants as a function of the driving force (ΔG), the reorganization energy (λ) and factor Z, which has dimensions of collision frequency and accounts for the effect of the medium, the distance between redox centers and the binding constant, according to Equation 2.5:

$$k = Zexp\left[-\frac{(\Delta G+\lambda)^2}{4\lambda RT}\right] \qquad \textbf{Equation 2.5}$$

In one of these sets of assumptions (model 1), redox centers are distinctive in what regards to binding affinity for electron donor and electron transfer parameters (different environment and solvent exposure) and it is realistic to consider different reorganization energies and also Z factors, although these are considered independent of the overall redox state and therefore, solely the driving force changes between steps for a given redox center.

In the other set of assumptions (model 2), redox centers are considered to be equivalent (identical environment and solvent exposure) except in what concerns to their microscopic redox potential and thus, though reorganization energies and Z factors are the same within a given macroscopic redox step, these parameters depend on the overall redox state and may change between steps.

Model 1 is more appropriate for proteins with redox centers under different environment conditions, even though it presents higher constraints as variations in macroscopic rate constants are limited to changes in the driving force of the centers. Model 2 states that the redox centers must have the same

reorganization energies and accessibility, which may not correspond to reality. It is probable that the merging of these simplification models may be a better representative of the real scenario and thus, comparison of the parameters acquired with both should be an insurance for consistency.

Nevertheless, both models require just one variable per redox center as the use of Marcus theory greatly diminishes the number of unknowns, either by considering that factor Z and the reorganization energy are specific of each center but remain unchanged along the reduction process or that Z and λ are the same for all centers within each electron transfer step (203).

CHAPTER 3

ASSIGNMENT OF THE HEME SIGNALS OF THE INDIVIDUAL DOMAINS C AND D AND OF THE TWO DOMAIN FRAGMENT CD FROM GSU1996

Contents

Results presented for the reduced form of domains C and D and of fragment CD from GSU1996 were acquired in the course of the Master Thesis in Biochemistry and presented in Fernandes AP. Caracterização de um novo citocromo do tipo *c* que forma "nanofios" de hemos em *Geobacter sulfurreducens*. Faculdade de Ciências da Universidade de Lisboa; 2012.

A manuscript with the results presented in this chapter is in preparation as: Fernandes AP, Turner DL, Salgueiro C. A biochemical LEGO® strategy to unveil the functional properties of "nanowire" cytochromes.

ABSTRACT

Multiheme *c*-type cytochromes are crucial for extracellular electron transfer in *Geobacter* and *Shewanella* bacteria. This property is currently explored to harvest electricity from aquatic sediments and waste organic matter into microbial fuel cells. To date, the detailed functional characterization of MHCs is restricted to proteins containing up to four hemes. The multiple combinations of electron distribution that can occur among the various hemes and the high molecular weight of larger MHCs had prevented their characterization. The dodecaheme cytochrome GSU1996 composed of four domains (A to D) mediates the electron transfer between periplasmic and outer membrane proteins in the bacterium *G. sulfurreducens*. In the present work, this heme-forming “nanowire” was used as a model to test a biochemical modular strategy aiming to contribute to the biophysical characterization of large MHCs. The assignment of the heme NMR signals, a crucial step to carry out the detailed thermodynamic characterization of MHCs was performed in domains C and D and then used as a guide in the assignment of the hexaheme fragment CD. This strategy allowed for the first time the assignment of the heme substituents in a MHC that contains more than four heme groups, and opens new possibilities for the functional characterization of large MHCs.

INTRODUCTION

The general theoretical framework that allows the detailed study of the properties of the redox centers in multiheme proteins was previously described and was successfully applied to MHCs containing up to four heme groups (190,200,201,219). The first step of this methodology encompasses the assignment of twelve protons per heme group in 2D ^{1}H-NOESY spectra, with the aid of ^{1}H-COSY and ^{1}H-TOCSY spectra. Next, redox titrations monitored by 2D ^{1}H-EXSY are carried out at different pH values and the heme methyl signals of the heme groups are followed through each oxidation stage, from their position in the fully reduced to their final position in the fully oxidized state. In a MHC with N heme groups, the number of oxidation stages – each containing microstates with the same number of oxidized hemes – is N+1 and the total number of microstates is 2^{N} (212,220). For instance, the triheme c_7 cytochromes have a total of four oxidation stages: one for the fully oxidized and another for the fully reduced states and two others that correspond to the protein with one or two oxidized hemes (Figure 3.1). As the c_7 cytochromes may occur in their protonated or deprotonated form, the total number of microstates to consider is $2\times2^{3}=16$ (Figure 3.1). The NMR data combined with the data obtained from visible redox titrations is then used to determine the thermodynamic parameters of the individual redox centers. These include the heme reduction potentials, the pK_a values of the redox-Bohr centers, heme-heme redox interactions and redox-Bohr interactions (200).

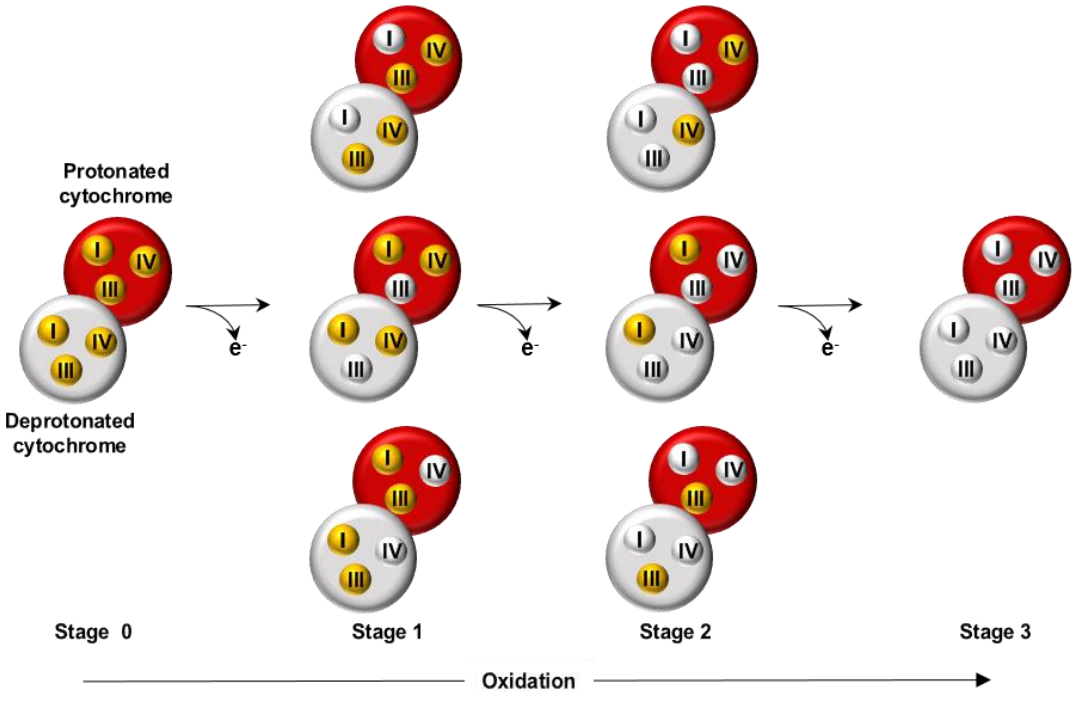

Figure 3.1 – Electronic distribution model for a triheme cytochrome with a proton equilibrium associated. The microstates are grouped according to the number of oxidized hemes (white circles) in four oxidation stages that are linked by three one-electron redox steps. Adapted from Morgado *et al.*, 2012 (259).

However, with the increase of the molecular weight and number of hemes, the quality of the NMR spectra of MHCs decreases as a consequence of signal broadness. To illustrate this, 1D ^{1}H-NMR obtained for a triheme cytochrome and for the dodecaheme cytochrome GSU1996 is compared in Figure 3.2.

Within the framework of the methodology used to characterize MHCs in solution, for a dodecaheme protein it is first necessary to assign a total of 144 heme protons in the fully reduced protein in order to monitor the stepwise oxidation of each heme group along 12 oxidation stages that encompass a total of 8192 microstates. Therefore, such picture prevents the straightforward application of this methodology to characterize MHCs with large number of heme groups.

Given the putative biological importance of the nanowire cytochromes, considerable efforts need to be undertaken in order to characterize them. In the case of GSU1996, the first step encompassed cloning, expression and purification of each triheme domain and hexaheme fragment, as these may theoretically be explored to establish a modular approach towards the thermodynamic characterization of the dodecaheme cytochrome at a microscopic level (192,194,196).

Here, the triheme domains C and D together with fragment CD that compose the C-terminal of GSU1996 were used as a model to validate the proposed modular strategy at the level of the first step of the methodology described above, i.e., the assignment of the heme groups protons.

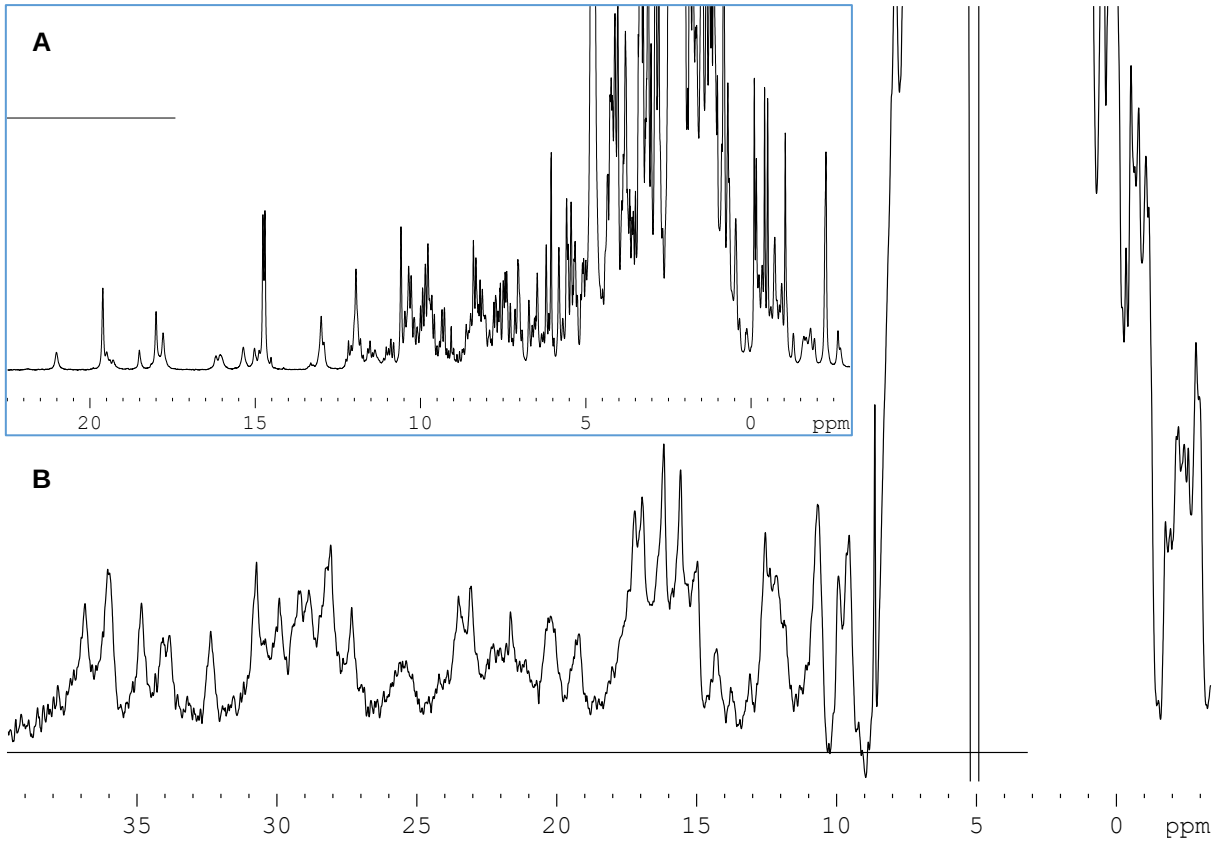

Figure 3.2 – 1D ^{1}H-NMR spectra of A) c_7 cytochrome PpcA and B) dodecaheme cytochrome GSU1996 in the oxidized state, at pH 8.0 and 298.15 K. As can be observed, the triheme cytochrome PpcA presents a well-defined spectrum, with heme methyl signals well defined while the GSU1996 spectrum shows broadening and large profusion of signals, which impairs the straightforward assignment of the heme substituents.

The NMR signals of each domain C and D were assigned and used as a guide in the assignment of the signals from the hexaheme fragment CD in a strategy that allowed for the first time to assign the heme substituents in a MHC with more than four heme groups.

Unlike the C-terminal of GSU1996, the N-terminal part of the biomolecule appears to behave as a structural unit and the attempts to apply this modular approach was unsuccessfully to date. In fact, the individual domains A and B were considerably unstable under all experimental conditions tested, with either low expression yields and/or more than one form in solution that impaired purification and/or spectra analysis.

MATERIALS AND METHODS

Expression and protein purification

The detailed protocol for the expression and purification of the hexaheme fragment AB will be described in CHAPTER 5, under the title Protein expression and purification present in the Materials and Methods section. The GSU1996 triheme domains A, C and D, as well as the hexaheme fragment CD, were expressed and purified as previously described (192,196,221). Briefly, the proteins were expressed in *E. coli* strain JCB7123 (222) harboring plasmid pEC86, which contains the *c*-type cytochromes maturation gene cluster *ccmABCDEFGH* (161). The periplasmic fractions were isolated by osmotic shock in the presence of lysozyme, and dialyzed against 20 mM Tris-HCl buffer pH 8.5 (domain A), 10 mM Tris-HCl buffer pH 7.0 (domains C and D) or 20 mM sodium phosphate (NaPi) buffer pH 5.9 (fragment CD). Samples were separately loaded onto a cation-exchange column (Econo-Pac High S, Bio-Rad) and eluted with a linear gradient of NaCl. In each case, the fractions with the protein of interest were pooled, concentrated and loaded onto a HiLoad 16/600 Superdex 75 column (GE Healthcare), equilibrated with 20 mM NaPi buffer pH 8.0 with 100 mM NaCl salt added. The presence of the desired proteins was confirmed by 12% sodium dodecyl sulfate polyacrilamide gel electrophoresis (SDS-PAGE) stained with Coomassie blue. Both chromatographic steps were performed in an ÄKTA Prime Plus FPLC System (GE, Amersham).

NMR Studies

Samples preparation

The buffer used in the last step of purification was exchanged for 80 mM NaPi buffer pH 8.0 (with NaCl added to a final ionic strength of 250 mM) in 99.9% ^2H_2O (CIL), through ultrafiltration procedures with Amicon Ultra Centrifugal Filter Units (Millipore). Protein concentrations were determined by UV-visible spectroscopy with the specific absorption coefficient of the α-band at 552 nm determined for the reduced triheme cytochrome PpcA ($\Delta\varepsilon_{552\,nm}$ = 32.5 mM^{-1} cm^{-1} per heme) (152) as described in Morgado and co-workers (197). Protein samples with approximately 1.5 mM were placed in 3 or 5 mm Wilmad NMR tubes and closed with NMR pressure caps. The protein samples were degassed with H_2 and reduced as necessary in the presence of catalytic amounts of Fe-hydrogenase isolated from *Desulfovibrio vulgaris* (Hildenborough).

NMR experiments

The NMR spectra were acquired on a Bruker Avance 600 MHz spectrometer at 288.15 K or 298.15 K. In order to assist the assignment of the heme substituent proton signals, 2D ^{1}H-TOCSY and 2D ^{1}H-NOESY NMR spectra were recorded with standard pulse techniques. A series of 2D ^{1}H-TOCSY and 2D ^{1}H-NOESY NMR spectra were acquired with mixing times covering the range of 40-60 ms and 50-400 ms, respectively, for MHCs in both reduced and oxidized states. 2D ^{1}H-^{13}C-HMQC and ^{1}H-^{13}C-HSQC NMR spectra were acquired with 2048 points ranging a spectral width of 37 kHz in the ^{1}H dimension and 512 increments with TPPI to attain a spectral with of 78 kHz in the ^{13}C dimension for the MHCs in the oxidized state. The spectra were calibrated with the water signal as internal reference. Tetramethylsilane constituted the reference for all resonances listed. All NMR spectra were processed using TopSpin™ NMR software from Bruker Biospin and analyzed with resource to the software Sparky 3 (T. D. Goddard and D. G. Kneller, University of California, San Francisco).

Calculation of ring-current shifts

The ring-current shifts calculations followed the procedure described by Turner and co-workers (223) and were calculated with data from the crystal structure of fragment CD (195) by Prof. David Turner (Instituto de Tecnologia Química e Biológica, Universidade Nova de Lisboa). The heme substituent chemical shifts were calculated through correction of the heme protons reference shifts (9.36 ppm for meso protons, 6.13 for thioether methines, 3.48 for methyls, and 2.12 for thioether methyls) as described by Pessanha and co-workers (224).

RESULTS AND DISCUSSION

The crucial step underlying the detailed thermodynamic characterization, and hence the functional mechanisms of MHCs, is the specific assignment of the heme substituents in the structure.

The 1D ^{1}H-NMR spectra of domains C, D and fragment CD are characteristic of low-spin *c*-type cytochromes in both reduced and oxidized states (Figure 3.3). The 1D ^{1}H-NMR spectra of the proteins showed NMR signals covering the regions −4 to 11 ppm and −20 to 40 ppm in the reduced and oxidized states, respectively (Figure 3.3). Thus, from the NMR studies it can be concluded that domains C, D and fragment CD are diamagnetic when reduced (Fe(II), $S = 0$) and paramagnetic when oxidized (Fe(III), $S = \frac{1}{2}$). Indeed, the pattern and linewidths of the NMR signals are clearly distinct from those of high-spin cytochromes (209). In the latter, in the oxidized state, the 1D ^{1}H-NMR spectra show extremely broad signals above 40 ppm. Similarly, for reduced high-spin cytochromes the 1D ^{1}H-NMR spectra show wider spectral regions (typically from −15 up to 30 ppm). Such profiles are not observable for the triheme domains and fragment CD. By simple observation of the more shifted signals in the reduced and oxidized spectra of these proteins, it is clear that the NMR signals in the fragment follow closely the dispersion of the signals in the individual triheme domains (Figure 3.3). There is remarkable similarity for the signals of axial methionine 209 and 287 of hemes IV in domains C and D, respectively.

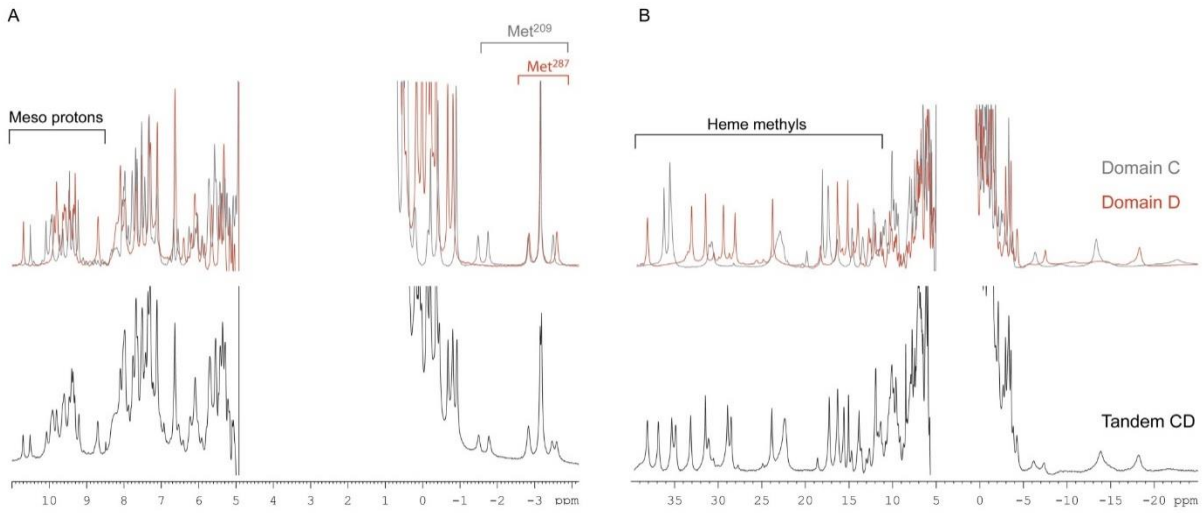

Figure 3.3 – 1D ^{1}H-NMR spectra acquired for domains C and D (respectively gray and red, in the upper panel) and fragment CD (black, lower panel) in the reduced (A) and oxidized (B) state at pH 8.0 and 288.15 K. The typical regions for meso and heme axial methionine side chain protons are indicated in the reduced spectra. In the oxidized spectra the typical regions for heme methyl signals are also indicated.

The typical pattern of heme axial methionine resonances includes a three-proton intensity peak at approximately −3 ppm and up to four resolved one-proton intensity peaks in the low-frequency region of the reduced spectrum (138,225). Due to the paramagnetic effect of the unpaired electrons these signals are even more shifted and broader in the oxidized NMR spectra (see spectral region −20 to −5 ppm). However, the spectral resolution is high enough to show that the geometry of the axial ligands in the individual domains is conserved in the fragment CD (Figure 3.3).

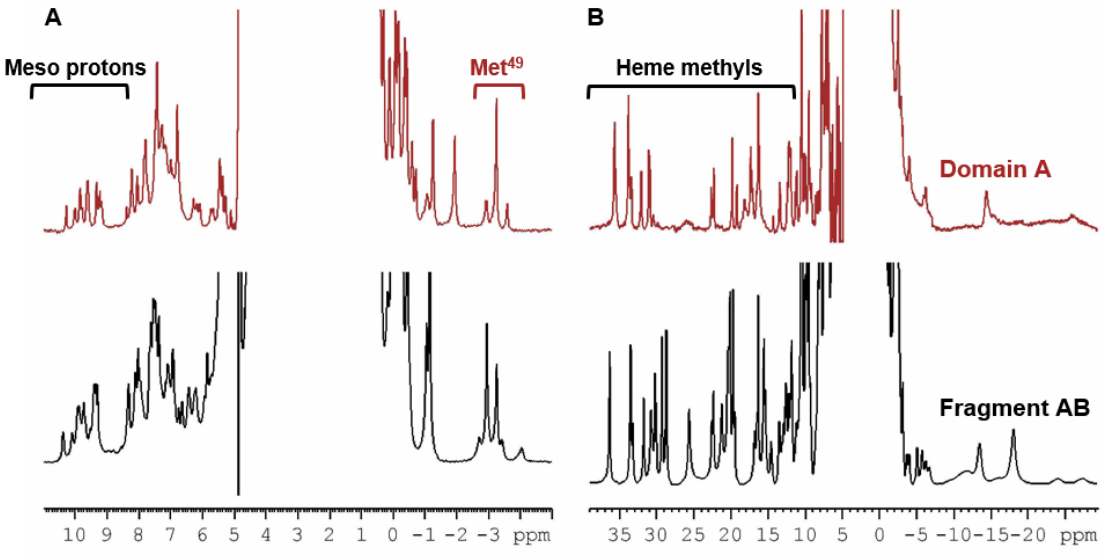

Figure 3.4 – 1D ^{1}H-NMR spectra acquired for domain A (red curve in the upper panel) and fragment AB (black curve in the lower panel) in the reduced (A) and oxidized state (B) at pH 8.0 and 298.15 K. The typical regions for meso and heme axial methionine side chain protons are indicated in the reduced spectra and the typical regions for heme methyl signals are indicated in the oxidized spectra.

A similar discussion may be carried in the case of the N-terminal of the molecule, with some repairs. Unlike in the C-terminal end, it was not possible to obtain the individual domain B, as its expression levels are very low and the purification process was not yet optimized (221). In the case of domain A and fragment AB, the 1D ^{1}H-NMR spectra are also typical of low-spin *c*-type cytochromes in both reduced and oxidized states (Figure 3.4), with NMR signals that range from –4.5 to 10.5 ppm in the reduced state and –29 to 38 ppm in the oxidized state. NMR chemical shifts in the fragment AB are comparable to the ones in the individual domain A (Figure 3.4). The signal of axial methionine 49 of heme IV in domain A is close to the one observed in fragment AB and endorses that the axial geometry of the heme axial ligand is conserved in the fragment AB (Figure 3.4). As observed in the C-terminal, chemical shifts appear altered and broader in the oxidized NMR spectra (see spectral region −20 to −5 ppm). On the other hand, a closer observation of the spectra indicated that domain A occurs in more than one conformation in solution, as the number of signals for triheme domain A appear to be exceeded relative to predicted (Figure 3.5).

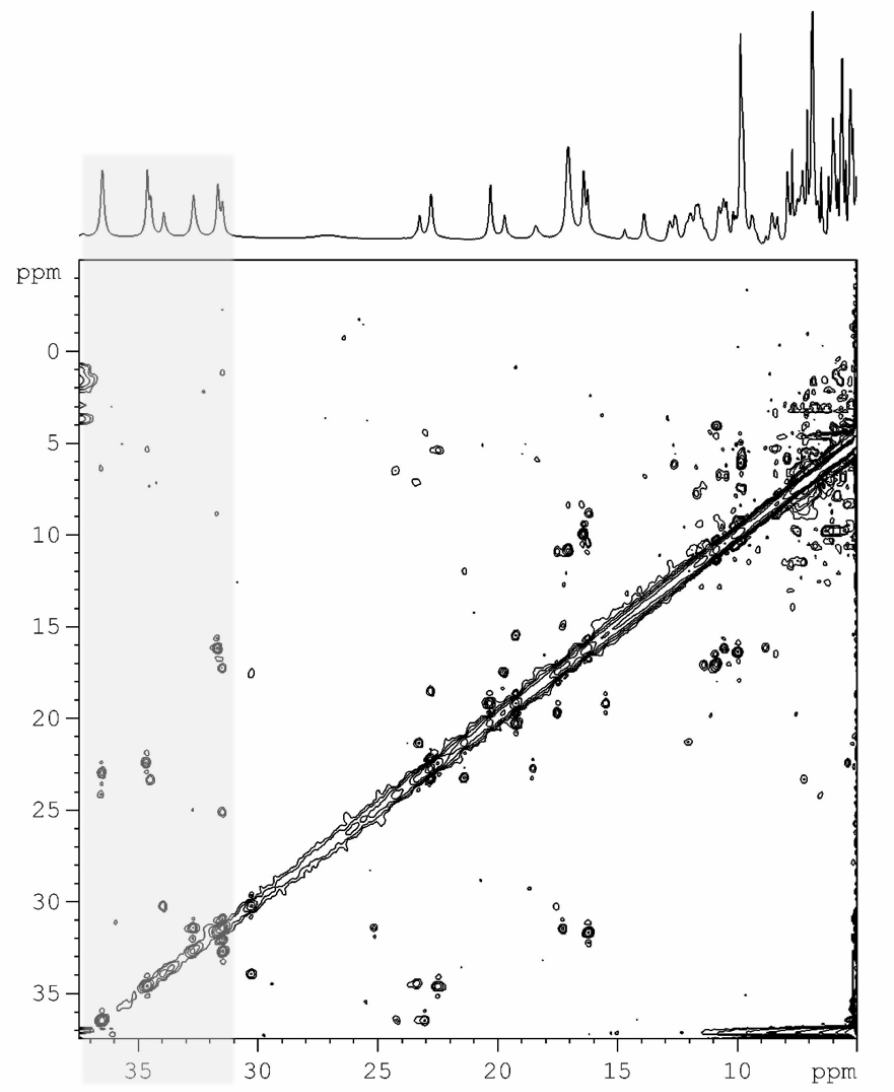

Figure 3.5 – 1D ^{1}H-NMR spectra acquired for domain A (above) and 2D ^{1}H-EXSY (below, (221)**) in the oxidized state at pH 8.0 and 289.15 K.** The shadowed region exemplifies heme methyl signals that may belong to two different conformations of domain A in solution.

Unfortunately, this precludes the signal assignment of domain A and, together with the absence of domain B, the assignment of fragment AB is impaired, as the profusion and broadness of signals are quite large to unequivocally allow the attribution of the signals. The assignment of the domains C and D and fragment CD in both states is described in more detail in the next section.

Reduced state

Assignment of the heme ^{1}H signals in domain D

The assignment of the heme protons of domain C in the reduced state was already described in detail in previous work (197) and it is not discussed here. Domain D will be used as an illustration towards the understanding of the assignment process in a MHC in the reduced state (221).

The heme proton resonances in the reduced state of domain D were identified following the strategy previously described for multiheme ferrocytochromes (223). In the diamagnetic state the heme proton signals appear in quite typical regions, according to their type. These are 11–8 ppm for meso protons (5H, 10H, 15H and 20H) ; 8–5 ppm for thioether methine (3^{1}H and 8^{1}H); 5–2.5 ppm for heme methyls ($2^{1}CH_3$, $7^{1}CH_3$, $12^{1}CH_3$ and $18^{1}CH_3$) and 3–(−1.0) ppm for thiother methyls ($3^{2}CH_3$ and $8^{2}CH_3$) (Figure 3.6 A, C) (201,223,224,226–232). Among these substituents, the only protons that show scalar coupling are the pairs thioether methine/thioether methyls ($3^{1}H/3^{2}CH_3$ and $8^{1}H/8^{2}CH_3$), which were firstly identified in the 2D ^{1}H-TOCSY NMR spectra (Figure 3.6 B). Next, the distinctive pattern of short-range intraheme connectivities between meso protons and neighboring substituents were identified in the 2D ^{1}H-NOESY NMR spectra acquired with short mixing-times (50–100 ms). As illustrated (see full lines in Figure 3.6 C), meso protons 20H are connected only to two heme methyls ($2^{1}CH_3$ and $18^{1}CH_3$) and meso protons 15H show no connections to heme methyls or thioether substituents. Meso protons 5H and 10H are connected to heme methyls, thioether methines and also thioether methyls. Since they have the same pattern of NOE connectivities, the distinction between meso protons 5H and 10H can be achieved by inspection of the connectivities between the heme substituents $2^{1}CH_3/3^{2}CH_3$ and $7^{1}CH_3/8^{2}CH_3$. As an example, the short-range intraheme NOE connectivities for heme III meso protons are indicated in Figure 3.6 A. 2D ^{1}H-NOESY experiments performed with a mixing time in the range 150–400 ms allowed the observation of the long-range intraheme connectivities and further confirmed the assignment of the signals. The heme proton signals of domains C and D in the diamagnetic state are listed in Table 3.1.

Cross-assignment of the hemes to the structure of domain D

We then moved to the assignment of the heme signals to its specific hemes. In order to achieve this, the ^{1}H chemical shifts of domain D were compared to those calculated from the crystal structure of fragment CD (Figure 3.7 and Table 3.S1). From the six possible permutations for the three sets of heme protons with respect to the crystal structure, one was clearly preferred since all hemes concurrently showed the smallest root mean square deviation (rmsd). The rmsd of the 36 shifts was 0.10 ppm, with deviations of 0.02 (heme I), 0.04 (heme III) and 0.04 (heme IV). As in the case of domain C (197), the observed and predicted shifts correlate very well, even for the protons subjected to the larger ring

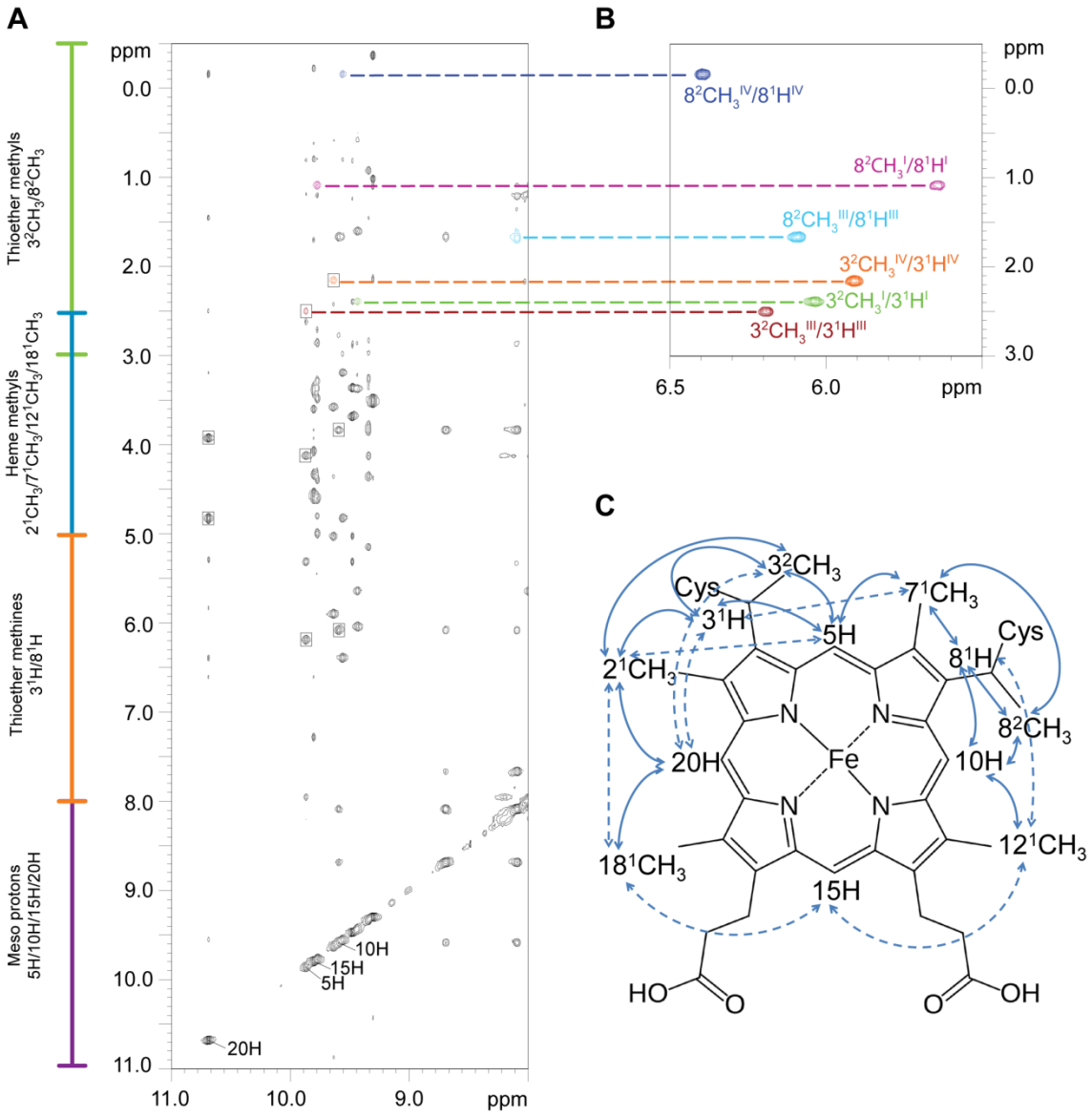

Figure 3.6 – Summary of the methodology used in the assignment of the reduced state of domain D heme substituents. (A) Expansion of the 2D ^{1}H-NOESY NMR spectrum region that shows the intraheme NOE connectivities of meso protons. In order to not overcrowd the figure, only the short-range connectivities for heme III meso protons (identified according to panel C) are boxed; (B) Expansion of the 2D ^{1}H-TOCSY NMR spectrum region that contains the thioether methine/thioether methyls scalar connectivities. The dashed lines connect these signals with the correspondent ones in the 2D ^{1}H-NOESY NMR spectrum; (C) Diagram of heme *c* numbered according to the IUPAC-IUB nomenclature (136). The full lines show the heme protons involved in the short-range connectivities, which are easily detected in the 2D ^{1}H-NOESY NMR spectra acquired with 50–100 ms mixing-time. Dashed lines indicate the long-range NOE connectivities also observed in the 2D ^{1}H-NOESY NMR spectra acquired with higher mixing-time values.

current effects, as it is the case of the protons 10H^{I}, 20H^{III}, 2^{1}CH$_3^{III}$, 12^{1}CH$_3^{I}$, 8^{2}CH$_3^{I}$ and 8^{2}CH$_3^{IV}$ (*cf.* Figure 3.7 and Table 3.1).

The assignment of domain D heme substituents was further tested by examination of the interheme NOE connectivities from the 2D ^{1}H-NOESY spectra and their comparison with the distances obtained from the crystal structure of fragment CD. All NOE connectivities between protons up to 3 Å apart were observed in the 2D ^{1}H-NOESY spectra, which confirms that both crystal and solution structures are similar.

Table 3.1 – Observed ^{1}H chemical shifts (ppm) and ring current shifts (in parentheses) of the heme substituents of domains C, D and fragment CD in the diamagnetic state at pH 8.0 and 288.15 K (197,221)**.**

Heme substituent	Protein		Heme I	Heme III	Heme IV
5H	*Domain C*		9.49 (−0.13)	9.94 (−0.58)	9.73 (−0.37)
	Domain D		9.44 (−0.08)	9.87 (−0.51)	9.64 (−0.28)
	Fragment CD	C	9.47 (−0.11)	9.93 (−0.57)	9.65 (−0.29)
		D	9.47 (−0.11)	9.89 (−0.53)	9.65 (−0.29)
10H	*Domain C*		8.01 (1.35)	10.09 (−0.73)	9.64 (−0.28)
	Domain D		7.99 (1.37)	9.59 (−0.23)	9.56 (−0.20)
	Fragment CD	C	8.00 (1.36)	10.08 (−0.72)	9.60 (−0.24)
		D	8.02 (1.34)	9.63 (−0.27)	9.58 (−0.22)
15H	*Domain C*		9.37 (−0.01)	9.96 (−0.60)	9.99 (−0.63)
	Domain D		9.34 (0.02)	9.80 (−0.44)	9.77 (−0.41)
	Fragment CD	C	9.36 (0.00)	9.96 (−0.60)	9.96 (−0.60)
		D	9.32 (0.04)	9.81 (−0.45)	9.78 (−0.42)
20H	*Domain C*		9.23 (0.13)	10.51 (−1.15)	9.46 (−0.10)
	Domain D		9.48 (−0.12)	10.69 (−1.33)	9.31 (0.05)
	Fragment CD	C	9.21 (0.15)	10.51 (−1.15)	9.36 (0.00)
		D	9.40 (−0.04)	10.70 (−1.34)	9.32 (0.04)
$2^{1}CH_3$	*Domain C*		3.59 (−0.11)	4.74 (−1.26)	3.65 (−0.17)
	Domain D		3.69 (−0.21)	4.83 (−1.35)	3.55 (−0.07)
	Fragment CD	C	3.56 (−0.08)	4.74 (−1.26)	3.61 (−0.13)
		D	3.75 (−0.27)	4.85 (−1.37)	3.55 (−0.07)
$7^{1}CH_3$	*Domain C*		3.45 (0.03)	4.18 (−0.70)	3.64 (−0.16)
	Domain D		3.38 (0.10)	4.13 (−0.65)	3.59 (−0.11)
	Fragment CD	C	3.43 (0.05)	4.17 (−0.69)	3.64 (−0.16)
		D	3.42 (0.06)	4.18 (−0.70)	3.60 (−0.12)
$12^{1}CH_3$	*Domain C*		1.42 (2.06)	3.88 (−0.40)	2.91 (0.57)
	Domain D		1.20 (2.28)	3.84 (−0.36)	3.20 (0.28)
	Fragment CD	C	1.40 (2.08)	3.87 (−0.39)	2.87 (0.61)
		D	1.22 (2.26)	3.85 (−0.37)	3.21 (0.27)
$18^{1}CH_3$	*Domain C*		3.39 (0.09)	3.68 (−0.20)	3.51 (−0.03)
	Domain D		3.37 (0.11)	3.93 (−0.45)	3.49 (−0.01)
	Fragment CD	C	3.38 (0.10)	3.68 (−0.20)	3.51 (−0.03)
		D	3.55 (−0.07)	3.94 (−0.46)	3.49 (−0.01)
$3^{1}H$	*Domain C*		6.03 (0.10)	6.26 (−0.13)	5.91 (0.22)
	Domain D		6.04 (0.09)	6.19 (−0.06)	5.91 (0.22)
	Fragment CD	C	6.02 (0.11)	6.25 (−0.12)	5.72 (0.41)
		D	6.09 (0.04)	6.22 (−0.09)	5.92 (0.21)
$8^{1}H$	*Domain C*		5.75 (0.38)	6.55 (−0.42)	6.09 (0.04)
	Domain D		5.65 (0.48)	6.09 (0.04)	6.40 (−0.27)
	Fragment CD	C	5.74 (0.39)	6.54 (−0.41)	6.09 (0.04)
		D	5.70 (0.43)	6.12 (0.01)	6.42 (−0.29)
$3^{2}CH_3$	*Domain C*		2.37 (−0.25)	2.69 (−0.57)	2.16 (−0.04)
	Domain D		2.40 (−0.28)	2.51 (−0.39)	2.17 (−0.05)
	Fragment CD	C	2.35 (−0.23)	2.66 (−0.54)	1.69 (0.43)
		D	2.46 (−0.34)	2.54 (−0.42)	2.18 (−0.06)
$8^{2}CH_3$	*Domain C*		1.36 (0.76)	1.86 (0.26)	−0.41 (2.53)
	Domain D		1.10 (1.02)	1.67 (0.45)	−0.15 (2.27)
	Fragment CD	C	1.36 (0.76)	1.85 (0.27)	−0.44 (2.56)
		D	1.13 (0.99)	1.70 (0.42)	−0.12 (2.24)

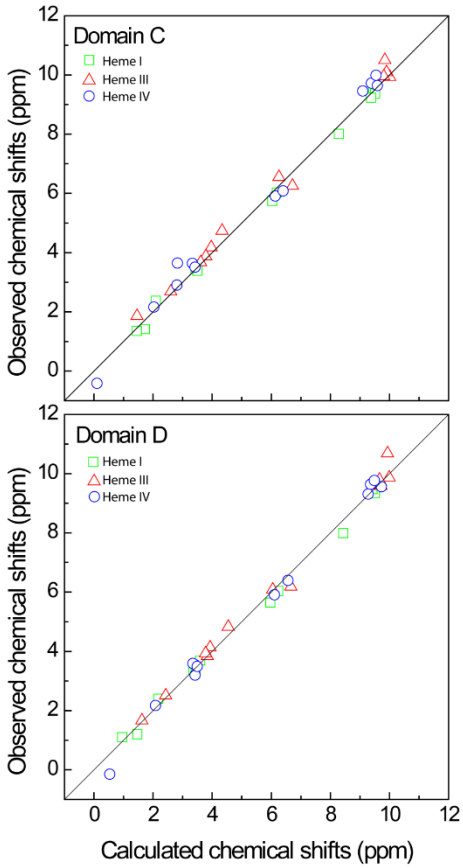

Figure 3.7 – Comparison between the observed and calculated chemical shifts for all the heme substituents of domains C and D. Hemes I, III, and IV are represented by squares, triangles and circles, respectively. The calculated values were obtained from the crystal structure of the fragment CD (PDB code 3OUE (195)). The solid line has a unit slope. The rmsd between the observed and calculated proton chemical shifts are 0.02 (heme I), 0.05 (heme III) and 0.07 (heme IV) for domain C and 0.02 (heme I), 0.04 (heme III) and 0.04 (heme IV) for domain D (221).

The crystal structures showed that domains C and D have several aromatic side chains in the vicinity of the heme groups (Figure 3.8).

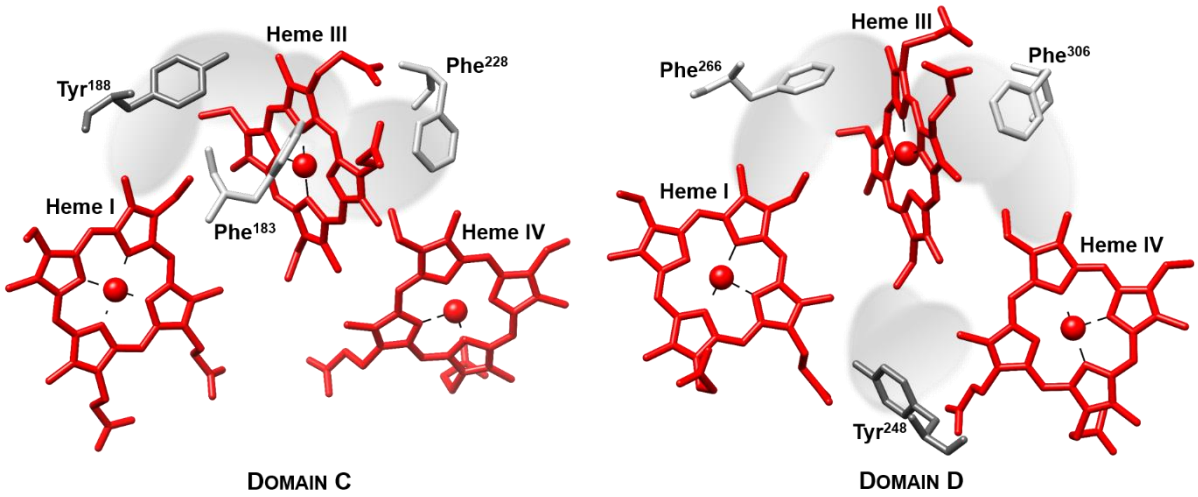

Figure 3.8 – Location of aromatic residues in the heme core of domains C and D. The residues are indicated in gray and hemes in red. Shadowed areas indicate the observed NOE connectivities in the 2D ^{1}H-NMR spectra. Figures of the heme core of domains C and D were produced with the UCSF Chimera package (320) from PDB file 3OUE (195).

Among these, Phe^{183} (close to heme III), Tyr^{188} (near hemes I and III) and Phe^{228} (near hemes III and IV) were identified in domain C and Tyr^{248} (near hemes III and IV), Phe^{266} (near hemes I and III) and Phe^{306} (near hemes III and IV) in domain D. The aromatic signals of these residues were identified in the 2D ^{1}H-TOCSY spectrum and used to further test the assignment of the heme substituents.

The expected NOE connectivities between aromatic and heme substituent signals were observed in the 2D ^{1}H-NOESY and thus confirm the assignment made (see shadowed areas in Figure 3.8).

Assignment of the heme proton signals in fragment CD

The fragment CD has twice the number of heme groups and molecular weight compared to the individual domains. Consequently, due to the slow correlation time of the fragment in solution, the NMR signals are broader and the intensity of the NOE connectivities are smaller when compared to those in the individual domains. The high number of heme signals together with the signal broadness hinders the straightforward application of the methodology described for the assignment of the heme substituents in the individual domains. However, as discussed, the signals of the fragment CD in the 1 D ^{1}H-NMR spectra correspond to the cumulative pattern of the heme signals of each individual domain (Figure 3.3). Thus, in the present work the assigned heme signals of the individual domains in the 2D ^{1}H-TOCSY and 2D ^{1}H-NOESY spectra were used as a guide to their assignment in the fragment CD (Figure 3.9). The assignment of the heme signals in the fragment CD is indicated in the Table 3.1. As described above for domain D, the assignment was tested by comparison of the observed heme proton chemical shifts with those calculated using the crystal structure of fragment CD (Table 3.S1). Also for the fragment CD, the chemical shifts correlate very well, even for the protons that withstand large ring current shifts (Figure 3.10). The interheme NOE connectivities observable in the 2D ^{1}H-NOESY spectra were examined and compared with the distances obtained from the crystal structure. All the expected NOE connectivities between the closest protons were observed in the 2D ^{1}H-NOESY spectra and validate the strategy used in the present work to assign the heme signals in proteins with a large number of heme groups.

Oxidized state

Assignment of the heme proton signals in domains C and D

As explained above, the dispersion of signals in the oxidized state is larger compared to the reduced state, which makes their assignment much more complex and difficult to achieve. Consequently, the strategy described for the assignment of the heme substituent signals in the reduced form, based on the exclusive analysis of 2D ^{1}H-TOCSY and 2D ^{1}H-NOESY NMR spectra is insufficient. However, when such type of experimental data are combined with data obtained from 2D ^{1}H-^{13}C-HSQC or ^{1}H-^{13}C-HMQC spectra the assignment becomes more straightforward and some of the heme signals can be specifically attributed. In fact, these spectra may be used to assist the assignment of the heme substituent signals, since the dipolar shifts of the carbon nuclei attached to the pyrrole β-carbons are very small and, in contrast with the protons bonded to them, their Fermi contact shifts are directly proportional to the spin density on the pyrrole β-carbons (233,234).

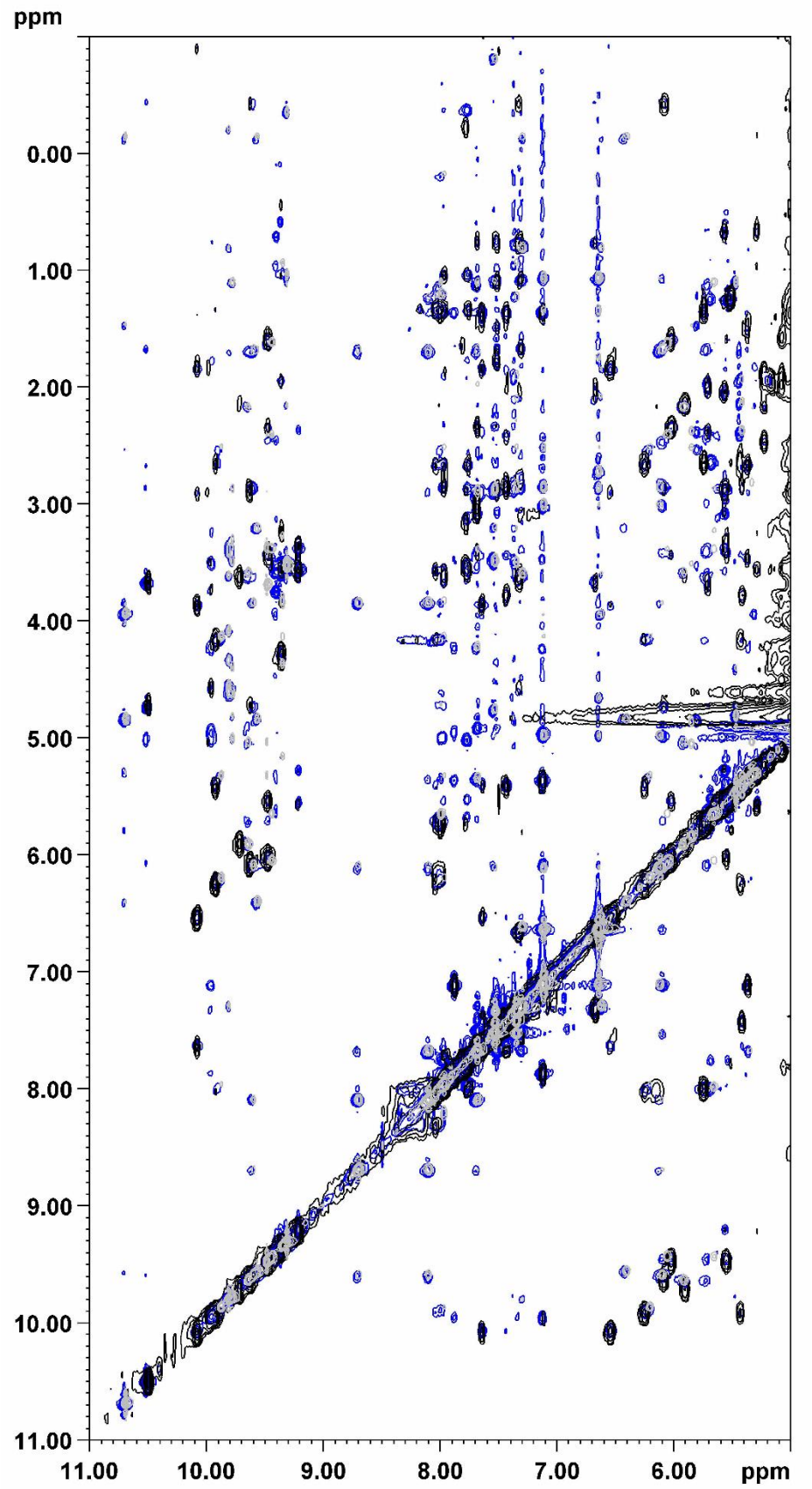

Figure 3.9 – Overlay from part of the 2D ^{1}H-NOESY spectra acquired for domain C (black), domain D (gray) and fragment CD (dark blue) in the reduced state at pH 8.0 and 288.15 K. As already observed in the 1D ^{1}H-NMR spectra, fragment CD spectrum reflects a cumulative pattern from the spectra acquired for both domains.

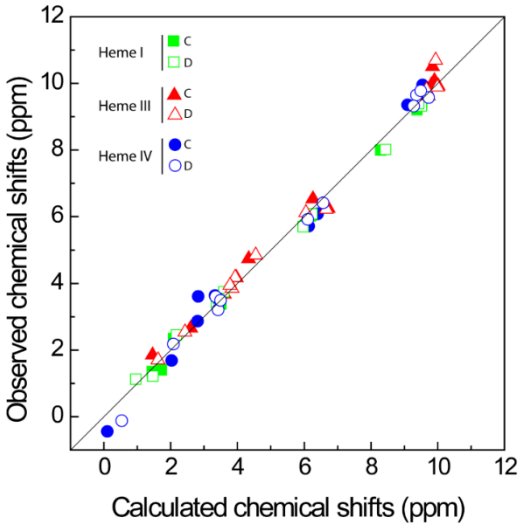

Figure 3.10 – Comparison between the observed and calculated chemical shifts for all the heme substituents of fragment CD. Heme I, III, and IV are represented by squares, triangles and circles, respectively. The calculated values were obtained from the crystal structure of the fragment CD as described in the materials and methods section. The heme signals that correspond to domains C and D are represented by filled and open symbols, respectively. The solid line has a unit slope. The rmsd between the observed and calculated proton chemical shifts are 0.02 (heme I), 0.05 (heme III) and 0.07 (heme IV) for domain C and 0.02 (heme I), 0.04 (heme III) and 0.03 (heme IV) for domain D (221).

Thus, in the ^{13}C dimension, typical regions for the signals of the heme substituents can be easily identified as illustrated with the ^{1}H-^{13}C-HSQC NMR spectrum obtained for domain D (Figure 3.11).

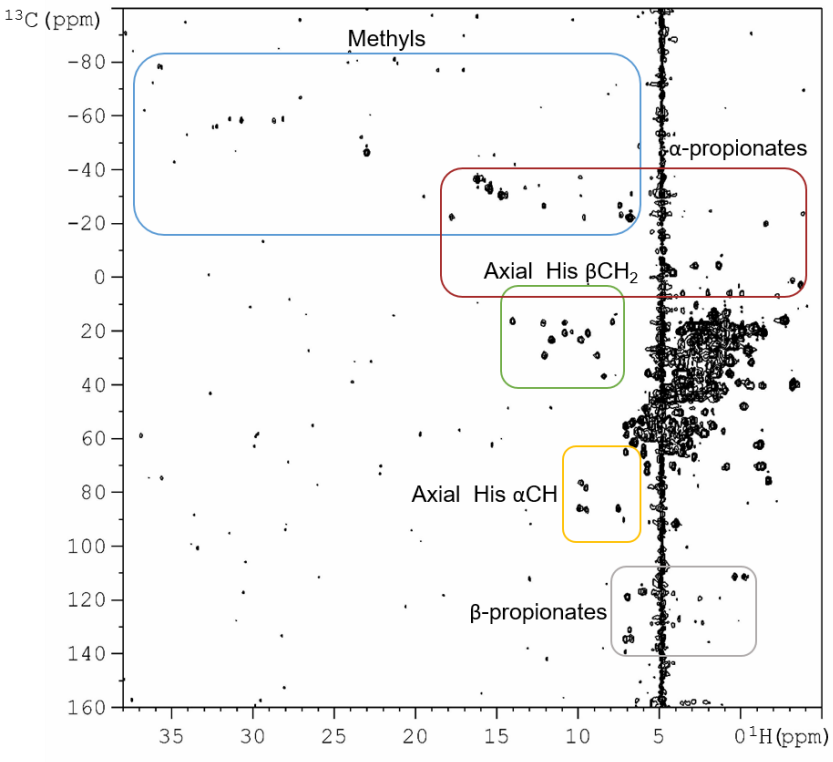

Figure 3.11 – Expansion of the 2D ^{1}H-^{13}C-HSQC spectrum acquired for the oxidized domain D at pH 8.0 and 298.15 K illustrates the typical regions for the signals of the heme substituents in an oxidized cytochrome.

The assignment of the heme protons of domains C and D in the oxidized state followed the spectra analysis described by Turner *et al.* (233) by combining the information gathered from 2D ^{1}H-^{13}C HSQC, 2D ^{1}H-TOCSY and 2D ^{1}H-NOESY spectra and is summarized in Table 3.2 and Table 3.3.

In the case of domain C, 2D ^{1}H-EXSY data previously obtained (197) served as a guide in the identification of several of the heme methyl signals in the 2D ^{1}H-^{13}C HSQC spectra. The remaining heme methyl signals were identified first in the 1D ^{1}H-NMR spectra by observation of the expected intensities for methyl groups (Figure 3.3 B) and then located in the 2D ^{1}H-^{13}C HSQC spectra, as they appear in typical regions and signals usually show large intensities (Figure 3.11). Unfortunately, no data from 2D ^{1}H-EXSY spectra was recovered for domain D, as the slow intermolecular exchange regime on the NMR time scale was not achieved in neither experimental conditions attempted in earlier work (221). Therefore, heme methyl signals assignment in domain D was initially performed with resource solely to 1D ^{1}H-NMR spectra (Figure 3.3 B) and further confirmed in 2D ^{1}H-^{13}C HSQC spectra (Figure 3.11). 18^{1}CH$_3$ heme methyl is in close vicinity of the heme methyl 2^{1}CH$_3$ and this reflects a distinctive connectivities pattern from 12^{1}CH$_3$ heme methyl in the spectra. 7^{1}CH$_3$ heme methyl signals may be more defying to locate, as they may appear in more unusual regions and the connectivity patterns in 2D NMR spectra are also difficult to identify with certainty.

The assignment of the signals of the heme propionates is generally straightforward, as they appear paired in defined regions of the 2D ^{1}H-^{13}C HSQC spectra (Figure 3.11) and scalar coupling patterns are afterwards located in the 2D ^{1}H-TOCSY NMR spectra.

Following heme methyl and heme propionate signals identification, the characteristic pattern of short-range intraheme connectivities between heme methyl 12^{1}CH$_3$ and 18^{1}CH$_3$ and the respective heme propionate legs were located in the 2D ^{1}H-NOESY spectra (see heme *c* diagram in Table 3.3).

Table 3.2 – Observed ^{1}H-^{13}C chemical shifts (ppm) and ring current shifts (in parentheses) of the heme substituents of domains C, D and fragment CD in the paramagnetic state at pH 8.0 and 298 K. The resonances not assigned are labelled as n. a.. Yellow shadowing refers to heme methyl shifts that could not be specifically assigned to hemes I or IV. Gray shadowing refers to connectivities that may belong to heme methyls 18^{1}CH$_3$ or 2^{1}CH$_3$ from hemes I or IV but could not also be specifically attributed.

Heme substituent	Protein		Heme I		Heme III		Heme IV	
			^{1}H	^{13}C	^{1}H	^{13}C	^{1}H	^{13}C
2^{1}CH$_3$	*Domain C*		21.85	n. a.	17.36	−37.53	34.60	−61.46
	Domain D		22.99/ 32.22/14.73	−46.21/ −55.99/−20.28	16.16	−36.33	22.99/ 32.22/14.73	−46.21/ −55.99/−20.28
	Fragment CD	C	21.81	n. a	17.06	−39.86	34.31	−63.96
		D	22.83/ 32.04/14.72	−47.58/ −58.37/−32.83	15.98	−38.63	22.83/ 32.04/14.72	−47.58/ −58.37/−32.83
7^{1}CH$_3$	*Domain C*		n. a.	n. a.	n. a.	n. a.	n. a.	n. a.
	Domain D		n. a.	n. a.	n. a.	n. a.	n. a.	n. a.
	Fragment CD	C	n. a.	n. a.	n. a.	n. a.	n. a.	n. a.
		D	n. a.	n. a.	n. a.	n. a.	n. a.	n. a.
12^{1}CH$_3$	*Domain C*		22.14	n. a.	34.54	−59.01	35.43	−67.28
	Domain D		30.70	−58.08	15.37	−32.64	37.07	−71.23
	Fragment CD	C	21.81	n. a	33.44	−63.26	35.79	−71.56
		D	30.44	−60.32	15.30	−35.21	36.77	−72.58
18^{1}CH$_3$	*Domain C*		30.09	n. a.	12.62	−28.10	18.69	−35.63
	Domain D		28.70/ 32.22/14.73	−57.98/ −55.99/−20.28	26.98	−67.10	28.70/ 32.22/14.73	−57.98/ −55.99/−20.28
	Fragment CD	C	29.65	−59.87	12.52	−31.05	16.37	−35.66
		D	27.74/ 32.04/14.72	−59.32/ −58.37/−32.83	27.40	−69.85	27.74/ 32.04/14.72	−59.32/ −58.37/−32.83

Table 3.3 – Observed ^{1}H-^{13}C chemical shifts (ppm) of the heme propionates of domains C, D and fragment CD in the paramagnetic state at pH 8.0 and 298.15 K. The resonances not assigned are labelled as n. a.. In Domain D entries, yellow shadowing refers to connectivities that belong to the same spin system, although it was not possible to assign them specifically to hemes I or IV.

		Domain C						***Domain D***					
		Heme I		Heme III		Heme IV		Heme I		Heme III		Heme IV	
	Heme propionate	^{1}H	^{13}C	^{1}H	^{13}C	^{1}H	^{13}C	^{1}H	^{13}C	^{1}H	^{13}C	^{1}H	^{13}C
18^{1}CH$_3$	**β$_1$CH$_2$**	1.91	63.86	−2.40	65.63	2.32	72.24	n. a.	n. a.	n. a.	n. a.	n. a.	n. a.
	β$_2$CH$_2$	2.33	63.86	−1.92	65.63	2.74	72.24	n. a.	n. a.	n. a.	n. a.	n. a.	n. a.
	α$_1$CH$_2$	3.14	3.41	0.47	−2.08	−1.64	4.43	3.53	6.32	1.98	6.25	3.53	6.32
	α$_2$CH$_2$	3.49	3.41	0.76	−2.08	6.44	4.43	−0.10	6.32	0.64	6.25	−0.10	6.32
12^{1}CH$_3$	**β$_1$CH$_2$**	0.75	52.69	0.40	128.77	2.07	110.53	−0.25	111.57	−1.41	70.48	2.47	119.76
	β$_2$CH$_2$	1.23	52.69	2.59	128.77	3.13	110.53	0.34	111.57	−1.18	70.48	3.88	119.76
	α$_1$CH$_2$	2.56	n. a.	8.85	−31.38	6.86	−18.16	7.41	−26.49	2.74	−4.14	9.60	−22.18
	α$_2$CH$_2$	3.28	n. a.	16.78	−31.38	19.70	−18.16	12.08	−26.49	1.30	−4.14	17.76	−22.18

		Fragment CD											
		Domain C						*Domain D*					
		Heme I		Heme III		Heme IV		Heme I		Heme III		Heme IV	
	Heme propionate	^{1}H	^{13}C	^{1}H	^{13}C	^{1}H	^{13}C	^{1}H	^{13}C	^{1}H	^{13}C	^{1}H	^{13}C
18^{1}CH$_3$	**β$_1$CH$_2$**	n. a.	n. a.	−2.41	65.57	n. a.	n. a.	n. a.	n. a.	n. a.	n. a.	n. a.	n. a.
	β$_2$CH$_2$	n. a.	n. a.	−1.97	65.57	n. a.	n. a.	n. a.	n. a.	n. a.	n. a.	n. a.	n. a.
	α$_1$CH$_2$	n. a.	n. a.	0.39	−2.42	n. a.	n. a.	2.67	8.32	n. a.	n. a.	2.67	8.32
	α$_2$CH$_2$	n. a.	n. a.	0.57	−2.42	n. a.	n. a.	−0.73	8.32	n. a.	n. a.	−0.73	8.32
12^{1}CH$_3$	**β$_1$CH$_2$**	n. a.	n. a.	0.33	128.58	n. a.	n. a.	−0.17	111.86	−1.43	70.26	2.45	n. a.
	β$_2$CH$_2$	n. a.	n. a.	2.53	128.58	n. a.	n. a.	0.35	111.86	−1.19	70.26	3.87	n. a.
	α$_1$CH$_2$	n. a.	n. a.	8.78	−31.02	n. a.	n. a.	7.58	−26.63	2.65	−4.05	9.37	−22.73
	α$_2$CH$_2$	n. a.	n. a.	16.58	−31.02	n. a.	n. a.	11.99	−26.63	1.25	−4.05	18.01	−22.73

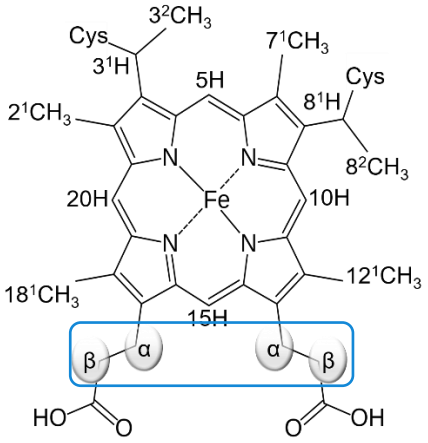

The chemical shifts of the histidine axial ligands of the hemes were also attributed (Table 3.4). Initially, these were located in the 2D ^{1}H-^{13}C-HSQC or ^{1}H-^{13}C-HMQC spectra, as they appear in typical uncrowded regions of the spectra (Figure 3.11) and next, histidine scalar coupling patterns were identified in the 2D ^{1}H-TOCSY NMR spectra.

Cross-assignment of the hemes to the structures of domains C and D

The specific assignment of the heme substituents of domains C and D to the structure was obtained by inspection of the observed interheme NOE connectivities in the 2D ^{1}H-NOESY spectra and the distances taken from crystal structures of domain C and fragment CD, as described for the reduced state. In the paramagnetic state, predicted heme methyl signals (Table 3.S2) did not correlate well with

the signals observed in the spectra and that appear up to approximately 37 ppm. Several NOE connectivities between protons up to 3 Å apart were observed in the 2D ^{1}H-NOESY spectra, which endorses the similarity between crystal and solution structures.

Assignment of the heme proton signals in fragment CD

The assignment of the chemical shifts in the oxidized form of fragment CD was accomplished as described before for the reduced form. Therefore, the assignment of the individual domains were used as guide to assist in the assignment of fragment CD.

In general, chemical shifts correlate very well, even for the protons withstanding large ring current shifts. The major variations were observed for domain C, and heme methyl $18^{1}CH_{3}^{IV}$ that is at the interface between domains C and D in the fragment CD showed the largest deviation (Table 3.2). Probably due their mobility in solution and rearrangement in the fragment CD, some of the domain C heme propionates had no correspondence in the fragment CD (Table 3.3). The interheme NOE connectivities observable in the 2D ^{1}H-NOESY spectra were examined and compared with the distances obtained from the crystal structure. Several of the NOE connectivities between the closest protons were observed in the 2D ^{1}H-NOESY spectra and corroborate the strategy used in the present work to assign the heme signals in MHCs with a large number of heme groups.

Table 3.4 – Observed ^{1}H-^{13}C chemical shifts (ppm) of the histidine axial ligands of domains C, D and fragment CD in the paramagnetic state at pH 8.0 and 298.15 K. The resonances not assigned are labelled as n. a..

Histidine axial ligands		β_1CH_2		β_2CH_2		αCH	
		^{1}H	^{13}C	^{1}H	^{13}C	^{1}H	^{13}C
Domain C		10.52	22.56	9.16	22.56	9.41	85.78
		10.79	22.77	9.88	22.77	7.69	78.05
		13.00	29.35	8.96	29.35	9.61	77.19
		14.07	14.06	7.98	14.06	9.18	82.20
		n. a.	n. a.	n. a.	n. a.	n. a.	n. a.
Domain D		10.79	21.00	9.36	21.00	7.51	86.27
		11.60	23.56	9.78	23.56	9.90	86.16
		12.04	29.24	8.76	29.24	9.74	76.81
		12.13	17.08	10.82	17.08	9.46	86.65
		14.00	16.68	7.86	16.68	9.48	78.65
Fragment CD	C	10.51	22.48	9.15	22.48	9.42	85.83
		11.09	22.50	7.90	22.50	7.48	74.59
		13.06	29.21	8.91	29.21	9.62	77.30
		14.06	13.50	n. a.	n. a.	9.22	81.93
		n. a.	n. a.	n. a.	n. a.	n. a.	n. a.
	D	10.78	20.87	9.37	20.87	7.50	86.43
		11.72	23.77	11.62	23.77	9.92	86.18
		12.14	29.20	8.77	29.20	9.78	76.90
		12.57	16.20	10.75	16.20	9.45	86.52
		14.17	16.01	7.86	16.01	9.41	79.52

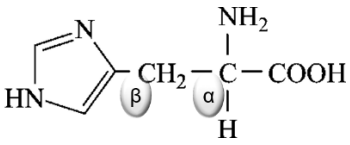

CONCLUSION

A large number of MHCs have been found in almost all major groups of *Bacteria* and *Archaea* (for a review see (235–238)). However, their complexity makes the characterization of these proteins very difficult from the structural and functional point of view. Several genetic and proteomic studies have proposed roles for some of them but their physiological functions and mode of action is still unclear. There is an inverse correlation between the number of heme groups of a MHC and the precise knowledge of their functional mechanisms. So far, detailed thermodynamic properties, and hence mechanistic information have only been obtained for MHCs that contain up to four heme groups (239,240). In order to shed light on the functional properties of large multiheme proteins new methodologies need to be developed. The linear and modular architecture displayed by the dodecaheme cytochrome GSU1996 was explored as a model in order to build a strategy for the detailed study of these proteins. This was the first time that such a methodology was used in the assignment of heme signals and it proved to be a promissory tool to gain functional insights on proteins with large molecular weight and number of hemes.

ASSIGNMENT SUPPLEMENTARY DATA

Table 3.S1 – Predicted ^{1}H chemical shifts (ppm) and ring current shifts (in parentheses) of the heme substituents of domains C and D in the reduced state. The chemical shifts and ring current shifts were calculated from the crystal structure of fragment CD (PDB file 3OUE) (221).

Heme substituent	Protein	Heme I	Heme III	Heme IV
5H	*Domain C*	9.45 (−0.09)	10.01 (−0.65)	9.39 (−0.03)
	Domain D	9.47 (−0.11)	9.99 (−0.63)	9.36 (0.00)
10H	*Domain C*	8.29 (1.07)	9.90 (−0.54)	9.59 (−0.23)
	Domain D	8.44 (0.93)	9.71 (−0.35)	9.72 (−0.36)
15H	*Domain C*	9.52 (−0.16)	9.81 (−0.45)	9.54 (−0.18)
	Domain D	9.50 (−0.14)	9.67 (−0.31)	9.49 (−0.13)
20H	*Domain C*	9.38 (−0.02)	9.85 (−0.49)	9.10 (0.26)
	Domain D	9.42 (−0.06)	9.94 (−0.58)	9.28 (0.08)
$2^{1}CH_3$	*Domain C*	3.44 (0.04)	4.34 (−0.86)	2.83 (0.66)
	Domain D	3.60 (−0.12)	4.55 (−1.07)	3.42 (0.06)
$7^{1}CH_3$	*Domain C*	3.44 (0.04)	3.97 (−0.49)	3.32 (0.16)
	Domain D	3.37 (0.11)	3.93 (−0.45)	3.34 (0.14)
$12^{1}CH_3$	*Domain C*	1.73 (1.75)	3.79 (−0.31)	2.81 (0.67)
	Domain D	1.47 (2.01)	3.84 (−0.36)	3.42 (0.06)
$18^{1}CH_3$	*Domain C*	3.51 (−0.03)	3.61 (−0.13)	3.42 (0.06)
	Domain D	3.44 (0.04)	3.78 (−0.30)	3.49 (−0.01)
$3^{1}H$	*Domain C*	6.19 (−0.06)	6.72 (−0.59)	6.14 (−0.01)
	Domain D	6.23 (−0.10)	6.67 (−0.54)	6.10 (0.03)
$8^{1}H$	*Domain C*	6.03 (0.10)	6.26 (−0.13)	6.40 (−0.27)
	Domain D	5.97 (0.16)	6.05 (0.08)	6.56 (−0.43)
$3^{2}CH_3$	*Domain C*	2.09 (0.03)	2.61 (−0.49)	2.03 (0.10)
	Domain D	2.17 (−0.05)	2.43 (−0.31)	2.08 (0.04)
$8^{2}CH_3$	*Domain C*	1.45 (0.67)	1.45 (0.67)	0.10 (2.02)
	Domain D	0.95 (1.17)	1.62 (0.50)	0.53 (1.59)

Table 3.S2 – Predicted ^{1}H chemical shifts (ppm) of the heme methyl substituents of domains C and D in the oxidized state. The chemical shifts were calculated from the crystal structure of fragment CD (PDB file 3OUE).

Heme methyl substituent	Protein	Heme I	Heme III	Heme IV
$2^{1}CH_3$	*Domain C*	24.16	20.00	28.61
	Domain D	24.73	18.74	27.47
$7^{1}CH_3$	*Domain C*	5.49	8.27	0.49
	Domain D	4.92	9.42	1.53
$12^{1}CH_3$	*Domain C*	24.16	20.00	28.61
	Domain D	24.73	18.74	27.47
$18^{1}CH_3$	*Domain C*	24.94	9.27	7.43
	Domain D	24.36	9.68	6.55

CHAPTER 4

THERMODYNAMIC AND KINETIC CHARACTERIZATION OF THE INDIVIDUAL DOMAINS C AND D AND OF THE TWO DOMAIN FRAGMENT CD FROM GSU1996

Contents

The results presented in this chapter were published in Fernandes AP, Alves MN, Salgueiro CA, Paquete CM. Unraveling the electron transfer processes of a nanowire protein from *Geobacter sulfurreducens*. Biochim Biophys Acta. 2016;1857(1):7–13. Available from: http://dx.doi.org/10.1016/j.bbabio.2015.09.

ABSTRACT

The extracellular electron transfer metabolism of *G. sulfurreducens* is sustained by several MHCs. One of these is the dodecaheme cytochrome GSU1996 that belongs to a new sub-class of *c*-type cytochromes. It was proposed that this protein works as an electrically conductive device in *G. sulfurreducens*, transferring electrons within the periplasm or to outer-membrane cytochromes. Here, a novel strategy was applied to characterize in detail the thermodynamic and kinetic properties of the hexaheme fragment CD of GSU1996. This characterization revealed the electron transfer process of GSU1996 for the first time and showed that a heme at the edge of the C-terminal of the protein is thermodynamic and kinetically competent to receive electrons from physiological redox partners. This information contributes towards understanding how this new sub-class of cytochromes functions as nanowires, and also increases the current knowledge of the extracellular electron transfer mechanisms in *G. sulfurreducens*.

INTRODUCTION

The *c*-type cytochromes are among the most diverse classes of metal containing proteins, fulfilling various functions in numerous biological electron transfer processes (241). The heme groups are covalently linked to the polypeptide chain through thioether bonds set by the cysteine residues in the heme-binding motif Cys-X-X-Cys-His. In this motif, the histidine is usually one of the axial ligands to the heme iron and X can be any amino acid residue. Interestingly, the covalent attachment to the polypeptide chain allows *c*-type cytochromes to bind numerous hemes on a short stretch of protein, where the heme-protein ratio is high and only very little secondary structure can be observed. In DMRB, multiheme *c*-type cytochromes are implicated in several processes, such as electron transfer in respiratory processes (135,242), gene regulation (109) and as electron-storage sinks or capacitors (117,243).

GSU1996 was proposed to work as a putative natural nanowire transferring electrons within the periplasmic space of *G. sulfurreducens* (195). It was also proposed that in the absence of electron acceptors, these proteins contribute to the enhancement of the cellular electron-storage capacity. In this process, they may receive electrons from the inner-membrane and contribute to prevent metabolic arrest (117).

In order to understand the function of this cytochrome it is necessary to elucidate its electron transfer mechanism. This information is only possible with a detailed characterization of the thermodynamic and kinetic properties of the various redox centers (244). While the thermodynamic data allow identification of the possible electron transfer pathways, the kinetic properties elucidate the velocity of a particular electron transfer event and define the electron transfer steps that occur in the protein. Over the years, methodologies that discriminate the individual redox properties of multiple centers and their pairwise interactions were developed (244). These methods are of general application and independent of any structural organization of the proteins.

Here, the thermodynamic and kinetic properties of the fragment CD of GSU1996 were determined and used to elucidate the electron transfer processes performed by the C-terminal half of the protein. This extends the experimental application of methods that define microscopic properties of multicenter redox proteins to a case of six redox centers. It was shown that the most exposed heme of domain D, at one edge of the protein, is the most thermodynamic and kinetically competent to receive electrons from the redox electron donor, and allows the protein to work as a nanowire device. This information is pioneer and contributes significantly to the understanding of the mechanisms of long range electron transfer in nanowire cytochromes.

MATERIALS AND METHODS

Protein purification

The GSU1996 domains C and D, as well as the fragment CD, were expressed and purified as previously described (192,196) with minor changes. Briefly, the proteins were produced in *E. coli* strains

JCB7123 (domain C) (222) and JM109 (domain D and fragment CD) harboring plasmid pEC86, which contains the *c*-type cytochromes maturation gene cluster *ccmABCDEFGH* (161).

The overexpressed proteins were purified as follows: the periplasmic fractions were isolated by osmotic shock in the presence of lysozyme (Sigma-Aldrich) and dialyzed against 10 mM Tris-HCl buffer pH 7.0 (domains C and D) or 20 mM NaPi buffer pH 5.9 (fragment CD). Subsequently, the samples were subjected to two chromatographic steps. In the first step, samples were separately loaded onto cation-exchange columns (Econo-Pac High S, Bio-Rad) and eluted with a linear gradient of NaCl. In the second step, the fractions containing the proteins of interest were pooled, concentrated and loaded onto a HiLoad 16/60 Superdex 75 column (GE Healthcare), equilibrated with 20 mM NaPi buffer pH 8.0 containing 100 mM NaCl. Both chromatographic steps were performed in an ÄKTA Prime Plus FPLC System (GE, Amersham). The presence of the purified proteins was confirmed by 12% SDS-PAGE with both heme (245) and Coomassie blue staining. Protein concentrations were determined by UV-visible spectroscopy with the specific absorption coefficient of the α-band at 552 nm determined for the cytochrome c_7 PpcA ($\Delta\varepsilon_{552\ nm}$ = 32.5 mM^{-1} cm^{-1} per heme) (197).

NMR experiments

The buffer of the purified proteins was exchanged for 80 mM NaPi buffer pH 8.0 with NaCl (final ionic strength of 250 mM) prepared in 99.9% ^2H_2O (CIL), through ultrafiltration procedures with Amicon Ultra Centrifugal Filter Units (Millipore). Protein samples with approximately 1.5 mM were placed in 3 mm Wilmad NMR tubes. The 1D ^{1}H-NMR spectra were acquired on a Bruker Avance 600 MHz spectrometer with a spectral width of 30 kHz at 289 K. ^{1}H chemical shifts were calibrated using the water signal as internal reference. All NMR spectra were processed using TopSpin™ NMR Software from Bruker Biospin.

Redox titrations followed by visible spectroscopy

Redox titrations of domain D and fragment CD followed by UV-visible spectroscopy were performed at 289 K in anaerobic conditions as described previously in the literature (197). Protein solutions were prepared in 80 mM NaPi buffer (at pH 7 and 8) with NaCl (final ionic strength of 250 mM) inside an anaerobic glove box (MBraun), kept at below 2 ppm oxygen. The redox potential values of the proteins' solution were measured with an Ag/AgCl combined electrode, calibrated at the beginning of each titration with saturated solutions of quinhydrone freshly prepared at pH 7 and 8 and the calibration was reassessed at the end of the respective titration. To ensure equilibrium between the electrode and the redox centers of the protein, a mixture of redox mediators was used: indigo tetrasulfonate ($E^{\circ\prime} = -30$ mV), indigo trisulfonate ($E^{\circ\prime} = -70$ mV), indigo disulfonate ($E^{\circ\prime} = -110$ mV), riboflavin ($E^{\circ\prime} = -208$ mV), anthraquinone 2-sulfonate ($E^{\circ\prime} = -225$ mV), safranin ($E^{\circ\prime} = -280$ mV), benzyl viologen ($E^{\circ\prime} = -345$ mV), neutral red ($E^{\circ\prime} = -325$ mV), and methyl viologen ($E^{\circ\prime} = -440$ mV). For redox titrations performed at pH 7, the mediator 2-hydroxy 1,4-naphthoquinone ($E^{\circ\prime} = -152$ mV) was added to the redox mediators mixture, while for redox titrations performed at pH 8 the mediators methylene blue ($E^{\circ\prime} = +11$ mV) and gallocyanine ($E^{\circ\prime} = +21$ mV) were added to the redox mediators mixture. Different

concentration ratios of protein (approximately 10 μM) to mediators (between 1 and 2 μM) were tested to check for possible interactions between the protein and redox mediators. To check for hysteresis and reproducibility, the redox titrations were repeated at least twice in the oxidative and reductive directions for each pH with sodium dithionite and potassium ferricyanide as reducing and oxidizing agents, respectively. Each titration consisted in the addition of an aliquot of 1 to 2 μL of a sodium dithionite (25 mM or, when approaching the equivalence point, 12.5 mM) or potassium ferricyanide (17.4 mM or, when approaching the equivalence point, 8.7 mM). Between additions, the protein solutions were allowed to rest and the respective potential was then measured and a visible spectrum acquired between 300 and 800 nm. The reduced fraction of the cytochromes was determined by calculation of the area of the α peak with the absorbance data obtained at 552 nm and the isosbestic points of the target proteins. This analysis allows the subtraction of the optical contribution from the redox mediators.

Reduction kinetic experiments with sodium dithionite

Kinetic data were obtained by measuring the light absorption changes at 552 nm with a stopped-flow instrument (SHU-61VX2 from TgK Scientific) placed inside the anaerobic chamber. The temperature of the kinetic experiments was kept at 289 ± 1 K using an external circulating bath.

The reduction experiments were performed by mixing the target proteins with sodium dithionite. The target proteins were prepared in degassed 80 mM NaPi buffer (pH 7 and 8) with NaCl (final ionic strength of 250 mM). In order to guarantee pseudo-first order conditions (see below), this strong reducing agent was used in large excess (246). Solid dithionite was added to degassed 5 mM NaPi buffer pH 8 with NaCl (final ionic strength of 250 mM). The concentration of the reducing agent was determined in each experiment using $\varepsilon_{314\,nm}$ of 8000 M^{-1} cm^{-1} (247). Partially reduced protein was prepared by adding small amounts of concentrated solution of sodium dithionite to achieve the desired degree of reduction, before the beginning of the kinetic experiment. The reference value for the absorbance of the fully oxidized state of the protein was obtained at 552 nm in the beginning of the experiment by mixing the oxidized protein with degassed buffer, while the reference value for the fully reduced state of the protein was obtained from the final absorbance taken at effectively infinite time.

Although the models by Catarino and Turner (203) and its resulting deductions are valid for reversible reactions, for calculations purposes solely, one-directional reactions are necessary and usually a strong electron donor is used, as the case of sodium dithionite. Albeit its complex equilibrium chemistry, when $SO_2^{\bullet}$ radical is the reducing agent (248) the midpoint redox potential of the couple $SO_2/SO_2^{\bullet}$ (−0.3 V) is the relevant value for calculations and it has no dependence on dithionite concentration or pH above 2 (249). For the three proteins, the reducing agent was found to be the one electron donor bisulfite radical ($SO_2^{\bullet}$) (248). The pH of the samples was measured after each kinetic experiment and was taken as the pH of the kinetic experiment.

Data analysis

Thermodynamic analysis

The model used in the analysis was adapted from the thermodynamic model previously developed (see Thermodynamic analysis in Thermodynamic and Kinetic Characterization Supplementary Data) (200,244). For a protein with six hemes and one protonatable center, such as for the fragment CD, 64 microstates are necessary to describe in detail all possible redox transitions (Figure 4.1).

The microscopic thermodynamic parameters of this protein include six reduction potentials, one for each heme, the *pKa* of the ionizable center, fifteen redox interaction energies between the heme groups, and six redox-Bohr interaction energies between the hemes and the ionizable center (244). The thermodynamic model considers that the redox interactions between each pair of hemes are only due to Coulombic effects, and that no conformation modification occurs with reduction or oxidation of the protein.

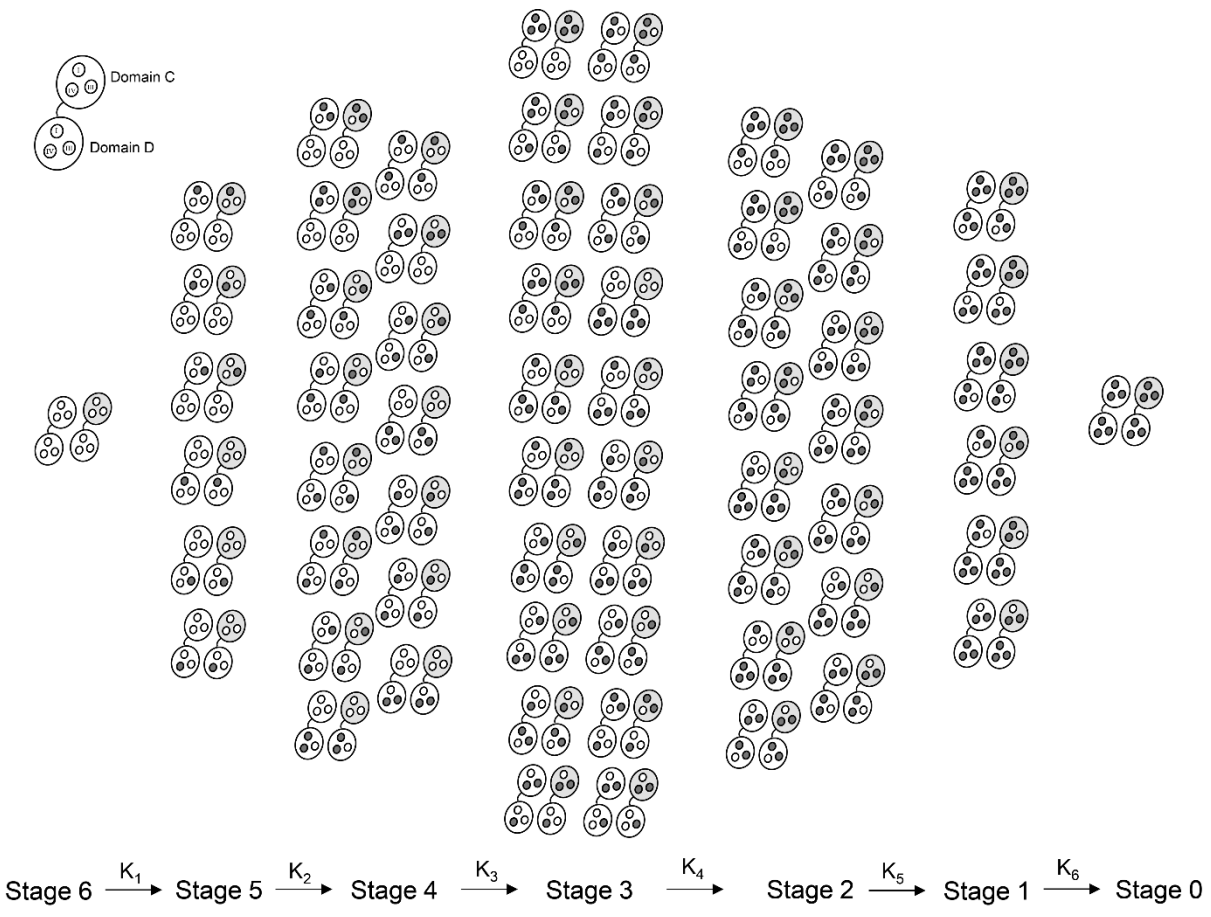

Figure 4.1 – Schematic representation of the microstates of fragment CD from GSU1996, a protein with six hemes and one acid-base center. The protein is represented as large circles, with black and white dots representing the hemes in the reduced and oxidized state, respectively. White and gray protein represents the deprotonated and protonated microstates for the acid-base center associated with the hemes. The redox stages are numbered according to the number of oxidized hemes and organized in columns that group populations with the same oxidation state. Macroscopic electron transfer steps between stages are shown in the direction of reduction, and macroscopic rate constants are represented by K_{1-6}.

In electrostatic interactions that do not occur in a vacuum environment, shielding of the interactions take place. These are influenced by the medium composition and, consequently, by its polarization extent. Therefore, the application of a dielectric constant higher than the one used in vacuum medium prevents the listing of all the factors implicated (250). Additional shielding may arise in ionic solutions, as a result of the heterogeneous charge distribution. This alters the interactions distance dependent decay that seems to reflect a stronger shielding effect with distance than predicted from the dielectric constant of the medium. Under such conditions, the interaction (V_i) amid two particles with unitary charge may be determined by:

$$V_i = k\frac{1}{\varepsilon r}\exp\left(\frac{-r}{r_D}\right) \qquad \textbf{Equation 4.1}$$

In this model, homogeneous polarizability of the medium is considered and Debye-Hückel shielding is applied to account for the for the effect of counterions (250,251). In Equation 4.1, $k = \frac{q_e}{4\pi\varepsilon_0}$, where q_e is the electron charge and ε_0 is the vacuum electric permittivity. The Debye length, r_D, depends on the charge density, temperature and ionic strength. The distance between the charged centers is represented by r. Fitting of experimental data is achieved by adjustment of the parameters r_D and ε.

The redox interaction energies for domain D were calculated using the Debye-Hückel model of shielded electrostatic interactions (Equation 4.1), that considers an effective dielectric constant of 8.6, a Debye length of 7.7 Å (219,250), and the iron-iron distances measured in the 3D-structure of fragment CD (pdb: 3OUE).

The microscopic thermodynamic parameters of domain C that include four reduction potentials, one for each individual heme, the redox interactions between pairs of hemes, the *pKa* of the ionizable center, and the redox-Bohr interaction energies (197) were used to predict the thermodynamic properties of domain D and fragment CD. Since domain D does not present redox-Bohr effect in the pH range studied (see Results and Discussion) no redox-Bohr interactions were considered.

The simultaneous fit of four independent redox titrations obtained at pH 7 and 8 for domain D and for fragment CD to the thermodynamic model, using the microscopic thermodynamic properties published for domain C and the redox interaction energies calculated for domain D, enabled the determination of three reduction potentials, one for each heme in domain D. The thermodynamic model was implemented in Microsoft Excel® and the Generalized Reduced Gradient resolution method of the add-in program Solver was used for the fitting. This model considers that each heme contributes equally to the change of absorbance at 552 nm.

The standard errors associated with the microscopic reduction potentials determined for the hemes of domain D were estimated from the covariance matrix using an experimental uncertainty of 3% of the total optical signal of the UV-visible redox titrations.

Kinetic analysis

Kinetic data obtained for the reduction of domains C and D, and of fragment CD with sodium dithionite at different pH values were normalized in order to have oxidized fractions versus time. The timescale was corrected to account for the dead time of the apparatus. To reduce electrical noise, a

minimum of two data sets were averaged for each experimental condition. The experimental data obtained for the reduction of each protein with sodium dithionite at various pH values were fitted simultaneously using the kinetic model described in the literature (203,244) adapted for six redox centers. The application of this model requires fast intramolecular electron transfer and slow intermolecular electron exchange. These conditions, usually given by the short distance between the hemes, ensure that a thermodynamic reequilibration occurs within the protein between each sequential electron transfer step. Furthermore, the fast equilibrium within microstates belonging to the same stage of oxidation (within each column in Figure 4.1) and the use of large excess of reducing agent simplifies the kinetic analysis (203). In this situation each electron transfer step is characterized by a macroscopic rate constant (K_{1-6} in Figure 4.1 for fragment CD) that is parsed into the contribution of all the microscopic rate constants of the transition that participate in that step (k_i^j, where i is the center that is under reduction, and j the other center(s) already reduced).

Each contribution is weighted according to the thermodynamic equilibrium populations of the starting states, which are known from the thermodynamic properties of the protein (203).

In this model, Marcus theory for electron transfer (252) is used to separate the contribution of the driving force of the reaction from the reference rate constant (k_i^0) that is intrinsic to each heme (203):

$$k_i^j = k_i^0 exp\left[\frac{e_i F}{2RT}\left(1 + \frac{e_D F}{\lambda} - \frac{e_i F}{2\lambda}\right)\right] \qquad \textbf{Equation 4.2}$$

In Equation 4.2, e_i is the reduction potential of the transition between a particular pair of microstates and e_D is the reduction potential of the electron donor. The reference rate constants obtained with this model are intrinsic to each heme and enable the definition of the role of each heme in the overall reduction process of the protein (203).

The fitting of the experimental data was achieved using the Nelder-Mead algorithm with the kinetic model implemented in MATLAB® (253,254). Fittings using different initial values for the reference rate constants were performed to find the best solution. An experimental uncertainty of 5% of the total amplitude of the optical signal of the kinetic trace was used to determine the standard errors associated with each reference rate constant.

RESULTS AND DISCUSSION

Typically, MHCs contain several hemes that are closely-packed to allow efficient electron transfer within the proteins (135,255). In the dodecaheme protein GSU1996 from *G. sulfurreducens* the hemes are arranged in a novel “nanowire” architecture, where the hemes are at close distance to each other and have substantial surface exposure (195). Consequently, multiple centers may donate or receive electrons from the redox partners. Thus, the identification of the redox centers that contribute significantly to the intermolecular electron transfer with the redox partners is a priority to understand the functional mechanism of GSU1996. This is however only possible with the characterization of the thermodynamic and kinetic properties of the individual redox centers in the protein.

Thermodynamic characterization of domain D and fragment CD from *G. sulfurreducens*

NMR can provide the spectroscopic distinction of the various hemes in a way that is highly sensitive to their redox state (212). Indeed, in conditions of slow intermolecular and fast intramolecular electron exchange rates on the NMR timescale, it is possible to follow NMR signals from a particular heme methyl through the oxidation stages of the protein, providing the necessary data to establish the oxidation order of the redox centers (213,219). This approach was previously used to characterize in detail the thermodynamic properties of domain C of GSU1996 (197). The application of this methodology depends on the complexity of the system that is given by the size of the molecule, number of hemes and if the convenient electron exchange conditions are met. In the case of domain C, the decrease of temperature and increase of ionic strength were essential to achieve the slow intermolecular electron exchange regime necessary to follow the NMR signals through the different oxidation stages (197). Unfortunately, for domain D the slow intermolecular exchange regime on the NMR time scale was not achieved in the same experimental conditions, even collecting data at a proton Larmor frequency of 800 MHz, precluding the determination of the detailed thermodynamic properties of this domain with this methodology. The complexity of the NMR spectra of the hexaheme domains of GSU1996 and of the GSU1996 itself prevents the discrimination of the NMR signals from each heme in each oxidation stage (244).

The 1D ^{1}H-NMR spectra of domains C, D and of fragment CD exhibit the typical features of low-spin *c*-type cytochromes with signals from the heme methyl groups shifted to the low-field region between 10 and 40 ppm (Figure 4.2). The dispersion of these signals is highly dependent on the relative orientation between neighboring hemes and on the relative orientation of the axial ligands (233).

Interestingly, the 1D ^{1}H-NMR spectrum of fragment CD is similar to the sum of the spectra of the individual domains, suggesting that the arrangement of the hemes and the axial ligand geometries in fragment CD are conserved.

For this reason, the thermodynamic model used to characterize the properties of fragment CD considers that the redox properties of the hemes and the heme interactions among pairs of hemes are conserved in fragment CD as in the individual domains C and D. In this model the redox properties of domain C previously reported were used (197), whereas the heme interaction energies of domain D were predicted from the heme iron-iron distances (Table 4.1).

Redox titrations followed by UV-visible spectroscopy of domains C and D performed at pH 7 and 8 show that both proteins do not present redox-Bohr effect within the pH range (Figure 4.3). Indeed, published data for domain C showed that the *pKa* of the redox-linked ionizable center is lower than 6 (197). For these reasons, the microscopic thermodynamic model only considers one ionizable center that is associated with domain C (Figure 4.1).

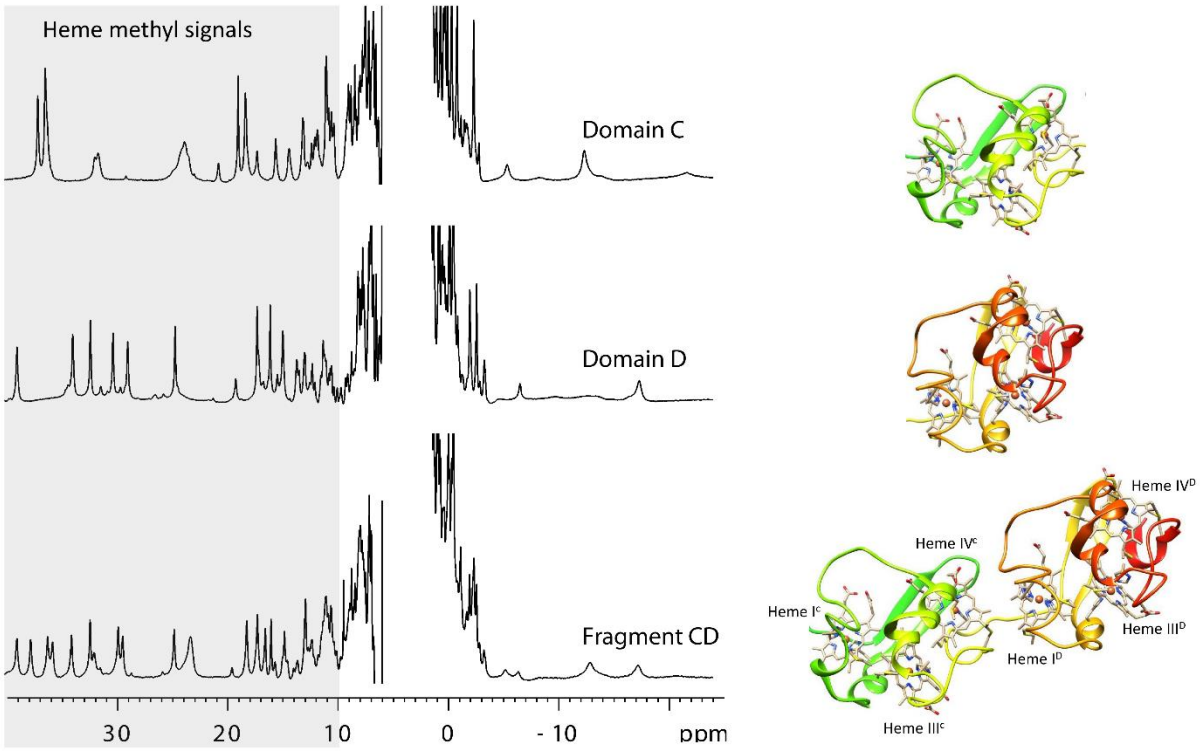

Figure 4.2 – NMR fingerprint of fragment CD and its domains. (A) 1D ^{1}H-NMR spectra of domains C, D and of fragment CD from *G. sulfurreducens* at 289 K and pH 8. The NMR spectral region where heme methyl groups of low-spin *c*-type cytochromes appear are highlighted by a gray box. (B) Three-dimensional structures of domain C, domain D and fragment CD. The 3D structures of domains C and D were taken from the 3D structure of the fragment CD (pdb: 3OUE). The hemes are numbered by analogy to the structurally homologous hemes in tetraheme cytochromes c_3.

The fitting of the redox titrations of domain D and of fragment CD to the thermodynamic model provides the reduction potential of the three hemes of domain D. Together with the published data for domain C and the calculated pairwise interactions between the hemes, the information is sufficient to achieve the detailed thermodynamic characterization of fragment CD (Table 4.2). Clearly, the model captures well the trend of the data and indicate that the redox behavior of the hemes in domains C and D are the same as in fragment CD (Figure 4.3).

Table 4.1 – Heme redox interaction energies of domain D in fragment CD from GSU1996. These values were determined from the Debye-Hückel model of shielded electrostatic interactions (see Materials and Methods).

	Heme pairs	Distance (Å)	Interaction energies (meV)
Fragment CD	I^{D}-III^{D}	11.3	34
	I^{D}-IV^{D}	18.0	9
	III^{D}-IV^{D}	12.1	29
	I^{C}-I^{D}	30.7	1
	I^{C}-III^{D}	40.6	0
	I^{C}-IV^{D}	48.3	0
	III^{C}-I^{D}	21.8	5
	III^{C}-III^{D}	30.4	1
	III^{C}-IV^{D}	39.5	0
	IV^{C}-I^{D}	14.7	17
	IV^{C}-III^{D}	25.3	3
	IV^{C}-IV^{D}	32.3	1

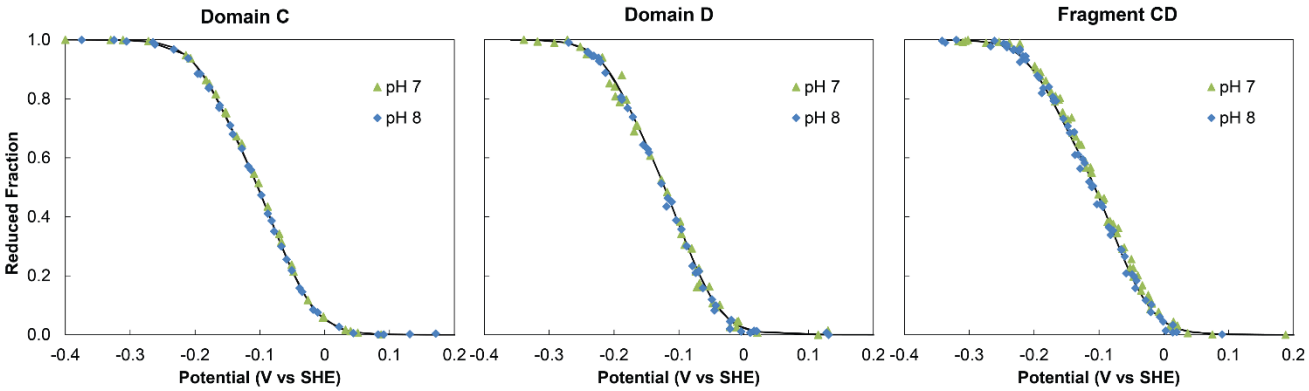

Figure 4.3 – Redox titrations followed by visible spectroscopy of domain C, domain D and fragment CD at pH 7 and 8 (289 K). Redox titrations of domain C were previously performed (197), whereas redox titrations of domain D and of fragment CD were performed in this work. The solid lines represent the best fit of the experimental data with the thermodynamic model described in Materials and Method section and give rise to the thermodynamic parameters reported in Table 4.2.

The thermodynamic parameters of fragment CD from GSU1996 show that the reduction order of the hemes are I^C, IV^D, IV^C, I^D, III^C and III^D (Figure 4.4).

Interestingly, in fragment CD the heme III of both domains C and D is the last one to be reduced. In the characterization of the individual domain C, heme III was shown to be the last one to be reduced (197), as it was observed for domain D. This constitutes further evidences that the redox behavior of the individual domains is maintained in the hexaheme fragment.

Table 4.2 – Microscopic thermodynamic parameters determined for fragment CD from GSU1996 in the fully reduced and protonated protein.

Hemes	Energies (meV)						
	I^C	III^C	IV^C	I^D	III^D	IV^D	Protonatable center
I^C	**−106**	*44*	7	*1*	*0*	*0*	−4
III^C		**−136**	40	*5*	*1*	*0*	−25
IV^C			**−125**	*17*	*3*	*1*	−13
I^D				**−155 (7)**	*34*	*9*	-
III^D					**−178 (5)**	*29*	-
IV^D						**−113 (4)**	-
Protonatable center							**340**

Diagonal terms (in bold) represent the oxidation energies of the six hemes and the deprotonation energy for the protonatable center in the fully reduced and protonated protein. The off-diagonal elements represent the redox and redox-Bohr interaction energies between the seven centers (italic elements are the heme redox interaction energies of domain D in fragment CD presented in this table). The thermodynamic properties of domain D are shown in a gray box, which includes the oxidation energies of the three hemes (in bold), and the redox interaction energies between the three centers. Standard thermodynamic expressions relate the oxidation energies and deprotonation energy with reduction potentials and pKa, respectively. Standard errors for the three parameters extracted from fitting the model to the experimental data are indicated within brackets and were calculated from the diagonal element of the covariance matrix, considering an experimental uncertainty of 3%.

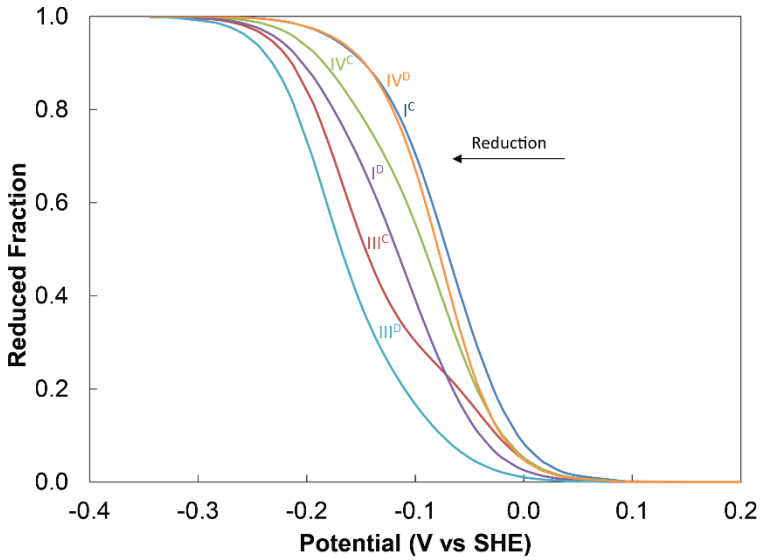

Figure 4.4 – Reduced fraction of the individual hemes in fragment CD from GSU1996 calculated at pH 7 with the thermodynamic parameters presented in Table 4.2.

Kinetic characterization of fragment CD

The kinetic traces obtained for the reduction of fragment CD from GSU1996 with sodium dithionite do not show pH dependence in the pH 7–8 range (Figure 4.5). This is in agreement with the data obtained from the redox titrations monitored by UV-visible spectroscopy for fragment CD (Figure 4.3).

Reductive kinetic traces were obtained with the protein poised at different levels of reduction. This way, the different kinetic experiments start from equilibrium between the different stages of oxidation in a condition that depends solely on the thermodynamic properties of the hemes (246).

The kinetic model uses the thermodynamic parameters to discriminate the rate constants for the reduction of the individual hemes (203).

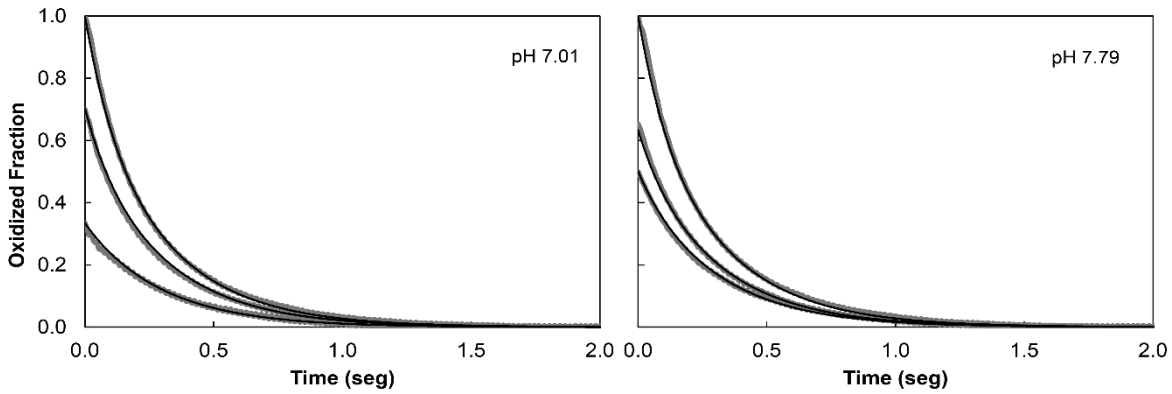

Figure 4.5 – Kinetics of reduction of fragment CD from GSU1996 by sodium dithionite at different pH values. Gray lines are the kinetic data obtained for the fully oxidized state of the protein, for 70% and 34% oxidized fraction at pH 7.01, and for 65% and 50% oxidized fraction at pH 7.79. Black lines are the fit of the kinetic model to the data. The concentration of sodium dithionite used in the kinetic experiments was 115 µM (after mixing), while the concentration of fragment CD was 0.91 and 0.90 µM (after mixing) at pH 7.01 and 7.79, respectively.

Table 4.3 – Reference rate constants for each heme in the reduction process with sodium dithionite (k_i^0) for fragment CD from GSU1996 at 289 K. Standard errors were calculated from the diagonal element of the covariance matrix considering an experimental uncertainty of 5% of the total amplitude of the optical signal in the kinetic traces are given in parentheses.

		$\boldsymbol{k_i^0}(\times 10^6 \mathrm{s}^{-1}\mathrm{M}^{-1})$
Domain C	Heme I	0.0 (5.7)
	Heme III	0.0 (2.4)
	Heme IV	0.0 (5.2)
Domain D	Heme I	74.0 (2.2)
	Heme III	274.3 (1.2)
	Heme IV	0.0 (2.1)

Table 4.3 presents the reference rate constants for each heme obtained by the best fit of the kinetic model to the experimental data acquired at different pH values for fragment CD. These reference rate constants are intrinsic to each heme and allow defining the contribution of each heme in the reductive process of the protein.

Only hemes from domain D, in particular hemes I and III, contribute to the entrance of electrons in the fragment CD from GSU1996 (Table 4.4).

Interestingly, heme III, the heme that contributes more to the reduction of fragment CD (Table 4.4) is the most exposed heme of domain D (195) and it is the heme with the lowest reduction potential in fragment CD. Clearly, the exposure of the hemes is not the most important factor contributing for the reductive kinetic process of the protein since heme I from domain C is the most exposed heme at fragment CD (195), and does not contribute to the reduction process of the hexaheme protein.

The entrance of electrons through heme III from domain D clearly shows how GSU1996 works as a nanowire protein. Heme III from domain D, at one extreme of GSU1996, can receive electrons from the physiological electron donor and transfer them to the other hemes within the protein. Since, at least in fragment CD, this heme has the lowest reduction potential, it is spontaneously re-oxidized by the other hemes in the fragment and remains free to receive electrons from redox partners, allowing the protein to function as a nanowire device (Figure 4.6).

CONCLUSION

Nanowire cytochromes are a new class of proteins found in the genome of several *Geobacter* species proposed to be responsible for long-range electron transfer.

Table 4.4 – Fraction of electrons that enter fragment CD from GSU1996 by each heme, calculated at pH 7 with the thermodynamic parameters from Table 4.2 and the reference rate constants presented in Table 4.3.

Stages	**Hemes**					
	I^C	III^C	IV^C	I^D	III^D	IV^D
Fraction of electrons	0.00	0.00	0.00	1.36	4.64	0.00

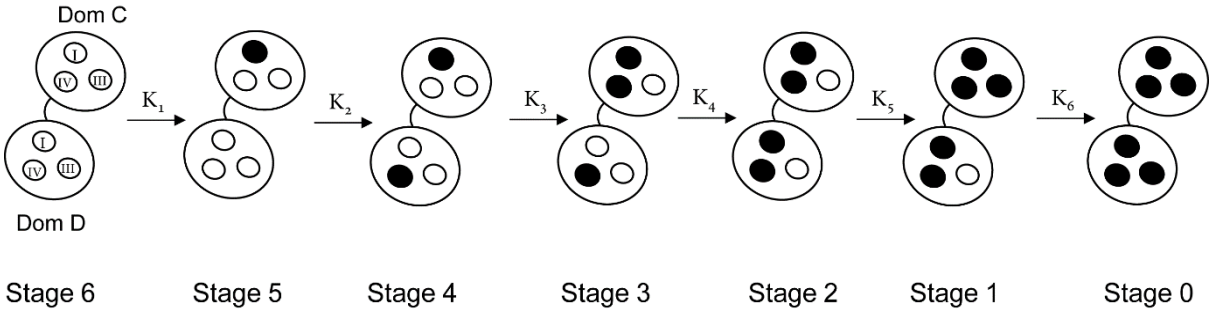

Figure 4.6 – Schematic representation of the most important microstates for the reduction of fragment CD from GSU1996. Black and white dots representing the hemes in the reduced and oxidized state, respectively.

The elucidation of the detailed thermodynamic and kinetic properties of the C-terminal half of the protein GSU1996 from *G. sulfurreducens* opens the possibility to unravel the electron transfer processes performed by this new class of proteins.

Indeed, the entrance of electrons through the heme that is at one edge ensures that the electrons may flow within the protein to the other end, allowing it to work as a nanowire. Further studies will enable the characterization of the full length protein and the elucidation of the electron transfer processes during its oxidation. This information will also be of significant importance to increase our knowledge on the extracellular electron transfer processes performed by *G. sulfurreducens*, a key asset to improve its biotechnological applications, such as microbial fuel cells.

THERMODYNAMIC AND KINETIC CHARACTERIZATION SUPPLEMENTARY DATA

Thermodynamic analysis

The reduced fractions of domain D and fragment CD were determined with the α peak (552 nm) according to the methodology previously described (240,246). Briefly, the reduced fractions were determined by integration of the area from the α peak located between the respective isosbestic points. The optical contribution of the redox mediators was subtracted by the measurement of the α peak relative to the flat line that connects the isosbestic points. Experimental potential data were corrected in agreement with the electrode calibration performed at 289 K and the potential value for the Ag/AgCl electrode relative to the standard hydrogen electrode (214 mV).

The determination of the reduced fractions of domain D is explained next as a working model. As earlier described, the different microstates in a triheme cytochrome may be grouped in four macroscopic oxidation stages ($S_{0\text{-}3}$), connected by three one-electron redox steps that contain the microstates with the same number of oxidized heme groups. Each microstate pair (protonated/deprotonated) is connected by one-electron redox step that may be described by a total of 24 Nernst equations identical to:

$$E = E^{\circ} + \frac{RT}{F} ln \frac{ox}{red} \qquad \textbf{Equation 4.S1}$$

In each case, three Nernst equations connect the microstates in the oxidation stage 1 and the microstates in the oxidation stage 0; six equations connect the microstates in the oxidation stage 2 and the microstates in the oxidation stage 1 and, finally, three Nernst equations connect the microstates in the oxidation stage 3 and the oxidation stage 2. For instance, departing from the completely reduced microstate and following the sequential oxidation of the heme groups I, III and IV (represented by 1, 3 and 4, respectively) along the four oxidation stages:

$$P_0 \underset{E_1^{\circ}}{\overset{1e^-}{\rightleftharpoons}} P_1 \underset{E_3^{\circ}}{\overset{1e^-}{\rightleftharpoons}} P_{13} \underset{E_4^{\circ}}{\overset{1e^-}{\rightleftharpoons}} P_{134}$$

the three relevant Nernst equations, expressed as a function of P_0, are:

$$E = E_1^{\circ} + \frac{RT}{F} ln \frac{P_1}{P_0} \Leftrightarrow P_1 = P_0 e^{(E - E_1^{\circ})\frac{F}{RT}} \qquad \textbf{Equation 4.S2}$$

$$E = E_3^{\circ} + \frac{RT}{F} ln \frac{P_{13}}{P_1} \Leftrightarrow P_{13} = P_0 e^{(2E - E_1^{\circ} - E_3^{\circ})\frac{F}{RT}} \qquad \textbf{Equation 4.S3}$$

$$E = E_4^{\circ} + \frac{RT}{F} ln \frac{P_{134}}{P_{13}} \Leftrightarrow P_{134} = P_0 e^{(3E - E_1^{\circ} - E_3^{\circ} - E_4^{\circ})\frac{F}{RT}} \qquad \textbf{Equation 4.S4}$$

where E, E_1^o, E_3^o and E_4^o represent, respectively, the experimental measured potential and the standard potential between each oxidation stage; F represents the Faraday constant; T, the temperature and R, the ideal gas constant.

The reduced fraction is determined by the relation between the reduced species and the total of reduced and oxidized species. Therefore, accounting for the electrons present in the several microstates, the reduced fraction may be written as following:

$$f_{reduced} = \frac{3P_0 + 2P_1 + P_{13} + 0P_{134}}{3P_0 + 2P_1 + P_{13} + 0P_{134} + 0P_0 + P_1 + 2P_{13} + 3P_{134}}$$

$$\Leftrightarrow$$

$$f_{reduced} = \frac{3P_0 + 2P_1 + P_{13}}{3(P_0 + P_1 + P_{13} + P_{134})}$$

This can be written as a function of the different potentials, by replacement of P_1, P_{13} e P_{134} by the three Nernst equations (Equation 4.S2; Equation 4.S3 and Equation 4.S4) above described:

$$f_{reduced} = \frac{3+2e^{\left[\left(E-E_1^\circ\right)\frac{F}{RT}\right]}+e^{\left[\left(2E-E_1^\circ-E_3^\circ\right)\frac{F}{RT}\right]}}{3\left(1+e^{\left[\left(E-E_1^\circ\right)\frac{F}{RT}\right]}+e^{\left[\left(2E-E_1^\circ-E_3^\circ\right)\frac{F}{RT}\right]}+e^{\left[\left(3E-E_1^\circ-E_3^\circ-E_4^\circ\right)\frac{F}{RT}\right]}\right)} \quad \textbf{Equation 4.S5}$$

The standard reduction potentials ($E°$) were calculated by fitting the experimental data to Equation 4.S5, with the *Solver* tool of Microsoft Excel (Microsoft. Microsoft Excel. Redmond, Washington: Microsoft, 2010. Computer Software) and considering $F = 96500\, C.mol^{-1}$, $R = 8.314\, J.K^{-1}.mol^{-1}$ and $T = 289\, K$.

The respective energy values can be related with the reduction potentials by:

$$\Delta G = -nF\Delta E \quad \textbf{Equation 4.S6}$$

Relative to the fully reduced and protonated reference microstate, each microstate energy value arises as a sum of the suitable energy terms depicted from the four redox centers, the six two-center interactions, the solution potential in a particular oxidation stage and the proton chemical potential (in the case of the deprotonated form):

$$G_i = G_{iH} + g_H + \sum g_{iH} - 2.3RTpH \quad \textbf{Equation 4.S7}$$

$$G_{iH} = \sum g_i + \sum g_{ij} - SFE \quad \textbf{Equation 4.S8}$$

In Equation 4.S7 and Equation 4.S8, i stands for the particular microstate that can be in the deprotonated or protonated (H) forms; g_i represents the heme oxidation energy; g_{ij} the interaction energy between pairs of hemes; g_H the deprotonation energy of the fully reduced protein and g_{iH} the interaction energy between the hemes and the redox-Bohr center.

Finally, the pKa values of the fully reduced and oxidized states of the triheme domain are determined by:

$$pKa\ (fully\ reduced) = \frac{g_H \mathrm{F}}{2.3RT}$$ **Equation 4.S9**

$$pKa\ (oxidation\ stage\ 1-3) = \frac{(g_H + \sum_{i=1}^{3} g_{iH})F}{2.3RT}$$ **Equation 4.S10**

CHAPTER 5

INTERACTION STUDIES BETWEEN GSU1996 AND THE PPC'S FAMILY

Contents

Part of the results presented in this chapter were published in Fernandes AP, Nunes TC, Paquete CM, Salgueiro CA. Interaction studies between periplasmic cytochromes provide insights into extracellular electron transfer pathways of *Geobacter sulfurreducens*. Biochem J. 2017;474(5): 797–808. DOI: 10.1042/BCJ20161022.

ABSTRACT

Nanowire cytochromes that contain at least 12 heme groups, have been proposed to play a role in electron storage in conditions of environmental lack of electron acceptors. Up to date, no redox partners have been identified in *G. sulfurreducens* and concomitantly the extracellular electron transfer and electron storage mechanisms remain unclear. Complexes of redox proteins show weak affinity and diminished lifetime, which makes them difficult to identify. Nuclear magnetic resonance spectroscopy techniques have already proved to be a powerful tool to probe for such partners, as it leads to the identification not only of interacting partners and determination of its associated parameters, but also of specific docking sites and structural modifications upon formation of these transient complexes. In the present work, potential redox partners were probed by interaction studies performed by NMR techniques. NMR chemical shift perturbation measurements of the heme methyl signals of GSU1996 and PpcA showed that the proteins form a transient redox complex in an interface that involves heme groups from two different domains located at the C-terminal of GSU1996. Overall, this study provides for the first time a clear evidence for an interaction between periplasmic cytochromes that might be relevant for the extracellular electron transfer and electron storage pathways in *G. sulfurreducens*.

INTRODUCTION

G. sulfurreducens has been used as a reference model in the study of the physiological features of *Geobacter* species, as it was the first species with a complete genome sequenced and with a genetic manipulation system developed (106,134) and it was shown that the ability of performing EET is related with the extremely high abundance of *c*-type cytochromes (105,134,182). It was proposed that the electrons released by the oxidation of organic molecules are transferred into the periplasmic space via two different constitutive inner membrane pathways formed by the transmembrane cytochromes CbcL (GSU0274) and ImcH (GSU3259) (171,172), and that a network of periplasmic *c*-type cytochromes establish the interface with the outer membrane electron transfer components that ultimately reduce the extracellular acceptors (135).

The periplasmic dodecaheme cytochrome GSU1996 and its homologues GSU0592 and GSU2210 were proposed to act as capacitors for electron storage in the absence of external acceptors (117). Both GSU0592 and GSU2210 were found to be more expressed under growth conditions with Fe(III) oxide, while GSU1996 was found to be more abundant in the presence of Fe(III) citrate (179).

The electron transfer mechanism processes performed by the C-terminal half of the cytochrome GSU1996 were recently investigated (256) and the data obtained suggested that GSU1996 may function as a nanowire device. However, the redox partners of this protein remain to be identified.

This is one of the major interrogations that needs to be addressed, in order to understand how *G. sulfurreducens* is able to conduit EET and perform electron storage. In order to answer these questions, in this work NMR chemical shift perturbation measurements were used to explore the interaction between GSU1996 and the triheme cytochromes that belong to the Ppc's family. PpcA is one of the most abundant components in the periplasmic space of *G. sulfurreducens* and its homologues PpcB, PpcC, PpcD and PpcE may also be potential partners of the dodecaheme GSU1996, although they possibly play distinctive roles in *G. sulfurreducens* (190,257,258). PpcA (GSU0612), PpcB (GSU0364), PpcC (GSU0365) and PpcD (GSU1024) were found both in Fe(III) citrate and Fe(III) oxide cultures. While PpcB was found to be more abundant under soluble electron acceptor growth conditions, PpcD showed higher abundance in the presence of insoluble acceptor conditions (179) and PpcA had similar abundance in both conditions. PpcE (GSU1760) was only detected in soluble acceptor growth conditions (179). The thermodynamic properties of PpcA and PpcD revealed a redox-Bohr effect that may be indicative of its participation in e^-/H^+ energy transduction mechanisms that support cellular growth (259).

Recent proteomic approaches based on affinity chromatography coupled with mass spectrometry techniques have been successfully used to identify novel interacting partners of human and plant *c*-type cytochromes (260,261) and can be explored in the future to target for other putative GSU1996 redox partners. The results obtained in the present work showed that GSU1996 and PpcA interact in a transient manner with the formation of a functional redox complex, which leads to the proposal of a unique electron transfer pathway during EET processes in *G. sulfurreducens*. This information adds an essential piece of information to the complex enigma encompassing *G. sulfurreducens* EET

mechanisms, and provides foundations towards the development of efficient bioelectrochemical applications in fields such as the production of bioenergy and bioremediation.

MATERIALS AND METHODS

Bacterial strains and plasmids

G. sulfurreducens PCA and *S. oneidensis* MR-1 cells were used to clone the *gsu1996* gene and the signal peptide derived from the small tetraheme cytochrome (STC, SO_2727), respectively. In order to obtain GSU1996 and its fragment AB, heterologous expression was tested aerobically under different conditions in several *E. coli* strains – BL21(DE3) (262), JM109 (263), JCB7123 (264) – and in *S. oneidensis* MR-1 (265). All *E. coli* strains harbored the pEC86 plasmid that contains the cytochrome *c* maturation System I, necessary to the proper assembly of the heme groups in *c*-type cytochromes produced under aerobic conditions (161).

G. sulfurreducens cells were cultured in NBAF liquid media supplemented with 0.1% (wt/vol) yeast extract and 1 mM cysteine with a final pH of 6.7 (106). *S. oneidensis* cells were cultured in Luria-Bertani liquid medium (266), with both species grown at 30°C. Genomic DNA from *G. sulfurreducens* and *S. oneidensis* was extracted with NZY Tissue gDNA Isolation kit (NZYTech, Portugal). The *gsu1996* gene with its native signal peptide was cloned into pBAD202/D-TOPO® vector (Invitrogen, USA) with the primers listed in Table 5.1 according to Shi *et al.* (267) (plasmid pBAD_gsu1996). In another construct, the native signal peptide of *gsu1996* was replaced by the sequence of the signal peptide derived from the STC from *S. oneidensis* to produce a chimeric gene, following the procedure described by Costa *et al.* (268). This chimeric gene (named stcsp_gsu1996) was also cloned into pBAD202/D-TOPO® vector (Invitrogen, USA) (plasmid pBAD_stc-gsu1996).

The expression plasmid of fragment AB from GSU1996 was constructed through modification of the plasmid pBAD_stc-gsu1996 with the NZYMutagenesis kit (NZYTech, Portugal) where a stop codon was inserted between domains B and C to avoid expression of fragment CD (Table 5.1). All the constructs were confirmed by GATC Biotech. The correct constructs were later transformed in *E. coli* and *S. oneidensis* for the production of the proteins.

Protein expression and purification

Positive transformants of *S. oneidensis* and *E. coli* harboring pBAD_gsu1996 or pBAD_stcgsu1996 were used for expressions tests, where different media, induction times and inducer concentrations were tested.

BugBuster™ Protein Extraction Reagent (Novagen, USA) was used to check the best overexpression conditions. Since in the case of *S. oneidensis* it was not possible to accomplish purification of GSU1996 (see Results – Expression and purification of cytochrome GSU1996 and its fragment AB), the *E. coli* strain selected for expression was BL21(DE3).

Briefly, the transformants of *E. coli* BL21(DE3) harboring both pEC86 and pBAD_stc-gsu1996 were grown in 2 L Erlenmeyer flasks containing 1 L of Terrific Broth medium supplemented with 34 µg/mL

Table 5.1 – Oligonucleotides used in the construction of plasmids pBAD_gsu1996, pBAD_stc-gsu1996 and pBAD_stc-fragment_AB. In the forward primers gsu1996_FW and stcsp_FW a stop codon (in italic) and the ribosome binding site (in bold) were included to avoid fusion with HP-thioredoxin present in the pBAD202/D-TOPO vector (267). In order to construct the expression plasmid for fragment AB, pBAD_stc-gsu1996 was modified and primers fragment_AB_FW and fragment_AB _RV insert a stop codon that prevents expression of fragment CD (in italic).

Name	Sequence 5' to 3'
pBAD_gsu1996	
gsu1996_FW	CACC*TAA***GAAGGAGATATACATCCC**ATGAA
gsu1996_RV	TTACATGTTGTGGCACTTCACACAGTCATC
pBAD_stc-gsu1996	
stcsp_FW	CACC*TAA***GAAGGAGATATACATCCC**GTGAGCAAAAAACTATTAAG
stc_gsu1996_RV	AACATTTTTCGTCTCCTTGGCAAATGCGGTTGGC
stc_gsu1996_FW	GCCAACCGCATTTGCCAAGGAGACGAAAAATGTT
gsu1996_RV	TTACATGTTGTGGCACTTCACACAGTCATC
pBAD_stc-fragment_AB	
fragment_AB_FW	CACCGTTTTCGGCGGGGTCAT*TTA*GCCCTTGTGGCACTTGCCGCA
fragment_AB_RV	TGCGGCAAGTGCCACAAGGGC*TAA*ATGACCCCGCCGAAAACGGTG

chloramphenicol (NZYTech, Portugal) and 50 µg/mL kanamycin (NZYTech, Portugal) to mid-exponential phase at 30°C with a shaking speed of 200 rpm. Protein expression was then induced with 2 mM L(+)-arabinose (Acros Organics). After overnight incubation under the same conditions, the cells were harvested by centrifugation at 8000×g for 10 min at 4°C.

The cell pellet was suspended in 20 mM NaPi buffer pH 5.9 with protease inhibitors (1 mM of each phenylmethylsulfonyl fluoride (Sigma-Aldrich) and benzamidine-HCl (Sigma-Aldrich)) and DNase I (1 mg/mL) (Roche).

Cell disruption was attained by three passages through a French Press (Thermo ScientificTM IEC) at a pressure of 1400 psi (1 psi=6.9 kPa). Cell debris were removed by centrifugation at 10000×g for 20 min at 4°C, and the supernatant was ultracentrifuged at 150000×g for 1 h and 30 min at 4°C in an Optima LE-80K Beckman Coulter ultracentrifuge. The supernatant with the soluble protein was dialyzed in 20 mM NaPi buffer pH 5.9, and the resulting sample was loaded onto cation-exchange columns (HiTrap SP HP, GE Healthcare Life Sciences) pre-equilibrated with the same buffer. The fractions were eluted with a linear gradient of 0–500 mM NaCl. The fractions with GSU1996 were pooled, concentrated and the buffer was exchanged to 20 mM NaPi buffer pH 7.8 with 100 mM NaCl added. This sample was then loaded onto a HiLoad™ 16/600 Superdex™ 75 prep grade column (GE Healthcare Life Sciences) pre-equilibrated with the latter buffer. Fragment AB best overexpression conditions were determined in the same manner as for cytochrome GSU1996. Accordingly, fragment AB was expressed in *E. coli* JCB7123 harboring both pEC86 and pBAD_stc-fragment_AB, with the same expression protocol described above for GSU1996. In this case, protein expression was achieved through induction with 1 mM L(+)-Arabinose (Acros Organics). Purification of fragment AB was performed as described by Londer *et al.* (196). Fragment CD and PpcA were expressed and purified as previously described (196,269). PpcB-E expression and purification was performed as described in earlier work (232,258,269) with the minor changes explained next. PpcB-E were expressed in *E. coli* BL21(DE3)

harboring plasmid pEC86 (161) and 100 µg/mL ampicillin was used instead of carbenicillin in the growth media. Protein expression was induced in all cases by addition of 10 µM isopropyl β-D-1-thiogalactopyranoside and cells were disrupted by three passages in a French Press (Thermo Scientific™ IEC) at a pressure of 1400 psi (1 psi=6.9 kPa).

All the chromatographic steps were performed in an ÄKTAprime™ plus FPLC system (GE, Amersham Biosciences). The presence and purity of the proteins were confirmed by 12% SDS-PAGE with both heme (245) and Coomassie blue staining. A single band on the SDS-PAGE confirmed the purity of the proteins.

1D ^{1}H-NMR was used to check for the correct folding of the proteins. All protein concentrations were determined by UV-visible spectroscopy with the specific absorption coefficient of the α-band at 552 nm determined for the reduced cytochrome PpcA ($\Delta\varepsilon_{552nm}$ = 32.5 mM^{-1} cm^{-1} per heme) (152). The cytochrome samples were completely reduced by the addition of a diluted solution of sodium dithionite (Sigma).

NMR experiments

Samples preparation

The buffers of purified proteins GSU1996, fragments AB and CD, as well as of PpcA-E were exchanged through ultrafiltration procedures with Amicon Ultra Centrifugal Filter Units (Millipore) for 45 mM NaPi buffer pH 7.0 prepared in 99.9% 2H2O (Cambridge Isotope Laboratories) with NaCl added to a final ionic strength of 100 mM and with 0.04% azide (wt/vol) (Sigma).

NMR titrations

All the NMR experiments were performed at 298 K on a Bruker Avance II 500 MHz NMR spectrometer equipped with a BBI-XYZ probe. Titrations were performed between proteins in the oxidized state as follows: 200 µM of GSU1996, fragment AB or fragment CD were titrated in 3 mm NMR tubes (Wilmad) with increasing amounts of Ppc's (stock solution of 2 mM) with ratios of Ppc's/protein ranging from 0 to 10. 1D ^{1}H-NMR spectra were recorded for each titration step. In the case of fragment AB and fragment CD, the experiments were only attained with PpcA for the 1:10 ratio. The pH of the samples was confirmed before and after each titration.

Data analysis

The effect of the addition of PpcA-E to GSU1996 cytochrome heme methyl proton chemical shift was analyzed by comparison of the NMR spectra obtained in the absence and in the presence of the Ppc's with the TopSpin™ 3.2 NMR software from Bruker Biospin. All the chemical shifts are reported in parts per million (ppm) and the ^{1}H chemical shifts were calibrated with the water signal as internal reference. Only chemical shift perturbations equal to or larger than 0.03 ppm were considered significant (270). The chemical shift variation of the heme methyl signals of GSU1996 upon addition of Ppc´s was used to determine the dissociation constant between the cytochromes with a two-parameter

nonlinear least-square fit of the data that considers a one-site binding model and corrects for dilution effects (Equation 5.1) (199,271).

$$\Delta\delta_{bind} = \frac{1}{2}\Delta\delta_{max}\left(A - \sqrt{A^2 - 4R}\right) \quad \textbf{Equation 5.1}$$

In Equation 5.1, $\Delta\delta_{bind}$ is the chemical shift change relative to the GSU1996 free protein when titrating with Ppc's, $\Delta\delta_{max}$ is the chemical shift change as $R = \frac{[Ppc's]}{[GSU1996]} \rightarrow \infty$ and A is described in Equation 5.2, with K_d as the dissociation constant.

$$A = 1 + R + \frac{K_d([GSU1996]_{initial}R + [Ppc's]_{stock})}{[GSU1996]_{initial}[Ppc's]_{stock}} \quad \textbf{Equation 5.2}$$

Data regarding the methyl signals of GSU1996 that showed identical behavior were fitted simultaneously to define the dissociation constant with the Microsoft® Office Excel add-in Solver (Generalized Reduced Gradient Nonlinear Algorithm (272)). Experimental uncertainty was estimated from the covariance matrix with an experimental uncertainty given by the NMR spectral resolution.

Binding reversibility

The binding reversibility between GSU1996 and the Ppc's was evaluated after NMR titrations as described: each final GSU1996:Ppc's mixture was loaded into a HiLoad™ 16/600 Superdex™ 75 prep grade column (GE Healthcare Life Sciences) connected to an ÄKTAprime™ plus FPLC system (GE, Amersham Biosciences) and the efficiency of the separation was assessed both by the chromatographic data and 12% SDS-PAGE with Coomassie blue staining.

1D ^{1}H-NMR spectra were further acquired in the same conditions of the titrations to check for the integrity of the pure proteins after separation.

RESULTS

Expression and purification of cytochrome GSU1996 and its fragment AB

The existence of the cell machinery necessary for the production of *c*-type cytochromes in *S. oneidensis* and *E. coli* and the ease handling of cultures, in particular their capability to grow under aerobic conditions, turn these organisms in the best candidates to perform heterologous expression, when compared with *G. sulfurreducens*. Albeit some degree of expression occurred in *S. oneidensis*, the profusion of other *c*-type cytochromes (273) prevented the proper purification of GSU1996. The insertion of the small tetraheme cytochrome signal peptide from *S. oneidensis* prior to the *gsu1996* gene was expected to increase the expression yield of GSU1996, as previously observed for other proteins (274). In fact, the purification of GSU1996 yielded approximately 1 mg of GSU1996 per liter of *E. coli* culture, which is two times higher compared with that obtained with previous expressions systems (194).

In the case of fragment AB, *E. coli* JCB7123 harboring pEC86 and pBAD_stc-fragment_AB plasmids was the most effective strain. A final yield of approximately 1 mg of protein per liter of culture was obtained, which corresponds to nearly four times the one earlier reported (196). 1D ^{1}H-NMR spectra confirmed the proper assembly of GSU1996, fragment AB, fragment CD and Ppc's in the periplasmic space of *E. coli* (221) (Figure 5.1 and Figure 5.S1).

Chemical shift perturbation experiments

NMR spectroscopy is exquisitely sensitive to changes in the nuclei chemical environment. The structures of the cytochromes GSU1996 and Ppc's showed that the hemes are considerably exposed to the solvent (191,195) and therefore, in the case GSU1996 and the Ppc's establish an electron

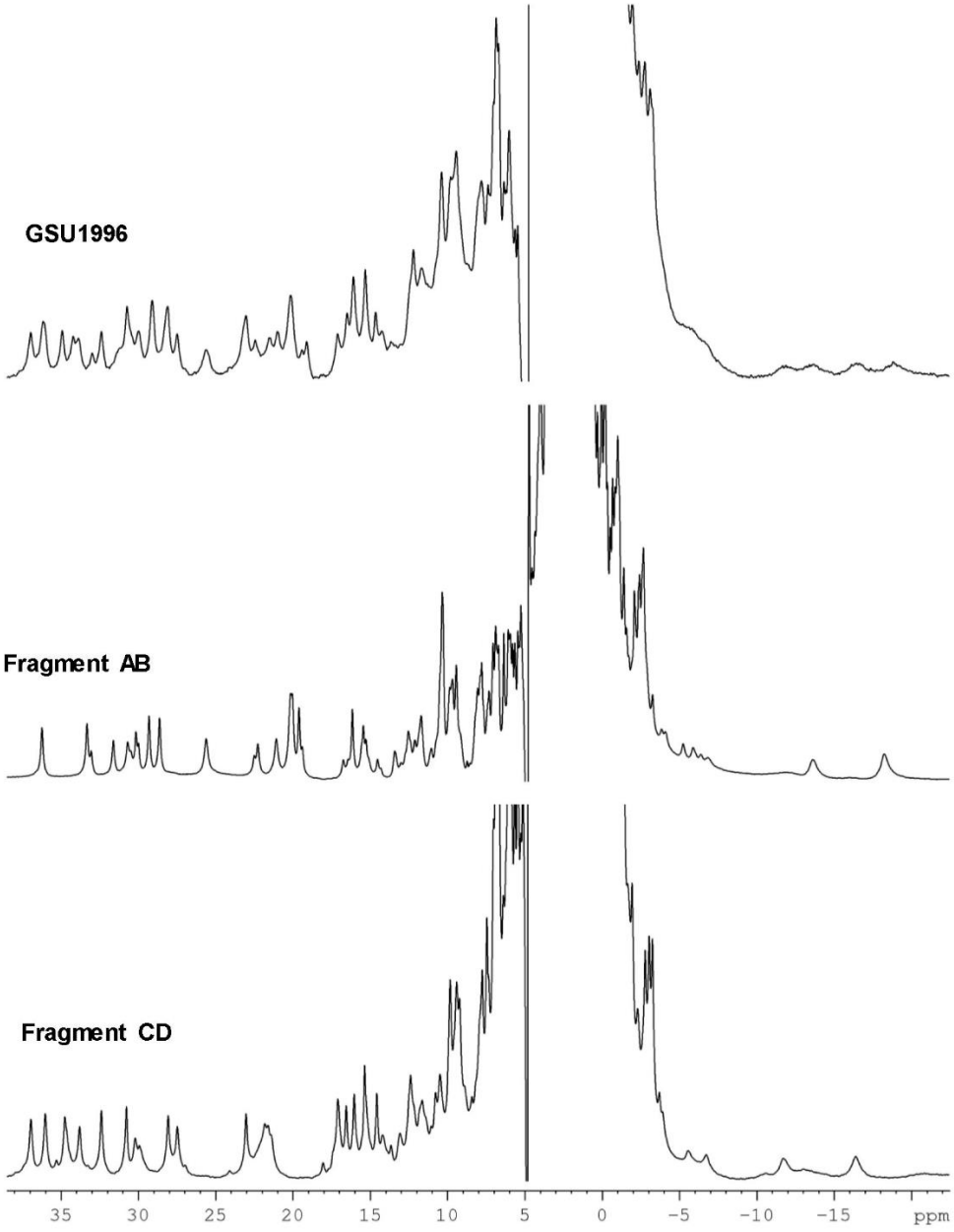

Figure 5.1 – 1D ^{1}H-NMR spectra of GSU1996, fragment AB and fragment CD at pH 7 and 298 K.

transfer complex it is expected that the chemical shift and/or broadness of the NMR heme methyl proton signals will be affected.

In the present study, the proton signals of cytochrome GSU1996 that were clearly visible in the paramagnetic region of the NMR spectra (from 40 to 25 ppm, Figure 5.1) and those of the Ppc's (from

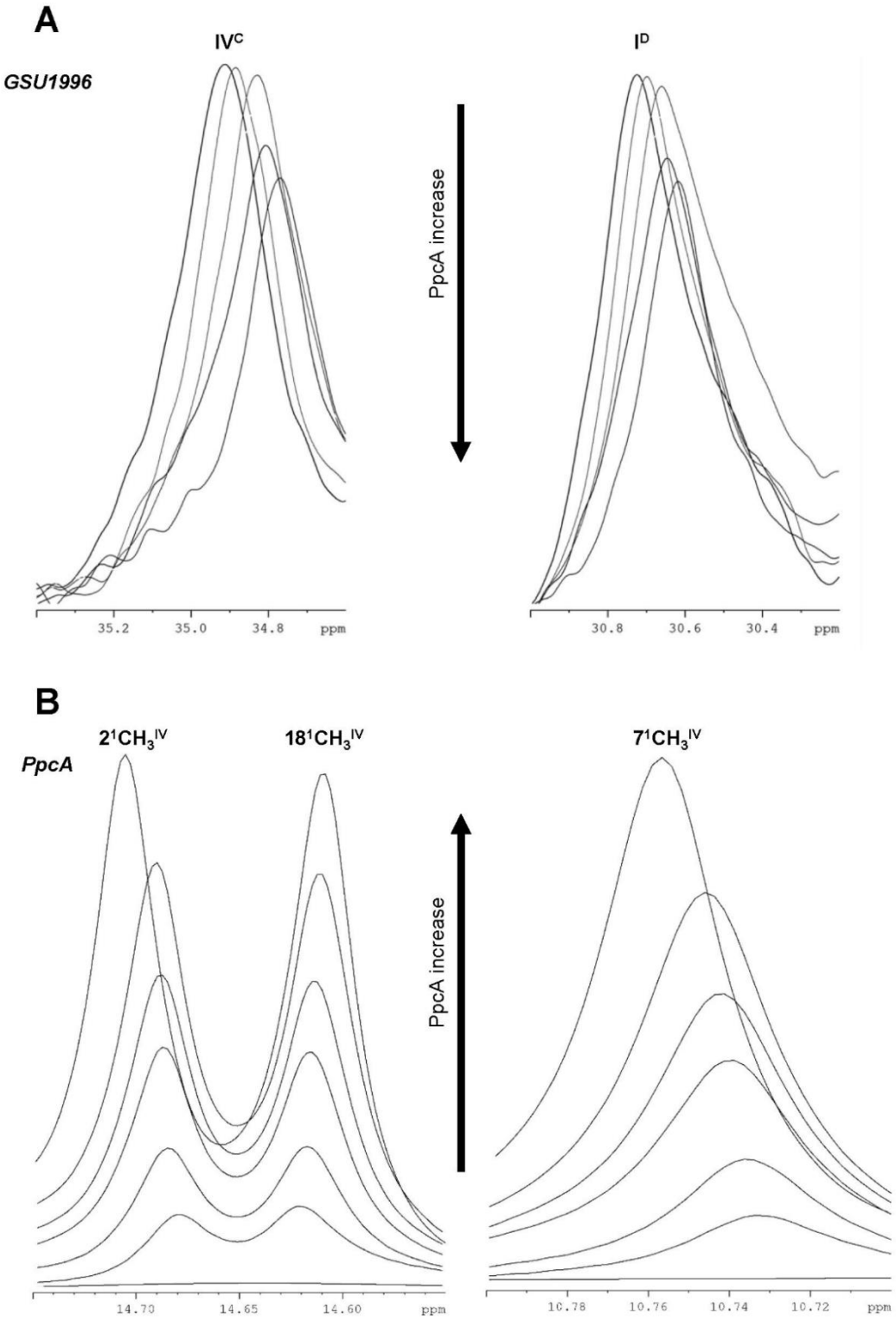

Figure 5.2 – Expansions of 1D ^{1}H-NMR spectra showing the most affected heme methyl signals of GSU1996 (A) and PpcA (B).

27 to 9 ppm, Figure 5.S1) were followed upon addition of increasing amounts of Ppc's (see Figure 5.2 for an example).

Unfortunately, in the case of the interaction studies between GSU1996 and PpcB further elucidation of a putative interaction between these proteins was prevented, as it was detected that the nanowire underwent some degree of protein degradation in the time course between the sample preparation and the NMR acquisition. This can be observable in the unusual multiple signals observed in the NMR spectra below 30 ppm (Figure 5.3).

The data obtained showed changes both in the chemical shift and broadness of particular heme methyl signals from GSU1996 upon the presence of PpcA, PpcC, PpcD and PpcE, which may indicate an interaction between the proteins. The dissociation constant determined for GSU1996 and PpcC yielded 8.91 (0.10) mM, 2.23 (0.10) mM with PpcD and 5.98×10^{4} (0.10) mM for PpcE, which is not in agreement with the existence of specific interactions. In the case of the dissociation constant determined for GSU1996 and PpcA, a value of 1.17 (0.10) mM was obtained, which is consistent with previously values reported for transient interactions between electron transfer complexes (217,275,276). The most affected signals in GSU1996 correspond to heme methyl signals at 34.91 and 30.72 ppm (Figure 5.2 A) and the progressive shift of these signals with the increasing addition of PpcA indicates that the free and bound forms of GSU1996 are in fast regime on the NMR time scale. Likewise, PpcA heme IV signals, in particular those of the solvent exposed heme methyls $2^{1}CH_3$ and $7^{1}CH_3$, are the most affected by the presence of GSU1996 (Figure 5.2 B). The dependence of the chemical shift perturbation as a function of [PpcA]/[GSU1996] ratio returned hyperbolic binding curves (Figure 5.4).

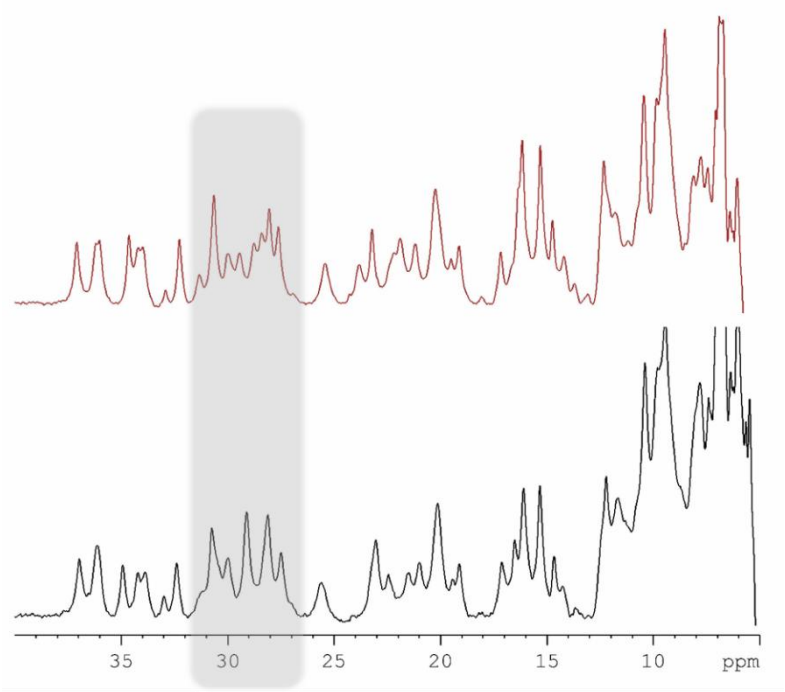

Figure 5.3 – Heme methyl region expansions of 1D ^{1}H-NMR spectra of GSU1996 properly folded (below) and GSU1996 that experienced possible degradation (above). The shadowed box highlights one of the most affected regions in GSU1996.

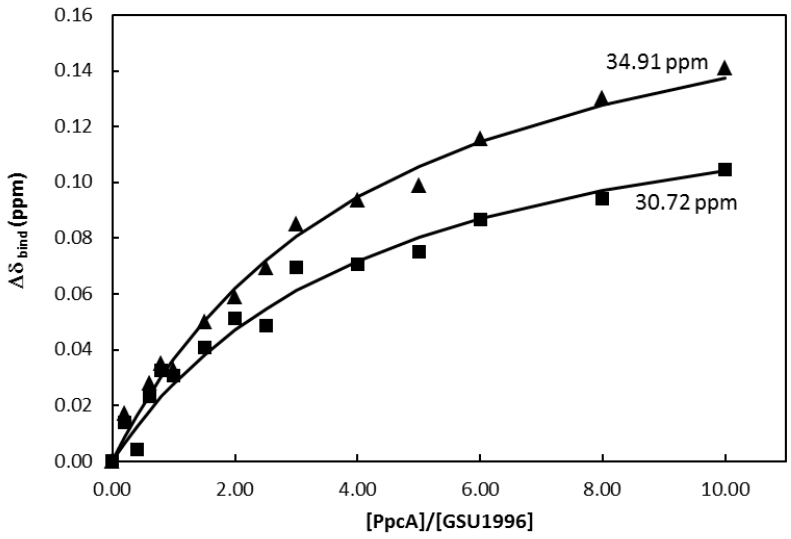

Figure 5.4 – Binding curves of GSU1996 from *G. sulfurreducens* with PpcA. The chemical shift perturbation of the heme methyl signals at 34.91 and 30.72 ppm (see Figure 5.2) are plotted as a function of the PpcA:GSU1996 molar ratio. The solid lines represent the best global fit to the 1:1 model.

Furthermore, chromatographic and SDS-PAGE data and 1D ^{1}H-NMR spectra acquired for the pure proteins after separation confirm that the interactions between GSU1996 and the PpcA is completely reversible (Figure 5.5).

Structural map of the interaction site between cytochromes GSU1996 and PpcA

Comparison of the NMR spectra obtained for GSU1996 fragments AB and CD with that of the whole protein (Figure 5.1) suggests that the C-terminal of the molecule is involved in the interaction with PpcA.

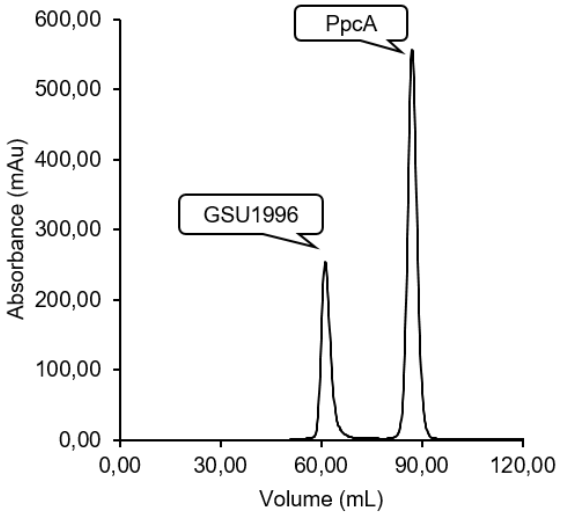

Figure 5.5 – Gel filtration of the mixture GSU1996:PpcA at the end of the NMR titration experiments. GSU1996, with the larger molecular weight, is the first to be eluted and it is readily followed by PpcA, the smaller cytochrome, which indicates the reversible nature of the binding between both proteins.

This was further confirmed by chemical shift perturbation studies between PpcA and fragments AB and CD carried out in the same experimental conditions as for GSU1996 (Figure 5.6).

The data gathered showed that only signals from fragment CD change upon interaction with PpcA (Figure 5.6). The most affected signals of GSU1996 at 34.91 and 30.72 ppm were assigned to heme IV of domain C and heme I of domain D, respectively (277).

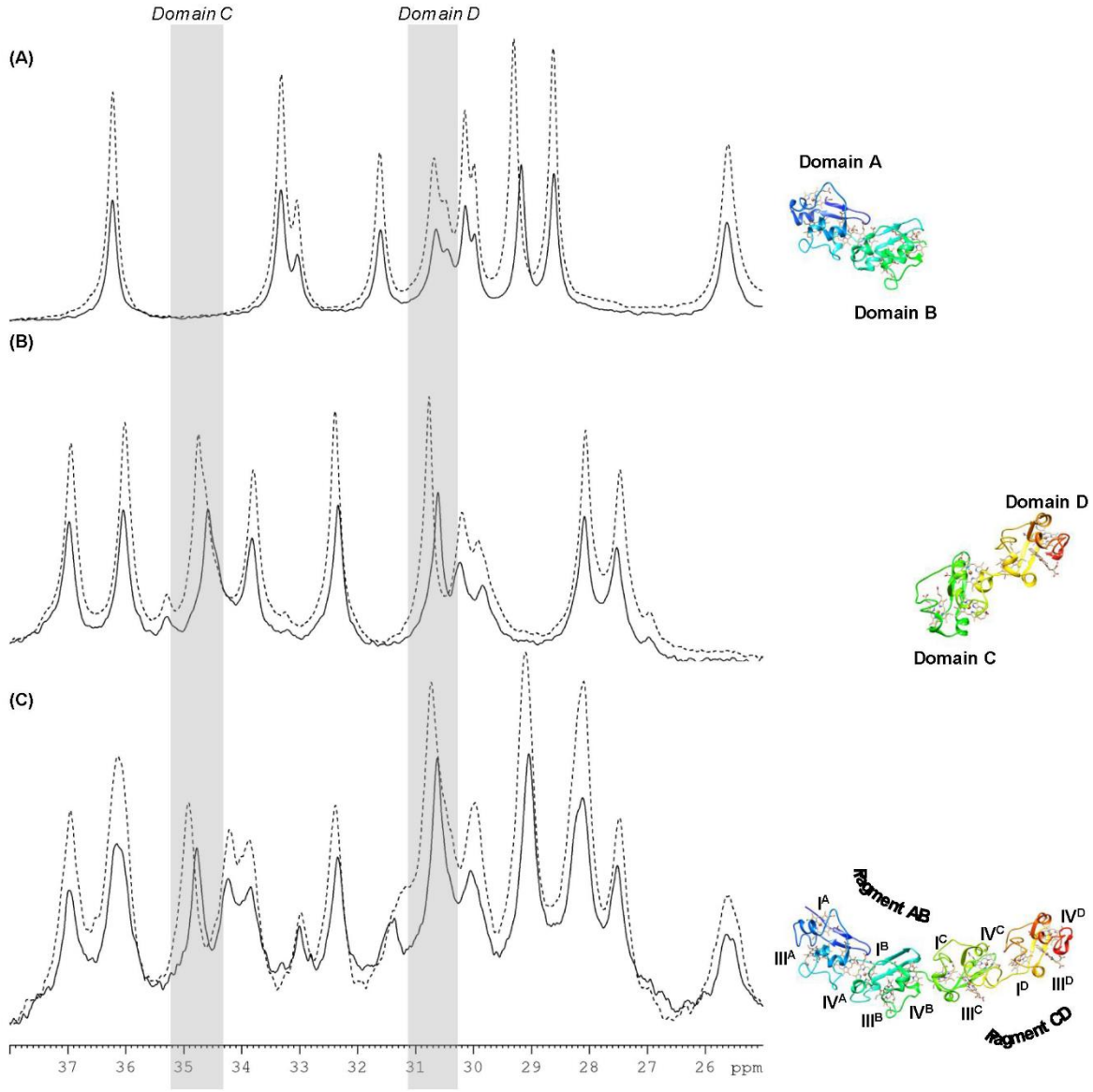

Figure 5.6 – Expansion of the low-field region of 1D ^{1}H-NMR spectra obtained for GSU1996 and its two fragments in the absence (dashed lines) and in the presence (solid lines) of PpcA (1:10). The most affected signals from domain C and D are highlighted in the gray boxes. Crystal structures were produced with UCSF Chimera 1.6.3 software (320) with data accessible from PDB's 3OV0 (GSU1996), 3OUQ (fragment AB) and 3OUE (fragment CD) (321).

DISCUSSION

Until the disclosure of the mechanistic biomolecular information surrounding the EET processes it will not be possible to improve and implement biotechnological applications sustainable at an industrial scale. It is then crucial to understand the EET mechanisms performed by *Geobacter*, including the identification of redox partners and elucidation of their mode of interaction. In respiratory electron transfer pathways, the interactions between redox partners occur in a transient manner, to maintain high-turnover rates and provide the basis to withstand a continuous electron flow (214,215). In *G. sulfurreducens*, MHCs have a key role in extracellular respiration and are responsible for electron transfer processes across the cell envelope and electron storage (6,117,118,176,182). A new family of cytochromes was proposed to contribute to the enhancement of the cellular electron storage capacity in *G. sulfurreducens* (117), where GSU1996 is the only cytochrome with a known three-dimensional crystal structure (195).

The organization of the hemes along the polypeptide chain in a nanowire like arrangement and the recent thermodynamic and kinetic characterization of fragment CD indicates that GSU1996 is able to work as an electron capacitor (195,256). It was shown that heme III from domain D at the edge of the C-terminal of the protein is thermodynamic and kinetically competent to receive electrons from physiological partners.

However, the GSU1996 redox partners and their interaction interfaces are still unknown. Interaction studies of redox partners are defying due to the small lifetime of the complex that is usually on the order of milliseconds (217). NMR spectroscopy is a choice of excellence to detect transient protein-protein interactions due to its high sensitivity, which allows readily detection of changes in the chemical environment (217).

Indeed, in chemical shift perturbation experiments, proteins are monitored during the course of a titration where the formation of the complex modifies the chemical environment of the nuclei at the interface of the interaction site (278). Therefore, chemical shift perturbation data gathered by NMR provide information about the complex interface and also the relative orientation of the proteins, even though these complexes show low affinity (214,217,270).

The interaction studies performed in this work between GSU1996, as well as between its C- and N-terminal fragments with PpcA show that the dodecaheme cytochrome interacts in a transient manner with the heme IV region of PpcA with the formation of a redox complex with a dissociation constant of 1.17 mM. Heme IV from domain C and heme I from domain D are involved in the interacting region between the two proteins, a feature that is reinforced by the structural characteristics of GSU1996. Indeed, domains C and D are connected by a flexible linker (195), suggesting that in solution they may slightly bend in the presence of redox partners to allow the formation of an interaction site relevant for electron transfer. Overall, the results obtained clearly suggest that the two proteins may be in vivo periplasmic partners, and this is consistent with the previous proteomic studies in *G. sulfurreducens* which showed that both proteins are expressed when acetate and Fe(III) citrate are used as electron donor and acceptor, respectively (152,179,182). Although it is possible that GSU1996 may have other partners, the studies performed with PpcC-E did not reveal interactions with the dodecaheme.

Thus in the presence of electron acceptors (*e.g.* iron sources) PpcA, that may be reduced via CbcL, ImcH or MacA inner membrane cytochromes (see Figure 5.7), will transfer electrons to the extracellular environment through porin-cytochromes Oma-c/B (GSU2738, GSU2739 and GSU2737) and Oma-c/C (GSU2732, GSU2733 and GSU2731) (168). On the other hand, in the absence of extracellular electron acceptors it is then plausible to suggest that electron transfer components with high number of hemes, like the nanowire GSU1996, may be used as large cell storage units to sustain cell survival until new sources are available. This hypothesis is further supported by studies on the electrochemical performance of *G. sulfurreducens* biofilms that showed that (i) *c*-type cytochromes abundance positively correlates with *G. sulfurreducens* biofilms capacitance and that these biomolecules are key players in cellular charge storage (117,118); (ii) there is no significant self-discharge behavior in the course of time when in conditions of lack of electron acceptors (118) and (iii) current production was impaired in the absence of electron donors but with no impact in capacitance (279).

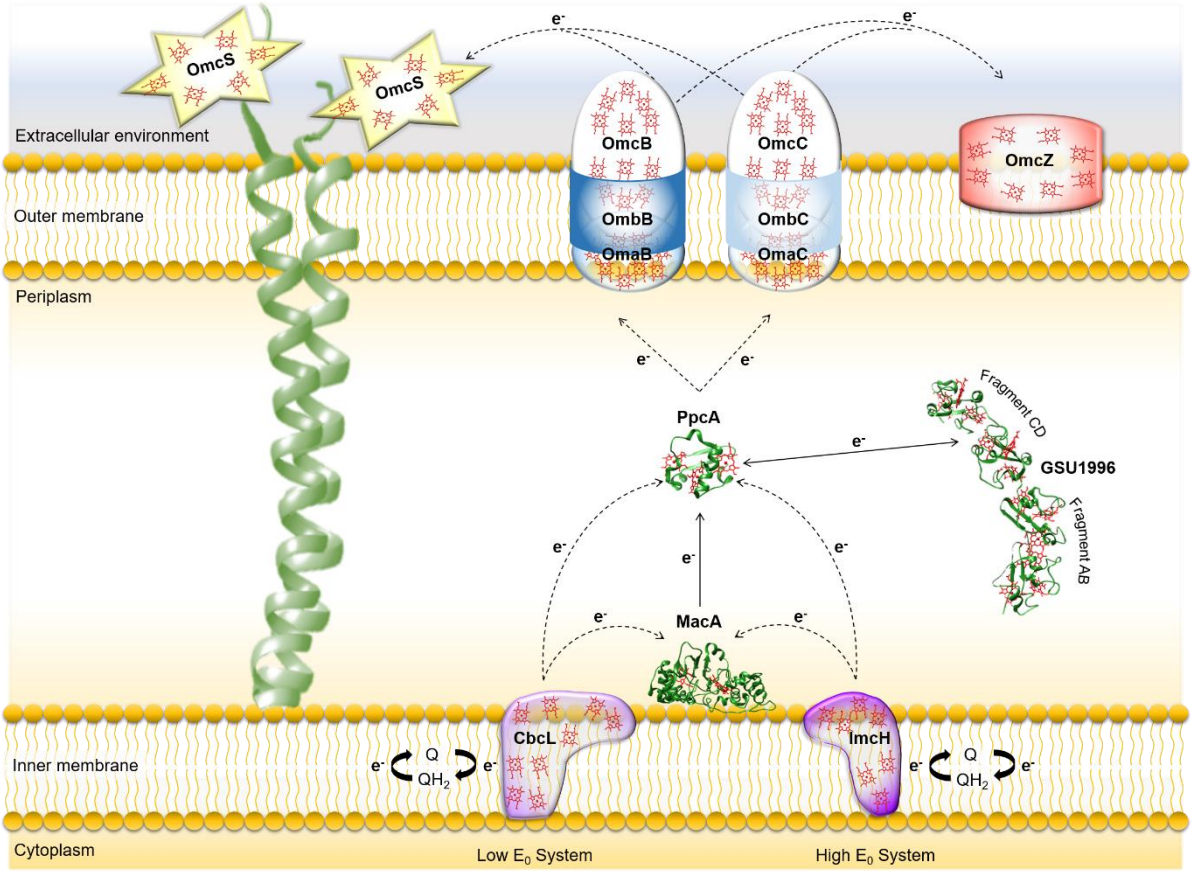

Figure 5.7 – Model for extracellular electron transfer on *G. sulfurreducens* mediated by porin cytochromes. The inner membrane quinol oxidases CbcL (proposed to be required for respiration of electron acceptors with redox potentials lower than −0.1 V versus normal hydrogen electrode) and ImcH (proposed to be required for respiration of electron acceptors with redox potentials higher than −0.1 V versus normal hydrogen electrode) receive electrons from the quinone pool (170) and transfer them to the extracellular environment through a net of *c*-type cytochromes across the periplasm and porin-cytochrome complexes (Oma-c/B and Oma-c/C) located on the outer membrane. When in lack of terminal acceptors the electrons can be stored in large MHCs, like GSU1996, and provide for cell survival until new sources of acceptors became available. The tridimensional structures indicated in the figure were produced with UCSF Chimera 1.6.3 software (320) with data accessible from PDB's 4AAL (MacA), 2LDO (PpcA) and 3OV0 (GSU1996) (321).

The similar redox-active windows of *G. sulfurreducens* cytochromes GSU1996 and PpcA at pH 7 (135) support a thermodynamically sustainable interaction between GSU1996 and PpcA, and point also for the reversibility of the direction of the electron flow.

Therefore, when electron acceptors become available, the electrons stored at GSU1996 may be used to reduce the electron acceptors, discharging the cell and leaving GSU1996 available to be re-reduced.

According to this hypothesis and in light of the data gathered, it is possible that the interaction between both GSU1996 and PpcA may be triggered by a cell or environmental signaling mechanism to respond to the devoid of external electron acceptors, favoring the interaction between the two cytochromes rather than the electron transfer to terminal acceptors. The precise mechanism that modulates the functional binding between GSU1996 and PpcA and/or their redox potentials is still unknown.

However, there are examples in the literature describing the switch from functional to non-functional interactions. This is the case of cytochrome *c*, for which it was demonstrated that the post-translational modification by phosphorylation or nitration of tyrosine residues is important to control its multiple functions (280,281). Cytochrome *c* is an electron transfer carrier in the mitochondrial intramembrane space but it has also been shown to play crucial roles in programmed cell death, a switch that can be fine-tuned by the nitration of specific tyrosine residues.

In fact, nitration of tyrosine residues impaired the functions of cytochrome *c* in cell life (respiration) and cell death (apoptosis) (282,283) as a result of protein structural changes that shift the cytochrome redox potential and lead to the formation of non-functional apoptosome (280,281). Similar mechanisms might account for the functional to non-functional switch between GSU1996 and PpcA.

The present study shows for the first time an interaction between two periplasmic cytochromes from *G. sulfurreducens* and contributes to the current knowledge of the periplasmic cytochrome network interactions that are relevant for EET and electron storage pathways in this organism. This knowledge is of significant importance to understand the EET performed by this model organism, and contributes to the rational design of environmentally friendly and viable technology based in electrosynthesis naturally carried out by *Geobacter* bacteria.

INTERACTIONS SUPPLEMENTARY DATA

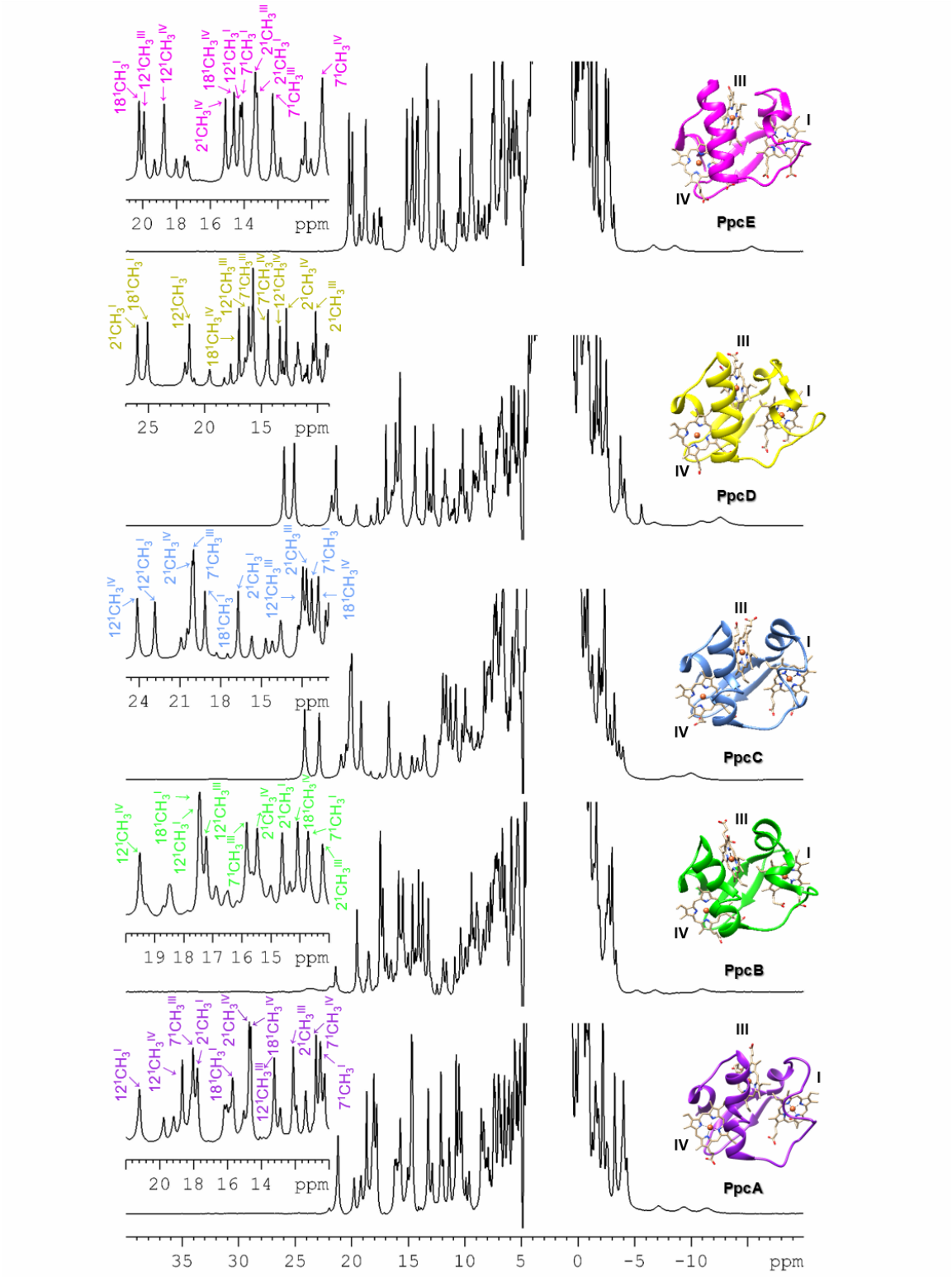

Figure 5.S1 – 1D ^{1}H-NMR spectrum of the Ppc's at pH 7 and 298 K. The insets show the expansion of the low-field region with the Ppc's heme methyl signals labeled ($2^{1}CH_3$, $7^{1}CH_3$, $12^{1}CH_3$ and $18^{1}CH_3$). The specific assignment of the Ppc's heme signals was previously reported (324). Solution structure of PpcA was produced with data accessible from PDB ID code 2MZ9 (325) and structures of PpcB-E with data from PDB ID codes 3BXU (232), 3H33 (258), 3H4N (258) and 3H34 (258) with resource to UCSF Chimera 1.6.3 software (320).

CHAPTER 6

ON THE QUEST TO UNVEIL ELECTRON TRANSFER CHAINS OF *GEOBACTER SULFURREDUCENS*

Contents

ABSTRACT

New advances regarding the knowledge of the electron transfer networks of *Geobacter* species are required and in order to do so, the building blocks of these chains must continue to be unveiled. Here, the heterologous expression of the nanowire cytochrome GSU2210, of the outer membranes multiheme cytochromes OmcE and OmcS from *G. sulfurreducens* was attempted with resource to pBAD vector. Unfortunately, under the experimental conditions tested, none of the proteins was successfully produced.

A new approach to label cytochromes based in a tetracysteine tag was also tested in the outer membrane cytochrome OmcF that aimed to enable the *in vivo* tracking of these proteins. Several expression conditions were tested to validate the expression of the properly folded protein, although none returned the OmcF-tagged protein.

INTRODUCTION

Extracellular electron transfer (EET), defined as the electron exchange reactions that occur between microorganisms and their surrounding environment, is a remarkable process that is carried out during biogeochemical cycles. In this form of respiration, redox potential differences that occur along the oxidation and reduction of chemical compounds – where electrons are transferred from low potential electron donors to higher potential electron acceptors –, are converted into a life supporting form of energy, ATP (284,285). Indeed, several bacteria are able to transfer electrons to and from soluble and insoluble extracellular terminal electron acceptors in nature to withstand their respiratory metabolic processes (34,286). Examples of these electron acceptors are Fe(III) and Mn(IV) metal oxides, soluble humic acids or even electrodes (26). The energy transduction reactions are executed by chains of redox proteins that establish pathways headed for a sustained and controlled electron flow (215,216). Nevertheless, the mechanisms diverge among species and their unveiling is still in its early days.

The electron flux that arises from these natural metabolisms have been diverted to be the basis of numerous Green Technologies currently under development. Microbial electrochemical systems (MXCs) make use of these microorganisms to transform the decomposing biomaterials chemical energy into electrical current and added-value chemical compounds. Such applications are created under the form of microbial desalination cells (MDCs) for water desalination (287–291); MECs (292–294) or microbial electrosynthesis cells (MESs) for chemical production (295,296); microbial remediation cells (MRCs) for environmental contaminants remediation (295–298) and MFCs for power generation (299–301). Unfortunately, these applications are restrained by the power output of the microbial devices which is still far from attaining the one retrieved by hydrogen fuel cells (302). Nonetheless, numerous advantages arise from MXCs, among which are the low cost of the carbon sources needed to sustain their survival, and the needless use of noble elements when these bugs are employed as catalysts – simple graphite felt can be used (302). MFCs based supercapacitors have been pointed as prospective storage devices, as they are able to stock electrons at a low current and high potentials, and discharge them as electric current. These devices present the advantages of having a large surface to volume ratio, effective mass transport and small charges transfer distances (303).

It is then of crescent interest to develop large-scale sustainable MXCs systems. These systems make use of electrochemically active bacteria that are able to perform electron transfer to electrodes through a network of redox active components like *c*-type cytochromes, pili and soluble electron shuttles.

Geobacteraceae are an example of promising bacteria towards the scaling-up of these systems. *Geobacter* species ability to perform the reduction of soluble ions to more insoluble forms is already a natural contribute to bioremediation. Actually, the enrichment or stimulation of the activity of these species is an aid to slow the dispersion or even in the immobilization of dangerous metals like U(VI) (54,304,305). In MFCs, they coherently stockpile in anodes and a pre-enrichment with these bacteria may be a potential way to enhance these systems output, together with the selection or engineering of optimized strains (28,29).

Bioelectronics is another field where *Geobacter* species can be applied, once that electronical biomaterials can be developed with rather low costs, they are self-renewing and nontoxic (27). Moreover, its supercapacitor skills may be the basis to develop new biomimetic materials (26,118). Indeed, the electron storage reservoirs in these microorganisms may be the *c*-type cytochromes, as a high abundance can be observable at the naked eye by the red coloration of the cultures grown under limiting electron acceptor conditions (117). Therefore, it is of utmost importance to understand the mechanisms that underlie electron transfer in *Geobacter*.

In order to proceed this quest, the characterization of the building blocks of the electron transfer chains is required, and many components are yet to be uncovered. In the case of *G. sulfurreducens*, three examples lacking *in vitro* characterization are the nanowire cytochrome GSU2210, the outer membrane tetraheme cytochrome OmcE and the hexaheme cytochrome OmcS.

Although *in vitro* characterization provides a large amount of information that can be explored to elucidate the mode of action of these proteins and extrapolate *in vivo* roles, it is also of prime relevance to perform the study of the cytochromes in their native environment. The occurrence of such a high number of cytochromes in *Geobacter* spp. turns any effort to directly locate and study each of them in an impracticable mission. Therefore, an alternative may be to specifically tag a desired cytochrome so that it can be readily distinguishable from its counterparts in the cell.

The procedure first described by Griffin and co-workers (306) involves the modification of the protein of interest by insertion of a tetracysteine motif (CysCysProGlyCysCys). Next steps involve the monitorization of its expression in cells and labeling of the protein with membrane-permeant biarsenical dyes, such as green FlAsH or red ReAsH (Life Technologies).

In the present work, the heterologous overexpression of OmcE, OmcS and GSU2210 was attempted. A test run was also carried with the monoheme OmcF as a model in order to understand if the tetracysteine motif may be used as a tag in *c*-type cytochromes.

MATERIALS AND METHODS

In vivo labeling system approach for *c*-type cytochromes

Following the methodology reported by Griffin and co-workers (306), a *G. sulfurreducens* mutant with the required gene disrupted could be used to construct a second mutant. This second mutant will harbor the plasmid with the protein of interest with the tetracysteine motif located downstream of the gene, according to the protocol described by Hoffmann and co-workers (307). Briefly, the desired gene is amplified from the genomic DNA and the codon sequence 5′-TGTTGCCCGGGCTGCTGT-3′ is used to combine with the gene so as to encode the tetracysteine motif. This codon comprises a SmaI/XmaI restriction site (CCCGGG) which allows for the screening of positive clones. The modified gene can then be cloned into vector pCDS as described by Leang and co-workers (173). A cassette with a kanamycin-resistance marker is excised from the knockout mutant and replaced with the vector pCDS-Protein-Cys tagged. Once the tetracysteine-tagged protein is expressed by *G. sulfurreducens*, biarsenical dyes can be used to fluorescently label the protein and thus visualize it through confocal microscopy and/or fluorescence resonance energy transfer recordings.

Bacterial strains and plasmids

G. sulfurreducens PCA cells were used to clone the *gsu2210*, *omcE*, *omcS* and *omcF* genes and the signal peptide derived from the small tetraheme cytochrome (STC, SO_2727) was cloned from *S. oneidensis* MR-1 cells.

Heterologous expression of OmcE was tested aerobically under different conditions in *E. coli* strains JM109 (263) and JCB7123 (264) and in *S. oneidensis* MR-1 (265). STC-OmcE expression was tested in *E. coli* strains BL21(DE3) (262) and JM109 (263) and in *S. oneidensis* MR-1 (265), *S. oneidensis* MR-1 Δ*cymA* and *S. oneidensis* MR-1 Δ*fccA* Δ*stc*. The last two *S. oneidensis* MR-1 mutant strains were kindly provided by Dr. Liang Shi and Dr. Johannes Gescher, respectively. OmcF-tetracysteine tagged expression tests were performed in *E. coli* strains BL21(DE3) (262), JM109 (263) and JCB7123 (264) and in *S. oneidensis* MR-1 (265). All *E. coli* strains harbored the pEC86 plasmid that contains the cytochrome *c* maturation System I, necessary to the proper assembly of the heme groups in *c*-type cytochromes produced under aerobic conditions (161).

G. sulfurreducens cells were routinely cultured in NBAF liquid media supplemented with 0.1% (wt/vol) yeast extract and 1 mM cysteine with a final pH of 6.7 (106) and *S. oneidensis* cells were routinely cultured in Luria-Bertani liquid medium (266), with both species grown at 30°C. Genomic DNA from *G. sulfurreducens* and *S. oneidensis* was extracted with NZY Tissue gDNA Isolation kit (NZYTech, Portugal).

Primer constructs were designed towards insertion into pBAD202/D-TOPO® vector (Invitrogen, USA) according to Shi *et al.* (267). Primers designed for the *omcE, omcS* and *omcF* genes with its native signal peptides (plasmids pBAD_omcE, pBAD_omcS, pBAD_omcF-tetracysteine tag) are listed in Table 6.1.

Other designs (plasmids pBAD_stc-omcE, pBAD_stc-omcS and pBAD_stc-gsu2210 in Table 6.1) contemplated the replacement of the native signal peptide of *omcE, omcS* and *gsu2210* by the sequence of the signal peptide derived from the STC from *S. oneidensis* to produce chimeric genes, following the procedure described in Costa *et al.* (268).

All the constructs were confirmed by GATC Biotech. The successful constructs were transformed in *E. coli* and *S. oneidensis* aiming for the production of the proteins, as explained next.

Protein expression

Positive transformants of *S. oneidensis* and *E. coli* harboring pBAD_omcE, pBAD_stc-omcE and pBAD_omcF-tetracysteine tag were used in expressions tests, where different media and inducer concentrations (0–2 mM L(+)-arabinose from Acros Organics) were tested. Briefly, the transformants of *E. coli* or *S. oneidensis* were grown in 25 mL of media (Luria-Bertani or Terrific Broth (266)) supplemented with 34 μg/mL chloramphenicol (NZYTech, Portugal) and 50 μg/mL kanamycin (NZYTech, Portugal) in *E. coli*, or just 50 μg/mL kanamycin (NZYTech, Portugal) in *S. oneidensis*. In both cases, microorganisms were grown to mid-exponential phase at 30°C with a shaking speed of 200 rpm. At this time, protein expression was induced with 0, 1 or 2 mM L(+)-arabinose (Acros Organics). After overnight incubation under the same conditions, the cells were harvested by centrifugation at 8000×g for 10 min at 4°C.

Table 6.1 – Oligonucleotides designed for the construction of plasmids pBAD_omcE, pBAD_omcS, pBAD_stc-omcE, pBAD_stc-OmcS, pBAD_stc-gsu2210 and pBAD_omcF-tetracysteine tag. In the forward primers omcE_FW, omcS_FW, omcF_FW and stcsp_FW a stop codon (in italic) and the ribosome binding site (in bold) were included to avoid fusion with HP-thioredoxin present in the pBAD202/D-TOPO vector® (267).

Name	Sequence 5' to 3'
pBAD_omcE	
omcE_FW	CACC*TAA***GAAGGAGATATACATCCC**ATGAGAAGCGAAGTAAAAATC
omcE_RV	CTACTTCTTGTGGCAACCCAGACAGAGCTTGC
pBAD_omcS	
omcS_FW	CACC*TAA***GAAGGAGATATACATCCC**ATGAAAAAGGGGATG
omcS_RV	TTAGTCCTTGGCGTGGCACTTGTTGCAGAG
pBAD_stc-omcE	
stcsp_FW	CACC*TAA***GAAGGAGATATACATCCC**GTGAGCAAAAAACTATTAAG
stc_omcE_RV	ATTCTTGATGCTGGCGGCAAATGCGGTTG
stc_omcE_FW	CAACCGCATTTGCCGCCAGCATCAAGAAT
omcE_RV	CTACTTCTTGTGGCAACCCAGACAGAGCTTGC
pBAD_stc-omcS	
stcsp_FW	CACC*TAA***GAAGGAGATATACATCCC**GTGAGCAAAAAACTATTAAG
stc_omcS_RV	CGCCGCCGGAGTGGAAGGCAAATGCGGTTG
stc_omcS_FW	CAACCGCATTTGCCTTCCACTCCGGCGGCG
omcS_RV	TTAGTCCTTGGCGTGGCACTTGTTGCAGAG
pBAD_stc-gsu2210	
stcsp_FW	CACC*TAA***GAAGGAGATATACATCCC**GTGAGCAAAAAACTATTAAG
stc_gsu2210_RV	TGACGATCTTGTAGTCACGGGCAAATGCGGTTGG
stc_ gsu2210_FW	CCAACCGCATTTGCCCGTGACTACAAGATCGTCA
gsu2210_med_FW	GCCACCATGGCCGACATGGGC
gsu2210_med_RV	GCCGCACGACAAGCCCTTGCC
gsu2210_RV	GTAGAGCCGCTGGTGGCACCTG
pBAD_omcF-tetracysteine tag	
omcF_FW	CACC*TAA***GAAGGAGATATACATCCC**ATGAGAGGGCTTGCCC
omcF_RV	GGCAACAGTTAAGGAATGGGAAGCTCGCCACG
tag_FW	TCACGGCTCCATACAGCAGCCCGGGCAACAGTTAAGGAATGGGAAGCTCGCCAC GAC
tag_RV	TCACGGCTCCATACAGCAGCCCGGG

BugBuster™ Protein Extraction Reagent (Novagen, USA) was used to check for expression of the proteins. The presence of the proteins was assessed by 12% SDS-PAGE with heme staining (245).

RESULTS AND DISCUSSION

Development of an expression system for GSU2210, OmcE and OmcS

In order to characterize and perform interaction studies with putative redox partners of outer membrane cytochrome OmcE, the hexaheme cytochrome OmcS and the nanowire cytochrome

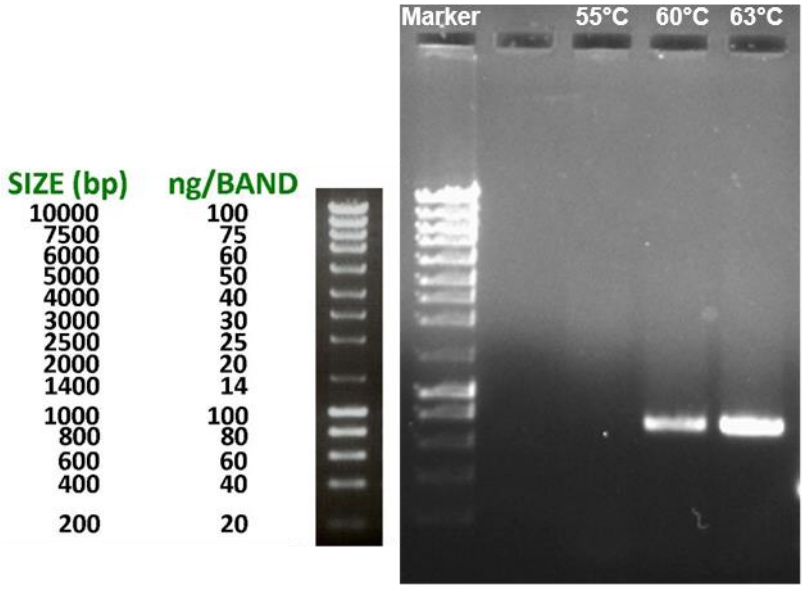

Figure 6.1 – Agarose gel with *omcE* gene PCR products obtained at different primer annealing temperatures and NZYDNA Ladder III (NZYTech) as the molecular weight marker.

GSU2210 from *G. sulfurreducens*, attempts were made to develop an expression system for the production of the proteins.

In a first step, the *omcE* and *omcS* genes were cloned from *G. sulfurreducens*. Regarding *omcE*, successful amplification of the gene with the native signal peptide was accomplished at an optimal primer annealing temperature of 63°C (Figure 6.1). Subsequently, it was inserted into plasmid pBAD202/D-TOPO® (Invitrogen). This vector is a pUC-like plasmid that is able to replicate in bacterial cells such as *E. coli* and *S. oneidensis* MR-1. It uses a highly efficient topoisomerase-based strategy for directional cloning of PCR products (308) and the expression of the genes cloned is inducible by L-arabinose (309). It also incorporates a V5-epitope and a His6 tag at the C termini of expressed proteins to facilitate subsequent protein detection and isolation. In addition, contains the His-Patch thioredoxin leader for increased translation efficiency and solubility of recombinant fusion proteins. However, in the constructions used in this work a stop codon was added to the forward PCR primers 5′ end immediately after CACC to avoid fusion with the His-Patch thioredoxin and a stop codon was added to the reverse PCR primers 3' end to prevent fusion with the His6 tag. The forward primer also contained a bacterial ribosome binding site. After expression attempts in several strains of *E. coli* (harboring the cytochrome *c* maturation gene cluster *ccmA-H*) and *S. oneidensis* MR-1 in different conditions of temperature, media, inducer concentration and periods of induction and expression, no expression was detected for the expected 24 kDa tetraheme cytochrome (Figure 6.2). Even though a band with the apparent size of OmcE was observed in the tests with *E. coli* JM109, the expression of the cytochrome was discarded, since this band is present in the profile of the *E. coli* strain when cultured in Terrific Broth medium without expression vectors (Figure 6.3).

In a second attempt, the *omcE* gene was cloned into pBAD vector without the native signal peptide. This was replaced by the signal peptide from the Small Tetraheme Cytochrome (STC) from *S. oneidensis*, which is an abundant cytochrome present in the periplasm of *S. oneidensis* cells grown anaerobically with fumarate (310).

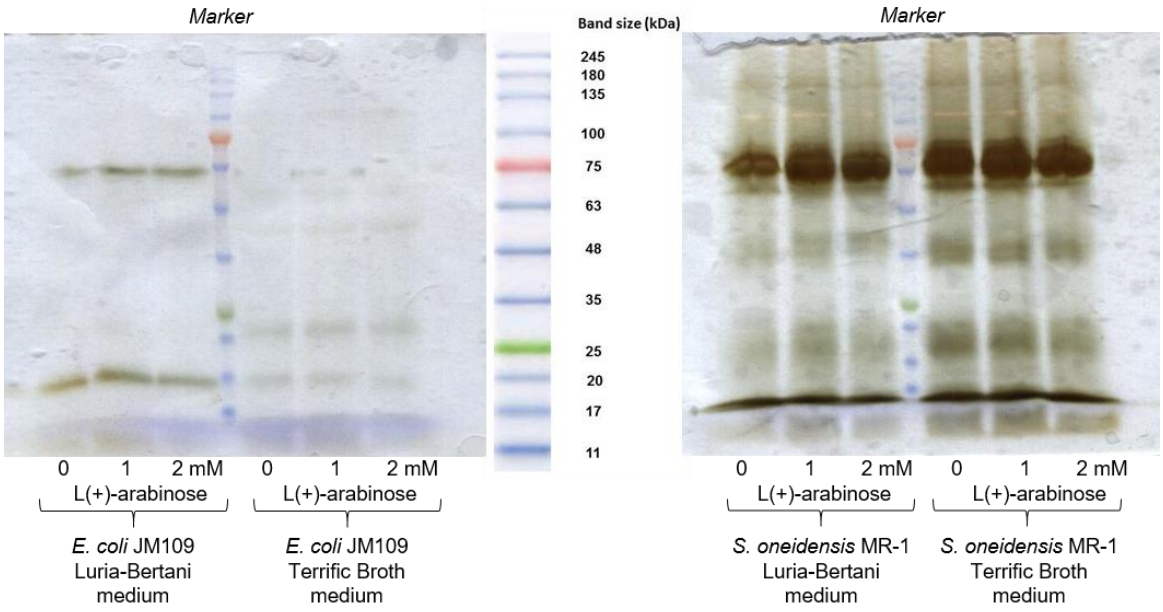

Figure 6.2 – Screening for OmcE expression in SDS-PAGE gels with NZYColour Protein Marker II (NZYTech) as a guide and heme staining. On the left, the results obtained for the expression tests with one of the *E. coli* strains used (JM109) under different media and inducer concentrations. On the right, the screening results obtained with *S. oneidensis* MR-1 under the same set of conditions.

The expression attempts showed that this construction was also not able to conduit to the expression of OmcE neither in *E. coli* nor in *S. oneidensis* strains tested under the experimental conditions applied (Figure 6.4).

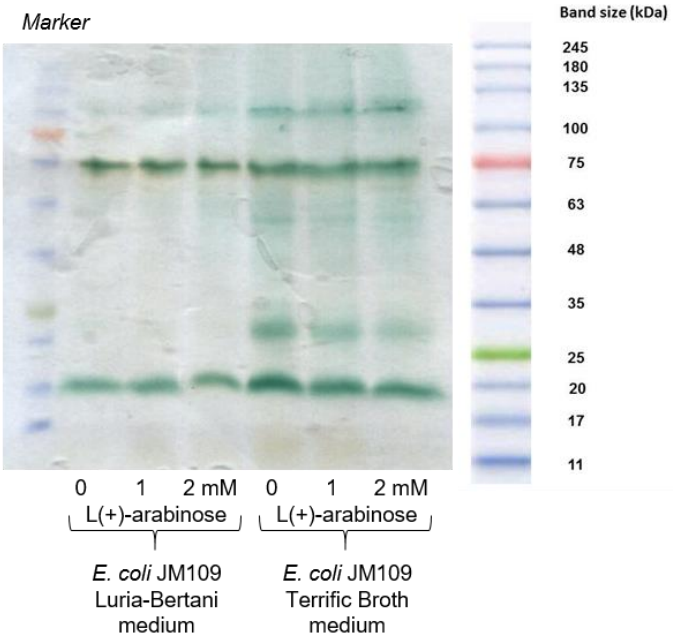

Figure 6.3 – SDS-PAGE gel stained for hemes with NZYColour Protein Marker II (NZYTech) as a guide illustrates the cytochrome *c* expression profile of *E. coli* JM109 cultured in Luria-Bertani and Terrific Broth medium in the presence and in the absence of L(+)-arabinose.

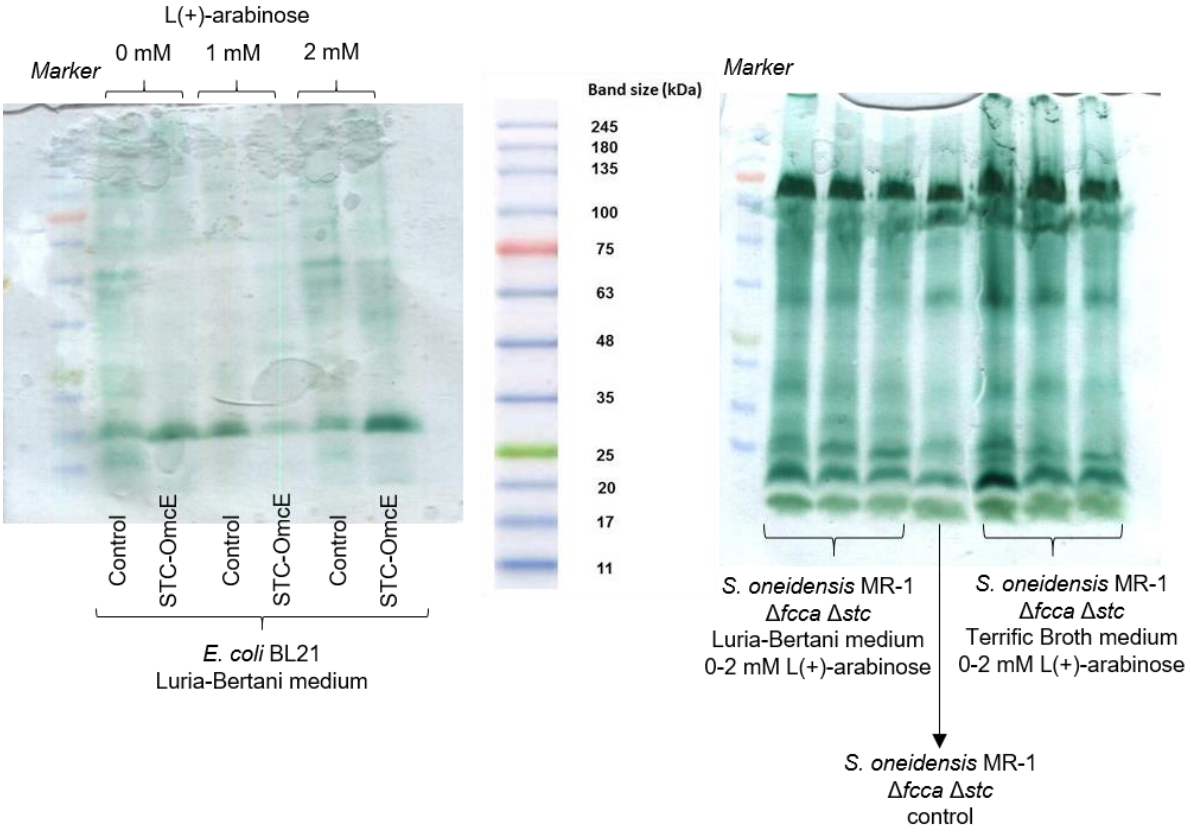

Figure 6.4 – Screening for STC-OmcE expression in SDS-PAGE gels with NZYColour Protein Marker II (NZYTech) and heme staining. On the left, the results obtained for the expression tests with *E. coli* BL21 in Luria-Bertani medium and different inducer concentrations. On the right, the screening results obtained with *S. oneidensis* MR-1 Δ*fcca* Δ*stc*. Controls refer to *E. coli* BL21 or *S. oneidensis* MR-1 Δ*fcca* Δ*stc* without the expression plasmid.

Although no heterologous expression of OmcE have been obtained so far, *E. coli* strains specifically engineered for expression of outer membrane proteins (311) may help to overcome this situation in future work.

In the case of OmcS, the cloning step had been succeeded both for the complete gene and for the gene lacking the native signal peptide with an optimal primer annealing temperature of 51.5°C (Figure 6.5). Unfortunately, the amplification step yields were very low (about 10–30 ng/µL). Nonetheless, with the small amount of PCR product obtained, the insertion of the genes in pBAD vector was attempted, although without success. Sequencing results had not confirmed the presence of neither *omcS* nor *stc-omcS* in pBAD vector.

Concerning *omcS*, gene amplification improvements may be briefly tested with the application of alternative commercially available kits that are specific for the amplification of large genes.

With respect to GSU2210, only *gsu2210* primers have been constructed as described in Table 6.1. Development of an expression system for this cytochrome will be part of forthcoming endeavors.

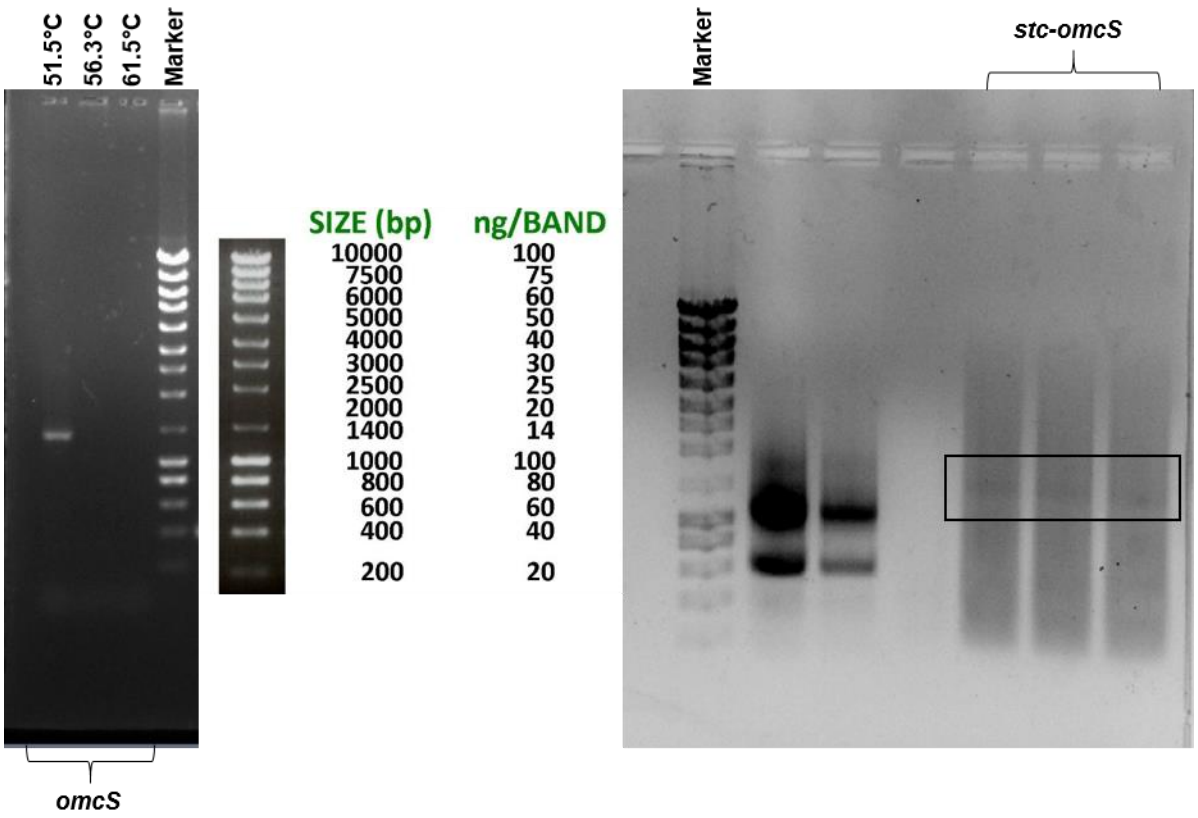

Figure 6.5 – Agarose gels with *omcS* gene PCR products obtained at different primer annealing temperatures (on the gel at the left) and *stc-omcS* PCR fusion products (boxed on the gel at the right). NZYDNA Ladder III (NZYTech) was used as molecular weight marker.

Development of a labeling system for *c*-type cytochromes

The primers forward and reverse for the complete gene were constructed, along with the one's to fuse OmcF cytochrome with the tetracysteine fluorescent tag at the C-terminal of the molecule. The fusion gene *omcF-tag* was successfully produced, as illustrated in Figure 6.6.

The fusion gene was properly inserted into pBAD and several expression attempts were performed, although none has been successful (see example in Figure 6.7).

Replacement of the native signal peptide by STC leader sequence, as explained in the Materials and Methods section of CHAPTER 5, may aid to solve the expression issues, as it was observed in the case of the expression system developed in this work for GSU1996. OmpA signal peptide is another possibility, as a successful expression system has already been described for OmcF with this leader sequence (269,312).

Unfortunately, the absence of a *c*-type tagged cytochrome constitutes the rate limiting step towards further work in the development of the proposed labeling methodology and thus, it will be addressed in upcoming efforts.

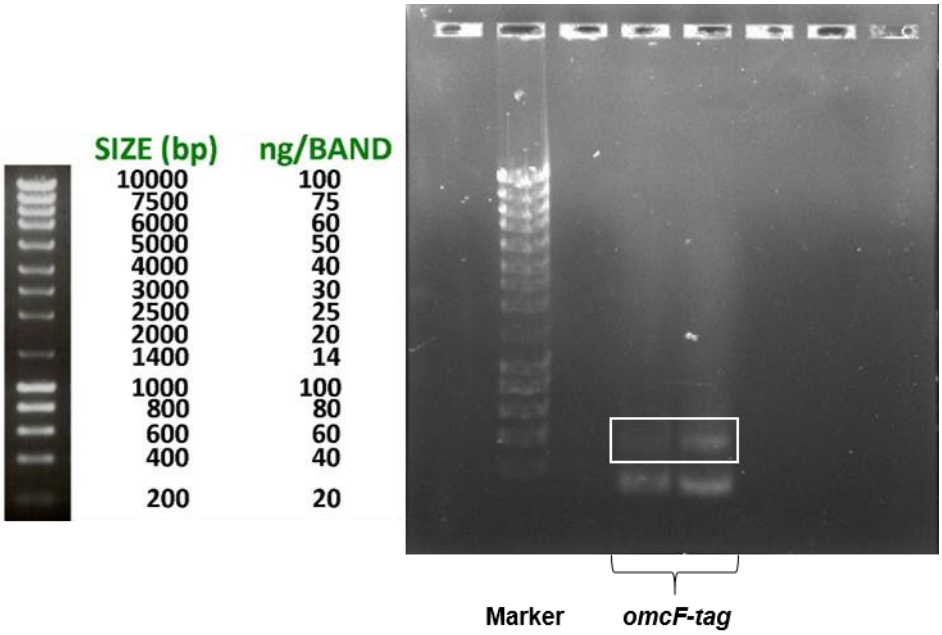

Figure 6.6 – Agarose gel with the *omcF-tag* PCR products. *omcF-tag* gene is indicated by the white box on the gel. NZYDNA Ladder III (NZYTech) was used as molecular weight marker.

CONCLUSION

Understanding of electron transfer chains of *Geobacter* bacteria is direly needed. In that sense, proteomic advances are needed towards the unveiling of electron transfer components and their roles in the cells.

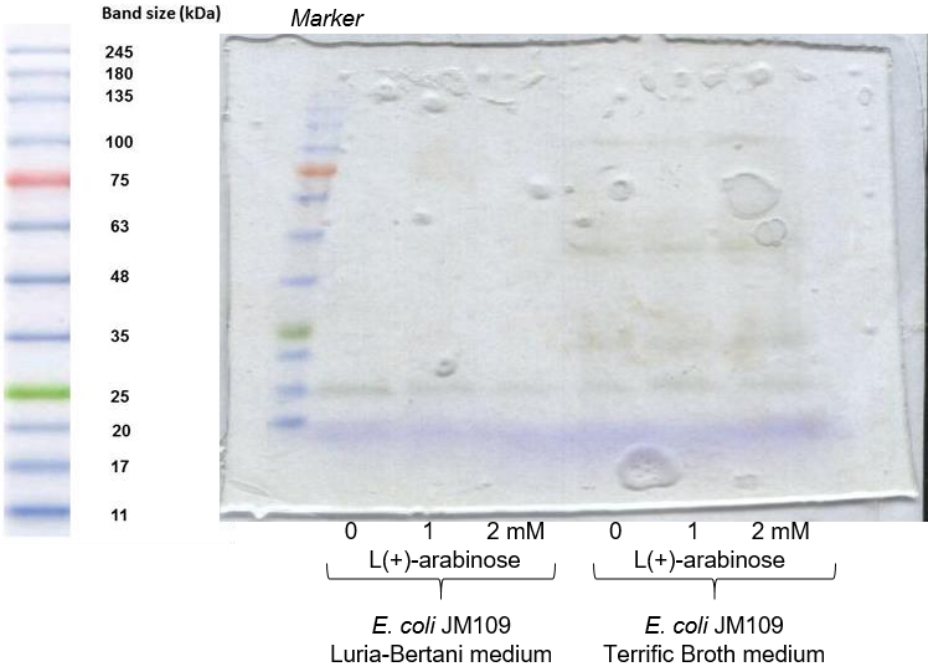

Figure 6.7 – Screening for the 9.42 kDa OmcF-tag in SDS-PAGE gel with NZYColour Protein Marker II (NZYTech) and heme staining. The results shown were obtained with expression attempts in *E. coli* JM109.

Although OmcE heterologous expression was not well accomplished so far, different expression conditions and/or hosts may correct such situation. It is also possible that homologous overexpression of OmcE in *G. sulfurreducens* may be a hypothesis for the construct of pBAD with *omcE* bearing the native signal peptide.

In the case of OmcS, application of more appropriate amplification systems may contribute to the availability of PCR products for insertion in pBAD vector so as to move forward to the expression tests.

As to GSU2210, primers are already available for the appropriate cloning and insertion in pBAD vector.

Finally, the *in vivo c*-type cytochrome labeling system has been hindered by the lack of a tagged protein. Nonetheless, a simple change in the leader sequence of the construct may solve this situation and enable future developments of this work.

CHAPTER 7

CONCLUDING REMARKS AND FUTURE PERSPECTIVES

Contents

FINAL CONCLUSIONS

Macroscopic biological systems comprehension is far from providing the crucial answers that are required to boost biotechnological advances to the next level. Indeed, groundwork in molecular mechanisms such as electron transfer is needed without delay, as it will contribute to a more integrated understanding of the biogeochemical cycles of the elements on Earth, and also to the development of novel and enhanced biotechnological tools that cover a vast spectra (5,15). Examples go from bioenergy production (18,301,313), to bioremediation of contaminated environments (314–316) and recovery of added-value compounds, or to the development of new biocatalysts (33,89). Therefore, mechanistic comprehension of electron transfer performed by highly versatile and efficient microorganisms may allow major breakthroughs in the scaling-up of MXCs and in the creation and improvement of biomimetic applications (5,15).

An atypical high number of multiheme *c*-type cytochromes are expressed in several microorganisms, such as *Geobacter* spp. (134,179,235), and these have been enrolled in electron transfer mechanisms that allow these bacteria to thrive successfully in so many environments, even under nutrient deprivation and other stress conditions (107,118). Multiheme *c*-type cytochromes mechanistic understanding is still in its early stages, as the complexity involved in their study raises impressively with the increase in molecular weight and number of hemes, and methodologies in use are not up to the challenges presented by these proteins. Indeed, the problems arise from the start, in the step of obtaining the cytochromes. Isolation of a specific cytochrome from organisms with such a high profusion of *c*-type cytochromes is an impossible task in most of the cases. Therefore, one way to solve this issue is to develop heterologous expression systems for the desired proteins. Although several methodologies have been reported (267,269,274,317), each cytochrome presents new and puzzling time-consuming challenges until the proper expression is achieved. While overexpression is the goal, usually, only small expression extension is accomplished. Next, purification steps need to be optimized and stability conditions established, so as to preserve the cytochrome in a properly folded functional state for as long as it is possible. Afterwards, materials and methodologies that allow the acquisition of the required data for the unveiling of mechanistic information need to be upgraded and/or created. Finally, data analysis can be defying with the increase in the number and idiosyncrasies of the hemes. Altogether, this translates in thousands of euros investment, dozens of liters of culture growth and in weeks, months or even years to develop an expression system, produce and purify the required amount of proteins needed to perform the also laborious studies that provide the underlying structural and functional details. For these reasons, large multiheme *c*-type cytochromes are still eagerly waiting to be uncovered.

This work focused on the study of an electron transfer protein from *G. sulfurreducens*, the dodecaheme nanowire cytochrome GSU1996. In order to overcome the obstacles inherent to the characterization of a protein with such large size and number of hemes, a puzzle approach, based in its modular structure was validated. Consequently, the functional characterization of individual triheme domains C and D was used to assist in the characterization of the C-terminal end of GSU1996, the hexaheme fragment CD. The same was tested for the N-terminal end of GSU1996, the hexaheme

fragment AB. Although this fragment has been properly produced, the presence of more than one form of domain A in solution and the absence of domain B hindered further work with this side of the biomolecule. Nonetheless, it was observed that the thermodynamic and kinetic properties of fragment CD are suitable to promote the entrance of electrons in GSU1996 via heme III of domain D.

Interaction studies between GSU1996 and putative interacting partners – PpcA to E – revealed that a transient redox interaction occurs amid GSU1996 and PpcA. Experiments performed with fragment AB and fragment CD showed that the complex formation involves the C-terminal of GSU1996 and heme IV of PpcA. This is in agreement with the structural features of GSU1996, given that the domains C and D are connected by a flexible linker and appear to have higher degree of mobility than the domains A and B in the N-terminal.

Overall, data collected indicates that GSU1996 works as a nanowire device and it was proposed to be an electron storage unit in periods of cellular starvation, to withstand survival. In light of the reversibility of the electron flow between GSU1996 and PpcA, it is possible that electrons stored in GSU1996 may be latter used to reduce electron acceptors as they become available again in the environmental surroundings. Probably, such interaction is triggered in the course of a reaction to environmental parameters change, via a specific signaling mechanism that benefits the interaction between the nanowire cytochrome and PpcA instead of the electron transfer to external electron acceptors.

The characterization methodology followed with GSU1996 has proven its value towards the study of large size *c*-type cytochromes, provided that the structural features allow this puzzle approach without loss of identity in the individual pieces.

FUTURE WORK

Although some issues have been successfully addressed in this PhD on the road to understand the nanowire cytochrome GSU1996, several others remain to be answered. In that sense, the N-terminal end of the molecule requires further studies in order to complete the GSU1996 functional puzzle. Based in the heterologous expression system developed by Dr. Yuri Y. Londer, expression yields of domain A had already been optimized in previous efforts (221). Unfortunately, this work revealed the coexistence of different conformations in solution. It was reported that periplasmic protein stability may rely upon their C-terminal residues (318). Therefore, a different expression system that includes an alternative gene coding sequence must be envisioned with the aim to produce a more stable solution form of the domain A, so as to allow the proper thermodynamic and kinetic characterization. In what concerns to domain B, attempts performed earlier failed to improve expression yields and purification (221) of the expression system established by Dr. Yuri Y. Londer. As in the case of domain A, other heterologous system need to be addressed. Regarding the achievement in the expression of GSU1996 and its fragment AB, one hypothesis in both cases may be the modification of the constructs proposed in this PhD to produce domain A and domain B.

The *in vivo* labeling of *c*-type cytochromes has also been hindered by the absence of a tagged protein. As referred in CHAPTER 6, the change of the leader sequence in the construct may solve this issue and allow further advances to validate the proposed methodology.

With respect to other electron transfer components, and as discussed in CHAPTER 6, OmcE heterologous expression may be tested in microorganisms more suitable for expression of outer membrane proteins, as some engineered *E. coli* strains (311). In the case of OmcS, the yields in the amplification of the genes for posterior insertion in pBAD vector may be accomplished with the use of commercially available kits, targeted for the amplification of larger genes. Finally, GSU2210 primers have been constructed and will be the object of expression tests briefly.

REFERENCES

1. Glick BR, Pasternak JJ, Patten CL. Molecular biotechnology: principles and applications of recombinant DNA. Washington, DC: ASM Press; 2010.
2. Madsen EL. Environmental microbiology: from genomes to biogeochemistry. Malden MA: Blackwell Publishing; 2008.
3. Singh RL. Introduction to Environmental Biotechnology. In: Principles and Applications of Environmental Biotechnology for a Sustainable Future. Singapore: Springer Singapore; 2017. p. 1–12.
4. Bashkin VN, Howarth RW. Modern biogeochemistry. Dordrecht: Kluwer Academic Publishers; 2002.
5. Madsen EL. Microorganisms and their roles in fundamental biogeochemical cycles. Curr Opin Biotechnol. 2011;22(3):456–64.
6. Shi L, Dong H, Reguera G, Beyenal H, Lu A, Liu J, et al. Extracellular electron transfer mechanisms between microorganisms and minerals. Nat Rev Microbiol. 2016;14(10):651–62.
7. Rawlings DE, Dew D, du Plessis C. Biomineralization of metal-containing ores and concentrates. Trends Biotechnol. 2003;21(1):38–44.
8. Johnson DB. Biomining – biotechnologies for extracting and recovering metals from ores and waste materials. Curr Opin Biotechnol. 2014;30:24–31.
9. Lovley DR, Stolz JF, Nord GL, Phillips EJP. Anaerobic production of magnetite by a dissimilatory iron-reducing microorganism. Nature. 1987;330(6145):252–4.
10. Windt W de, Aelterman P, Verstraete W. Bioreductive deposition of palladium (0) nanoparticles on *Shewanella oneidensis* with catalytic activity towards reductive dechlorination of polychlorinated biphenyls. Environ Microbiol. 2005;7(3):314–25.
11. Pearce CI, Pattrick RAD, Law N, Charnock JM, Coker VS, Fellowes JW, et al. Investigating different mechanisms for biogenic selenite transformations: *Geobacter sulfurreducens*, *Shewanella oneidensis* and *Veillonella atypica*. Environ Technol. 2009;30(12):1313–26.
12. Dippon U, Pantke C, Porsch K, Larese-Casanova P, Kappler A. Potential function of added minerals as nucleation sites and effect of humic substances on mineral formation by the nitrate-reducing Fe(II)-oxidizer *Acidovorax* sp. BoFeN1. Environ Sci Technol. 2012;46(12):6556–65.
13. Byrne JM, Coker VS, Moise S, Wincott PL, Vaughan DJ, Tuna F, et al. Controlled cobalt doping in biogenic magnetite nanoparticles. J R Soc Interface. 2013;10(83):20130134.
14. Bond DR, Lovley DR. Electricity production by *Geobacter sulfurreducens* attached to electrodes. Appl Environ Microbiol. 2003;69(3):1548–55.
15. Rabaey K, Rozendal RA. Microbial electrosynthesis – revisiting the electrical route for microbial production. Nat Rev Microbiol. 2010;8(10):706–16.
16. Logan BE. Exoelectrogenic bacteria that power microbial fuel cells. Nat Rev Microbiol. 2009;7(5):375–81.
17. Bretschger O, Obraztsova A, Sturm CA, Chang IS, Gorby YA, Reed SB, et al. Current production and metal oxide reduction by *Shewanella oneidensis* MR-1 wild type and mutants. Appl Environ

Microbiol. 2007;73(21):7003–12.
18. Tender LM, Gray SA, Groveman E, Lowy DA, Kauffman P, Melhado J, et al. The first demonstration of a microbial fuel cell as a viable power supply: powering a meteorological buoy. J Power Sources. 2008;179(2):571–5.
19. Wu S, Li H, Zhou X, Liang P, Zhang X, Jiang Y, et al. A novel pilot-scale stacked microbial fuel cell for efficient electricity generation and wastewater treatment. Water Res. 2016;98:396–403.
20. He W, Zhang X, Liu J, Zhu X, Feng Y, Logan BE. Microbial fuel cells with an integrated spacer and separate anode and cathode modules. Environ Sci Water Res Technol. 2016;2(1):186–95.
21. Dekker A, Heijne A Ter, Saakes M, Hamelers HVM, Buisman CJN. Analysis and improvement of a scaled-up and stacked microbial fuel cell. Environ Sci Technol. 2009;43(23):9038–42.
22. Kato S, Hashimoto K, Watanabe K. Methanogenesis facilitated by electric syntrophy via (semi)conductive iron-oxide minerals. Environ Microbiol. 2012;14(7):1646–54.
23. Rotaru AE, Shrestha PM, Liu F, Markovaite B, Chen S, Nevin KP, et al. Direct interspecies electron transfer between *Geobacter metallireducens* and *Methanosarcina barkeri*. Appl Environ Microbiol. 2014;80(15):4599–605.
24. Kumar R, Singh L, Zularisam AW. Exoelectrogens: recent advances in molecular drivers involved in extracellular electron transfer and strategies used to improve it for microbial fuel cell applications. Renew Sustain Energy Rev. 2016;56:1322–36.
25. Geelhoed JS, Stams AJM. Electricity-assisted biological hydrogen production from acetate by *Geobacter sulfurreducens*. Environ Sci Technol. 2011;45(2):815–20.
26. Lovley DR, Ueki T, Zhang T, Malvankar NS, Shrestha PM, Flanagan KA, et al. *Geobacter*: the microbe electric's physiology, ecology, and practical applications. Vol. 59, Advances in Microbial Physiology. 2011. 1–100 p.
27. Hauser CAE, Zhang S. Nanotechnology: peptides as biological semiconductors. Nature. 2010;468(7323):516–7.
28. Izallalen M, Mahadevan R, Burgard A, Postier B, Didonato R, Sun J, et al. *Geobacter sulfurreducens* strain engineered for increased rates of respiration. Metab Eng. 2008;10(5):267–75.
29. Yi H, Nevin KP, Kim B-C, Franks AE, Klimes A, Tender LM, et al. Selection of a variant of *Geobacter sulfurreducens* with enhanced capacity for current production in microbial fuel cells. Biosens Bioelectron. 2009;24(12):3498–503.
30. Flynn JM, Ross DE, Hunt KA, Bond DR, Gralnick JA. Enabling unbalanced fermentations by using engineered electrode-interfaced bacteria. MBio. 2010;1(5).
31. Nevin KP, Woodard TL, Franks AE, Summers ZM, Lovley DR. Microbial electrosynthesis: feeding microbes electricity to convert carbon dioxide and water to multicarbon extracellular organic compounds. MBio. 2010;1(2):e00103-10.
32. Park DH, Laivenieks M, Guettler M V., Jain MK, Zeikus JG. Microbial utilization of electrically reduced neutral red as the sole electron donor for growth and metabolite production. Appl Environ Microbiol. 1999;65(7):2912–7.
33. Lloyd JR. Dissimilatory metal transformations by microorganisms. In: Encyclopedia of Life

Sciences. Chichester, UK: John Wiley & Sons, Ltd; 2005.
34. Lovley DR. Dissimilatory metal reduction. Annu Rev Microbiol. 1993;47(1):263–90.
35. Lovley DR, Anderson RT. Influence of dissimilatory metal reduction on fate of organic and metal contaminants in the subsurface. Hydrogeol J. 2000;8(1):77–88.
36. Lloyd JR. Microbial reduction of metals and radionuclides. FEMS Microbiol Rev. 2003;27(2–3):411–25.
37. Ilbert M, Bonnefoy V. Insight into the evolution of the iron oxidation pathways. Biochim Biophys Acta - Bioenerg. 2013;1827(2):161–75.
38. Andrews SC, Robinson AK, Rodríguez-Quiñones F. Bacterial iron homeostasis. FEMS Microbiol Rev. 2003;27(2–3):215–37.
39. Beinert H, Holm RH, Münck E. Iron-sulfur clusters: nature's modular, multipurpose structures. Science (80-). 1997;277(5326):653–9.
40. Lovley DR. Dissimilatory Fe(III) and Mn(IV) reduction. Microbiol Rev. 1991;55(2):259–87.
41. Lovley DR. Organic matter mineralization with the reduction of ferric iron: a review. Geomicrobiol J. 1987;5(3–4):375–99.
42. Fischer WR. Microbiological reactions of Iron in soils. In: Iron in Soils and Clay Minerals. Dordrecht: Springer Netherlands; 1988. p. 715–48.
43. Lovley DR, Giovannoni SJ, White DC, Champine JE, Phillips EJ, Gorby YA, et al. *Geobacter metallireducens* gen. nov. sp. nov., a microorganism capable of coupling the complete oxidation of organic compounds to the reduction of iron and other metals. Arch Microbiol. 1993;159(4):336–44.
44. Roden EE, Lovley DR. Dissimilatory Fe(III) reduction by the marine microorganism *Desulfuromonas acetoxidans*. Appl Environ Microbiol. 1993;59(3):734–42.
45. Myers CR, Nealson KH. Bacterial manganese reduction and growth with manganese oxide as the sole electron acceptor. Science (80-). 1988;240(4857):1319–21.
46. Lovley DR. Cleaning up with genomics: applying molecular biology to bioremediation. Nat Rev Microbiol. 2003;1(1):35–44.
47. Lovley DR, Baedecker MJ, Lonergan DJ, Cozzarelli IM, Phillips EJP, Siegel DI. Oxidation of aromatic contaminants coupled to microbial iron reduction. Nature. 1989;339(6222):297–300.
48. Aulenta F, Rossetti S, Amalfitano S, Majone M, Tandoi V. Conductive magnetite nanoparticles accelerate the microbial reductive dechlorination of trichloroethene by promoting interspecies electron transfer processes. ChemSusChem. 2013;6(3):433–6.
49. Sekar R, DiChristina TJ. Microbially driven Fenton reaction for degradation of the widespread environmental contaminant 1,4-Dioxane. Environ Sci Technol. 2014;48(21):12858–67.
50. Thamdrup B. Bacterial manganese and iron reduction in aquatic sediments. In: Schink B, editor. Advances in Microbial Ecology. Boston, MA: Springer; 2000. p. 41–81.
51. Lovley DR, Phillips EJP. Manganese inhibition of microbial iron reduction in anaerobic sediments. Geomicrobiol J. 1988;6(3–4):145–55.
52. Lovley DR, Phillips EJP, Gorby YA, Landa ER. Microbial reduction of uranium. Nature. 1991;350(6317):413–6.

53. Gorby YA, Lovley DR. Enzymic uranium precipitation. Environ Sci Technol. 1992;26(1):205–7.
54. Newsome L, Morris K, Lloyd JR. The biogeochemistry and bioremediation of uranium and other priority radionuclides. Chem Geol. 2014;363:164–84.
55. Langmuir D. Uranium solution-mineral equilibria at low temperatures with applications to sedimentary ore deposits. Geochim Cosmochim Acta. 1978;42(6):547–69.
56. Lovley DR, Phillips EJ. Reduction of uranium by *Desulfovibrio desulfuricans*. Appl Environ Microbiol. 1992;58(3):850–6.
57. Cologgi DL, Lampa-Pastirk S, Speers AM, Kelly SD, Reguera G. Extracellular reduction of uranium via *Geobacter* conductive pili as a protective cellular mechanism. Proc Natl Acad Sci. 2011;108(37):15248–52.
58. Sheng L, Fein JB. Uranium reduction by *Shewanella oneidensis* MR-1 as a function of $NaHCO_3$ concentration: surface complexation control of reduction kinetics. Environ Sci Technol. 2014;48(7):3768–75.
59. Stylo M, Neubert N, Roebbert Y, Weyer S, Bernier-Latmani R. Mechanism of uranium reduction and immobilization in *Desulfovibrio vulgaris* biofilms. Environ Sci Technol. 2015;49(17):10553–61.
60. Payne RB, Gentry DM, Rapp-Giles BJ, Casalot L, Wall JD. Uranium reduction by *Desulfovibrio desulfuricans* strain G20 and a cytochrome c_3 mutant. Appl Environ Microbiol. 2002;68(6):3129–32.
61. Lovley DR. Bioremediation of organic and metal contaminants with dissimilatory metal reduction. J Ind Microbiol. 1995;14(2):85–93.
62. Lloyd JR, Yong P, Macaskie LE. Biological reduction and removal of Np(V) by two microorganisms. Environ Sci Technol. 2000;34(7):1297–301.
63. Rusin PA, Quintana L, Brainard JR, Strietelmeier BA, Tait CD, Ekberg SA, et al. Solubilization of plutonium hydrous oxide by iron-reducing bacteria. Environ Sci Technol. 1994;28(9):1686–90.
64. Lloyd JR, Cole JA, Macaskie LE. Reduction and removal of heptavalent technetium from solution by *Escherichia coli*. J Bacteriol. 1997;179(6):2014–21.
65. Lloyd JR, Sole VA, van Praagh C V., Lovley DR. Direct and Fe(II)-mediated reduction of technetium by Fe(III)-reducing bacteria. Appl Environ Microbiol. 2000;66(9):3743–9.
66. De Luca G, de Philip P, Dermoun Z, Rousset M, Verméglio A. Reduction of technetium(VII) by *Desulfovibrio fructosovorans* is mediated by the nickel-iron hydrogenase. Appl Environ Microbiol. 2001;67(10):4583–7.
67. Maillard J-Y, Hartemann P. Silver as an antimicrobial: facts and gaps in knowledge. Crit Rev Microbiol. 2013;39(4):373–83.
68. Fu JK, Liu YY, Gu PY, Tang DL, Lin ZY, Yao BX, et al. Spectroscopic characterization on the biosorption and bioreduction of Ag (I) by *Lactobacillus* sp. A09. Vol. 16, Acta Physico - Chimica Sinica. 2000. 781–782 p.
69. Barkay T, Miller SM, Summers AO. Bacterial mercury resistance from atoms to ecosystems. FEMS Microbiol Rev. 2003;27(2–3):355–84.

70. Iwahori K, Takeuchi F, Kamimura K, Sugio T. Ferrous iron-dependent volatilization of mercury by the plasma membrane of *Thiobacillus ferrooxidans*. Appl Environ Microbiol. 2000;66(9):3823–7.
71. Caccavo F, Lonergan DJ, Lovley DR, Davis M, Stolz JF, McInerney MJ. *Geobacter sulfurreducens* sp. nov., a hydrogen- and acetate-oxidizing dissimilatory metal-reducing microorganism. Appl Environ Microbiol. 1994;60(10):3752–9.
72. Wang Y-T. Microbial reduction of chromate. In: Lovley DR, editor. Environmental Microbe-Metal Interactions. Washington, DC: American Society of Microbiology; 2000. p. 225–35.
73. Shen H, Wang YT. Simultaneous chromium reduction and phenol degradation in a coculture of *Escherichia coli* ATCC 33456 and *Pseudomonas putida* DMP-1. Appl Environ Microbiol. 1995;61(7):2754–8.
74. Suzuki T, Miyata N, Horitsu H, Kawai K, Takamizawa K, Tai Y, et al. NAD(P)H-dependent chromium(VI) reductase of *Pseudomonas ambigua* G-1: a Cr(V) intermediate is formed during the reduction of Cr(VI) to Cr(III). J Bacteriol. 1992;174(16):5340–5.
75. Park CH, Keyhan M, Wielinga B, Fendorf S, Matin A. Purification to homogeneity and characterization of a novel *Pseudomonas putida* chromate reductase. Appl Environ Microbiol. 2000;66(5):1788–95.
76. Myers CR, Carstens BP, Antholine WE, Myers JM. Chromium(VI) reductase activity is associated with the cytoplasmic membrane of anaerobically grown *Shewanella putrefaciens* MR-1. J Appl Microbiol. 2000;88(1):98–106.
77. Lovley DR, Phillips EJ. Reduction of chromate by *Desulfovibrio vulgaris* and its c_3 cytochrome. Appl Environ Microbiol. 1994;60(2):726–8.
78. Wang PC, Mori T, Komori K, Sasatsu M, Toda K, Ohtake H. Isolation and characterization of an *Enterobacter cloacae* strain that reduces hexavalent chromium under anaerobic conditions. Appl Environ Microbiol. 1989;55(7):1665–9.
79. Shen H, Wang YT. Characterization of enzymatic reduction of hexavalent chromium by *Escherichia coli* ATCC 33456. Appl Environ Microbiol. 1993;59(11):3771–7.
80. Kashefi K, Tor JM, Nevin KP, Lovley DR. Reductive precipitation of gold by dissimilatory Fe(III)-reducing *Bacteria* and *Archaea*. Appl Environ Microbiol. 2001;67(7):3275–9.
81. Bautista EM, Alexander M. Reduction of inorganic compounds by soil microorganisms. Soil Sci Soc Am J. 1972;36(6):918.
82. Ortiz-Bernad I, Anderson RT, Vrionis HA, Lovley DR. Vanadium respiration by *Geobacter metallireducens*: novel strategy for in situ removal of vanadium from groundwater. Appl Environ Microbiol. 2004;70(5):3091–5.
83. Yurkova NA, Lyalikova NN. New vanadate-reducing facultative chemolithotrophic bacteria. Microbiology. 1991;59:672–7.
84. Hofmann BA. Reduction spheroids from northern Switzerland: mineralogy, geochemistry and genetic models. Chem Geol. 1990;81(1–2):55–81.
85. Bertine KK. The deposition of molybdenum in anoxic waters. Mar Chem. 1972;1(1):43–53.
86. Brierley CL, Brierley JA. Anaerobic reduction of molybdenum by *Sulfolobus* species. Zentralblatt

für Bakteriol Mikrobiol und Hyg I Abt Orig C Allg Angew und ökologische Mikrobiol. 1982;3(2):289–94.

87. Sugio T, Tsujita Y, Katagiri T, Inagaki K, Tano T. Reduction of Mo^{6+} with elemental sulfur by *Thiobacillus ferrooxidans*. J Bacteriol. 1988;170(12):5956–9.
88. Lloyd JR, Yong P, Macaskie LE. Enzymatic recovery of elemental palladium by using sulfate-reducing bacteria. Appl Environ Microbiol. 1998;64(11):4607–9.
89. Yong P, Farr JPG, Harris IR, Macaskie LE. Palladium recovery by immobilized cells of *Desulfovibrio desulfuricans* using hydrogen as the electron donor in a novel electrobioreactor. Biotechnol Lett. 2002;24(3):205–12.
90. Oremland RS, Stolz JF. The ecology of arsenic. Science (80-). 2003;300(5621):939–44.
91. Islam FS, Pederick RL, Gault AG, Adams LK, Polya DA, Charnock JM, et al. Interactions between the Fe(III)-reducing bacterium *Geobacter sulfurreducens* and arsenate, and capture of the metalloid by biogenic Fe(II). Appl Environ Microbiol. 2005;71(12):8642–8.
92. Dang Y, Walker DJF, Vautour KE, Dixon S, Holmes DE. Arsenic detoxification by *Geobacter* species. Appl Environ Microbiol. 2017;83(4):e02689-16.
93. Macy JM, Nunan K, Hagen KD, Dixon DR, Harbour PJ, Cahill M, et al. *Chrysiogenes arsenatis* gen. nov., sp. nov., a new arsenate-respiring bacterium isolated from gold mine wastewater. Int J Syst Bacteriol. 1996;46(4):1153–7.
94. Stolz JF, Ellis DJ, Blum JS, Ahmann D, Lovley DR, Oremland RS. *Sulfurospirillum barnesii* sp. nov. and *Sulfurospirillum arsenophilum* sp. nov., new members of the *Sulfurospirillum* clade of the epsilon *Proteobacteria*. Int J Syst Bacteriol. 1999;49(3):1177–80.
95. Krafft T, Macy JM. Purification and characterization of the respiratory arsenate reductase of *Chrysiogenes arsenatis*. Eur J Biochem. 1998;255(3):647–53.
96. Stüeken EE, Buick R, Bekker A, Catling D, Foriel J, Guy BM, et al. The evolution of the global selenium cycle: secular trends in Se isotopes and abundances. Geochim Cosmochim Acta. 2015;162:109–25.
97. Schröder I, Rech S, Krafft T, Macy JM. Purification and characterization of the selenate reductase from *Thauera selenatis*. J Biol Chem. 1997;272(38):23765–8.
98. Avazéri C, Turner RJ, Pommier J, Weiner JH, Giordano G, Verméglio A. Tellurite reductase activity of nitrate reductase is responsible for the basal resistance of *Escherichia coli* to tellurite. Microbiology. 1997;143(4):1181–9.
99. Shi L, Squier TC, Zachara JM, Fredrickson JK. Respiration of metal (hydr)oxides by *Shewanella* and *Geobacter*: a key role for multihaem *c*-type cytochromes. Mol Microbiol. 2007;65(1):12–20.
100. Albers S-V, Meyer BH. The archaeal cell envelope. Nat Rev Microbiol. 2011;9(6):414–26.
101. White GF, Edwards MJ, Gomez-Perez L, Richardson DJ, Butt JN, Clarke TA. Mechanisms of bacterial extracellular electron exchange. 1st ed. Advances in Microbial Physiology. Elsevier Ltd.; 2016. 87–138 p.
102. Nealson KH, Belz A, McKee B. Breathing metals as a way of life: geobiology in action. Antonie Van Leeuwenhoek. 2002;81(1/4):215–22.
103. Nevin KP, Lovley DR. Mechanisms for accessing insoluble Fe(III) oxide during dissimilatory

Fe(III) reduction by *Geothrix fermentans*. Appl Environ Microbiol. 2002;68(5):2294–9.

104. Hernandez ME, Newman DK. Extracellular electron transfer. Cell Mol Life Sci. 2001;58(11):1562–71.
105. Butler JE, Young ND, Lovley DR. Evolution of electron transfer out of the cell: comparative genomics of six *Geobacter* genomes. BMC Genomics. 2010;11:40.
106. Coppi M V., Leang C, Sandler SJ, Lovley DR. Development of a genetic system for *Geobacter sulfurreducens*. Appl Environ Microbiol. 2001;67(7):3180–7.
107. Esteve-Núñez A, Rothermich M, Sharma M, Lovley D. Growth of *Geobacter sulfurreducens* under nutrient-limiting conditions in continuous culture. Environ Microbiol. 2005;7(5):641–8.
108. Wang L-Y, Nevin KP, Woodard TL, Mu B-Z, Lovley DR. Expanding the diet for DIET: electron donors supporting Direct Interspecies Electron Transfer (DIET) in defined co-cultures. Front Microbiol. 2016;7:236.
109. Kim B-C, Leang C, Ding Y-HR, Glaven RH, Coppi M V., Lovley DR. OmcF, a putative *c*-type monoheme outer membrane cytochrome required for the expression of other outer membrane cytochromes in *Geobacter sulfurreducens*. J Bacteriol. 2005;187(13):4505–13.
110. Lovley DR. Dissimilatory Fe(III)- and Mn(IV)-reducing prokaryotes. In: The Prokaryotes. New York: Springer New York; 2006. p. 635–58.
111. Lovley DR. Extracellular electron transfer: wires, capacitors, iron lungs, and more. Geobiology. 2008;6(3):225–31.
112. Lovley DR, Holmes DE, Nevin KP. Dissimilatory Fe(III) and Mn(IV) reduction. Adv Microb Physiol. 2004;49(2):219–86.
113. Childers SE, Ciufo S, Lovley DR. *Geobacter metallireducens* accesses insoluble Fe(III) oxide by chemotaxis. Nature. 2002;416(6882):767–9.
114. Risso C, Methé BA, Elifantz H, Holmes DE, Lovley DR. Highly conserved genes in *Geobacter* species with expression patterns indicative of acetate limitation. Microbiology. 2008;154(9):2589–99.
115. Zhuang K, Izallalen M, Mouser P, Richter H, Risso C, Mahadevan R, et al. Genome-scale dynamic modeling of the competition between *Rhodoferax* and *Geobacter* in anoxic subsurface environments. ISME J. 2011;5(2):305–16.
116. Lin B, Westerhoff H V., Röling WFM. How *Geobacteraceae* may dominate subsurface biodegradation: physiology of *Geobacter metallireducens* in slow-growth habitat-simulating retentostats. Environ Microbiol. 2009;11(9):2425–33.
117. Esteve-Núñez A, Sosnik J, Visconti P, Lovley DR. Fluorescent properties of *c*-type cytochromes reveal their potential role as an extracytoplasmic electron sink in *Geobacter sulfurreducens*. Environ Microbiol. 2008;10(2):497–505.
118. Malvankar NS, Mester T, Tuominen MT, Lovley DR. Supercapacitors based on *c*-type cytochromes using conductive nanostructured networks of living bacteria. ChemPhysChem. 2012;13(2):463–8.
119. Ueki T, Lovley DR. Novel regulatory cascades controlling expression of nitrogen-fixation genes in *Geobacter sulfurreducens*. Nucleic Acids Res. 2010;38(21):7485–99.

120. Lin WC, Coppi M V., Lovley DR. *Geobacter sulfurreducens* can grow with oxygen as a terminal electron acceptor. Appl Environ Microbiol. 2004;70(4):2525–8.
121. Summers ZM, Fogarty HE, Leang C, Franks AE, Malvankar NS, Lovley DR. Direct exchange of electrons within aggregates of an evolved syntrophic coculture of anaerobic bacteria. Science (80-). 2010;330(6009):1413–5.
122. Kouzuma A, Kato S, Watanabe K. Microbial interspecies interactions: recent findings in syntrophic consortia. Front Microbiol. 2015;6:477.
123. Shelobolina ES, Nevin KP, Blakeney-Hayward JD, Johnsen C V., Plaia TW, Krader P, et al. *Geobacter pickeringii* sp. nov., *Geobacter argillaceus* sp. nov. and *Pelosinus fermentans* gen. nov., sp. nov., isolated from subsurface kaolin lenses. Int J Syst Evol Microbiol. 2007;57(1):126–35.
124. Nevin KP, Holmes DE, Woodard TL, Hinlein ES, Ostendorf DW, Lovley DR. *Geobacter bemidjiensis* sp. nov. and *Geobacter psychrophilus* sp. nov., two novel Fe(III)-reducing subsurface isolates. Int J Syst Evol Microbiol. 2005;55(4):1667–74.
125. Straub KL, Buchholz-Cleven B. *Geobacter bremensis* sp. nov. and *Geobacter pelophilus* sp. nov., two dissimilatory ferric-iron-reducing bacteria. Int J Syst Evol Microbiol. 2001;51(5):1805–8.
126. Coates JD, Bhupathiraju VK, Achenbach LA, Mclnerney MJ, Lovley DR. *Geobacter hydrogenophilus*, *Geobacter chapellei* and *Geobacter grbiciae*, three new, strictly anaerobic, dissimilatory Fe(III)-reducers. Int J Syst Evol Microbiol. 2001;51(Pt 2):581–8.
127. Prakash O, Gihring TM, Dalton DD, Chin K-J, Green SJ, Akob DM, et al. *Geobacter daltonii* sp. nov., an Fe(III)- and uranium(VI)-reducing bacterium isolated from a shallow subsurface exposed to mixed heavy metal and hydrocarbon contamination. Int J Syst Evol Microbiol. 2010;60(3):546–53.
128. Sung Y, Fletcher KE, Ritalahti KM, Apkarian RP, Ramos-Hernández N, Sanford RA, et al. *Geobacter lovleyi* sp. nov. strain SZ, a novel metal-reducing and tetrachloroethene-dechlorinating bacterium. Appl Environ Microbiol. 2006;72(4):2775–82.
129. De Wever H, Cole JR, Fettig MR, Hogan DA, Tiedje JM. Reductive dehalogenation of trichloroacetic acid by *Trichlorobacter thiogenes* gen. nov., sp. nov. Appl Environ Microbiol. 2000;66(6):2297–301.
130. Nevin KP, Holmes DE, Woodard TL, Covalla SF, Lovley DR. Reclassification of *Trichlorobacter thiogenes* as *Geobacter thiogenes* comb. nov. Int J Syst Evol Microbiol. 2007;57(3):463–6.
131. Kunapuli U, Jahn MK, Lueders T, Geyer R, Heipieper HJ, Meckenstock RU. *Desulfitobacterium aromaticivorans* sp. nov. and *Geobacter toluenoxydans* sp. nov., iron-reducing bacteria capable of anaerobic degradation of monoaromatic hydrocarbons. Int J Syst Evol Microbiol. 2010;60(3):686–95.
132. Shelobolina ES, Vrionis HA, Findlay RH, Lovley DR. *Geobacter uraniireducens* sp. nov., isolated from subsurface sediment undergoing uranium bioremediation. Int J Syst Evol Microbiol. 2008;58(5):1075–8.
133. Snoeyenbos-West OL, Nevin KP, Anderson RT, Lovley DR. Enrichment of *Geobacter* species

in response to stimulation of Fe(III) reduction in sandy aquifer sediments. Microb Ecol. 2000;39(2):153–67.

134. Methé BA, Nelson KE, Eisen JA, Paulsen IT, Nelson W, Heidelberg JF, et al. Genome of *Geobacter sulfurreducens*: metal reduction in subsurface environments. Science (80-). 2003;302(5652):1967–9.
135. Santos TC, Silva MA, Morgado L, Dantas JM, Salgueiro CA. Diving into the redox properties of *Geobacter sulfurreducens* cytochromes: a model for extracellular electron transfer. Dalt Trans. 2015;44(20):9335–44.
136. Moss GP. Nomenclature of tetrapyrroles. Recommendations 1986 IUPAC-IUB Joint Commission on Biochemical Nomenclature (JCBN). Eur J Biochem. 1988;178(2):277–328.
137. Hughes MN, Poole RK. Metals and micro-organisms. London: Chapman and Hall; 1989.
138. Moore GR, Pettigrew GW. Cytochromes *c*: evolutionary, structural and physicochemical aspects. Berlin: Springer-Verlag; 1990.
139. Lehninger A, Nelson D, Cox M. Lehninger Principles of Biochemistry. 5th ed. Book. New York; New Delhi: W. H. Freeman; 2005.
140. Reedijk J. Nomenclature of electron-transfer proteins. Recommendations 1989. J Biol Chem. 1992;267(1):665–77.
141. Hederstedt L. Heme *a* biosynthesis. Biochim Biophys Acta - Bioenerg. 2012;1817(6):920–7.
142. Hartshorne S, Richardson DJ, Simon J. Multiple haem lyase genes indicate substrate specificity in cytochrome *c* biogenesis. Biochem Soc Trans. 2006;34(1):146–9.
143. Herbaud ML, Aubert C, Durand MC, Guerlesquin F, Thöny-Meyer L, Dolla A. *Escherichia coli* is able to produce heterologous tetraheme cytochrome c_3 when the *ccm* genes are co-expressed. Biochim Biophys Acta. 2000;1481(1):18–24.
144. Hartshorne RS, Kern M, Meyer B, Clarke TA, Karas M, Richardson DJ, et al. A dedicated haem lyase is required for the maturation of a novel bacterial cytochrome *c* with unconventional covalent haem binding. Mol Microbiol. 2007;64(4):1049–60.
145. Pettigrew GW, Moore GR. Cytochromes *c*: Biological aspects. Berlin: Springer Berlin Heidelberg; 1987.
146. Ambler RP. Sequence variability in bacterial cytochromes *c*. Biochim Biophys Acta. 1991;1058(1):42–7.
147. Timkovich R, Dickerson RE. The structure of *Paracoccus denitrificans* cytochrome c_{550}. J Biol Chem. 1976;251(13):4033–46.
148. Yamanaka T, Imai S. A cytochrome *cc'*-like haemoprotein isolated from *Azotobacter vinelandii*. Biochem Biophys Res Commun. 1972;46(1):150–4.
149. Van Beeumen J, Van Den Branden C, Tempst P, De Ley J. Cytochromes c_{556} from three genetic races of *Agrobacterium*. Purification and comparison of their properties. Eur J Biochem. 1980;107(2):475–83.
150. Coutinho IB, Xavier A V. Tetraheme cytochromes. Methods Enzymol. 1994;243:119–40.
151. Aragão D, Frazão C, Sieker L, Sheldrick GM, LeGall J, Carrondo MA. Structure of dimeric cytochrome c_3 from *Desulfovibrio gigas* at 1.2 A resolution. Acta Crystallogr D Biol Crystallogr.

2003;59(Pt 4):644–53.

152. Seeliger S, Cord-Ruwisch R, Schink B. A periplasmic and extracellular *c*-type cytochrome of *Geobacter sulfurreducens* acts as a ferric iron reductase and as an electron carrier to other acceptors or to partner bacteria. J Bacteriol. 1998;180(14):3686–91.
153. Lloyd JR, Leang C, Hodges Myerson AL, Coppi M V., Cuifo S, Methé B, et al. Biochemical and genetic characterization of PpcA, a periplasmic *c*-type cytochrome in *Geobacter sulfurreducens*. Biochem J. 2003;369(Pt 1):153–61.
154. Afkar E. Purification and characterization of triheme cytochrome c_7 from the metal-reducing bacterium, <i>Geobacter metallireducens</sub>. FEMS Microbiol Lett. 1999;175(2):205–10.
155. Assfalg M, Banci L, Bertini I, Bruschi M, Turano P. 800 MHz ^{1}H NMR solution structure refinement of oxidized cytochrome c_7 from *Desulfuromonas acetoxidans*. Eur J Biochem. 1998;256(2):261–70.
156. Michel H. Three-dimensional crystals of a membrane protein complex. The photosynthetic reaction centre from *Rhodopseudomonas viridis*. J Mol Biol. 1982;158(3):567–72.
157. Stevens JM, Mavridou DAI, Hamer R, Kritsiligkou P, Goddard AD, Ferguson SJ. Cytochrome *c* biogenesis System I. FEBS J. 2011;278(22):4170–8.
158. Kranz RG, Richard-Fogal C, Taylor J-S, Frawley ER. Cytochrome *c* biogenesis: mechanisms for covalent modifications and trafficking of heme and for heme-iron redox control. Microbiol Mol Biol Rev. 2009;73(3):510–28.
159. Thöny-Meyer L, Fischer F, Künzler P, Ritz D, Hennecke H. *Escherichia coli* genes required for cytochrome *c* maturation. J Bacteriol. 1995;177(15):4321–6.
160. Simon J, Hederstedt L. Composition and function of cytochrome *c* biogenesis System II. FEBS J. 2011;278(22):4179–88.
161. Arslan E, Schulz H, Zufferey R, Künzler P, Thöny-Meyer L. Overproduction of the *Bradyrhizobium japonicum c*-type cytochrome subunits of the cbb_3 oxidase in *Escherichia coli*. Biochem Biophys Res Commun. 1998;251(3):744–7.
162. Feissner RE, Richard-Fogal CL, Frawley ER, Kranz RG. ABC transporter-mediated release of a haem chaperone allows cytochrome *c* biogenesis. Mol Microbiol. 2006;61(1):219–31.
163. Verissimo AF, Daldal F. Cytochrome *c* biogenesis System I: an intricate process catalyzed by a maturase supercomplex? Biochim Biophys Acta. 2014;1837(7):989–98.
164. van Wely KH, Swaving J, Freudl R, Driessen AJ. Translocation of proteins across the cell envelope of Gram-positive bacteria. FEMS Microbiol Rev. 2001;25(4):437–54.
165. Low KO, Muhammad Mahadi N, Md Illias R. Optimisation of signal peptide for recombinant protein secretion in bacterial hosts. Appl Microbiol Biotechnol. 2013;97(9):3811–26.
166. Auclair SM, Bhanu MK, Kendall DA. Signal peptidase I: cleaving the way to mature proteins. Protein Sci. 2012;21(1):13–25.
167. Natale P, Brüser T, Driessen AJM. Sec- and Tat-mediated protein secretion across the bacterial cytoplasmic membrane - Distinct translocases and mechanisms. Biochim Biophys Acta. 2008;1778(9):1735–56.
168. Liu Y, Wang Z, Liu J, Levar C, Edwards MJ, Babauta JT, et al. A trans-outer membrane porin-

cytochrome protein complex for extracellular electron transfer by *Geobacter sulfurreducens* PCA. Environ Microbiol Rep. 2014;6(6):776–85.

169. Marsili E, Rollefson JB, Baron DB, Hozalski RM, Bond DR. Microbial biofilm voltammetry: direct electrochemical characterization of catalytic electrode-attached biofilms. Appl Environ Microbiol. 2008;74(23):7329–37.
170. Yoho RA, Popat SC, Torres CI. Dynamic potential-dependent electron transport pathway shifts in anode biofilms of *Geobacter sulfurreducens*. ChemSusChem. 2014;7(12):3413–9.
171. Zacharoff L, Chan CH, Bond DR. Reduction of low potential electron acceptors requires the CbcL inner membrane cytochrome of *Geobacter sulfurreducens*. Bioelectrochemistry. 2016;107:7–13.
172. Levar CE, Chan CH, Mehta-Kolte MG, Bond DR. An inner membrane cytochrome required only for reduction of high redox potential extracellular electron acceptors. MBio. 2014;5(6):e02034-14.
173. Leang C, Coppi M V., Lovley DR. OmcB, a *c*-type polyheme cytochrome, involved in Fe(III) reduction in *Geobacter sulfurreducens*. J Bacteriol. 2003;185(7):2096–103.
174. Stephen CS, LaBelle E V., Brantley SL, Bond DR. Abundance of the multiheme *c*-type cytochrome OmcB increases in outer biofilm layers of electrode-grown *Geobacter sulfurreducens*. PLoS One. 2014;9(8):e104336.
175. Kim B-C, Lovley DR. Investigation of direct vs. indirect involvement of the *c* -type cytochrome MacA in Fe(III) reduction by *Geobacter sulfurreducens*. FEMS Microbiol Lett. 2008;286(1):39–44.
176. Seidel J, Hoffmann M, Ellis KE, Seidel A, Spatzal T, Gerhardt S, et al. MacA is a second cytochrome *c* peroxidase of *Geobacter sulfurreducens*. Biochemistry. 2012;51(13):2747–56.
177. Aklujkar M, Coppi M V., Leang C, Kim B-C, Chavan MA, Perpetua LA, et al. Proteins involved in electron transfer to Fe(III) and Mn(IV) oxides by *Geobacter sulfurreducens* and *Geobacter uraniireducens*. Microbiology. 2013;159(Pt_3):515–35.
178. Dantas JM, Brausemann A, Einsle O, Salgueiro CA. NMR studies of the interaction between inner membrane-associated and periplasmic cytochromes from *Geobacter sulfurreducens*. FEBS Lett. 2017;591(12):1657–66.
179. Ding Y-HR, Hixson KK, Aklujkar MA, Lipton MS, Smith RD, Lovley DR, et al. Proteome of *Geobacter sulfurreducens* grown with Fe(III) oxide or Fe(III) citrate as the electron acceptor. Biochim Biophys Acta. 2008;1784(12):1935–41.
180. Qian X, Reguera G, Mester T, Lovley DR. Evidence that OmcB and OmpB of *Geobacter sulfurreducens* are outer membrane surface proteins. FEMS Microbiol Lett. 2007;277(1):21–7.
181. Liu Y, Fredrickson JK, Zachara JM, Shi L. Direct involvement of *ombB*, *omaB*, and *omcB* genes in extracellular reduction of Fe(III) by *Geobacter sulfurreducens* PCA. Front Microbiol. 2015;6:1075.
182. Ding Y-HR, Hixson KK, Giometti CS, Stanley A, Esteve-Núñez A, Khare T, et al. The proteome of dissimilatory metal-reducing microorganism *Geobacter sulfurreducens* under various growth conditions. Biochim Biophys Acta. 2006;1764(7):1198–206.

183. Shelobolina ES, Coppi M V., Korenevsky AA, DiDonato LN, Sullivan SA, Konishi H, et al. Importance of c-type cytochromes for U(VI) reduction by *Geobacter sulfurreducens*. BMC Microbiol. 2007;7:16.
184. Mehta T, Coppi M V., Childers SE, Lovley DR. Outer membrane *c*-type cytochromes required for Fe(III) and Mn(IV) oxide reduction in *Geobacter sulfurreducens*. Appl Environ Microbiol. 2005;71(12):8634–41.
185. Inoue K, Leang C, Franks AE, Woodard TL, Nevin KP, Lovley DR. Specific localization of the *c*-type cytochrome OmcZ at the anode surface in current-producing biofilms of *Geobacter sulfurreducens*. Environ Microbiol Rep. 2011;3(2):211–7.
186. Nevin KP, Kim B-C, Glaven RH, Johnson JP, Woodard TL, Methé BA, et al. Anode biofilm transcriptomics reveals outer surface components essential for high density current production in *Geobacter sulfurreducens* fuel cells. PLoS One. 2009;4(5):e5628.
187. Reguera G, McCarthy KD, Mehta T, Nicoll JS, Tuominen MT, Lovley DR. Extracellular electron transfer via microbial nanowires. Nature. 2005;435(7045):1098–101.
188. Wang F, Gu Y, O'Brien JP, Yi SM, Yalcin SE, Srikanth V, et al. Structure of microbial nanowires reveals stacked hemes that transport electrons over micrometers. Cell. 2019;177(2):361-369.e10.
189. Shi L, Fredrickson JK, Zachara JM. Genomic analyses of bacterial porin-cytochrome gene clusters. Front Microbiol. 2014;5:1–10.
190. Morgado L, Bruix M, Pessanha M, Londer YY, Salgueiro CA. Thermodynamic characterization of a triheme cytochrome family from *Geobacter sulfurreducens* reveals mechanistic and functional diversity. Biophys J. 2010;99(1):293–301.
191. Pokkuluri PR, Londer YY, Duke NEC, Long WC, Schiffer M. Family of cytochrome c_7-type proteins from *Geobacter sulfurreducens*: structure of one cytochrome c_7 at 1.45 Å resolution. Biochemistry. 2004;43(4):849–59.
192. Pokkuluri PR, Londer YY, Duke NEC, Erickson J, Pessanha M, Salgueiro CA, et al. Structure of a novel c_7-type three-heme cytochrome domain from a multidomain cytochrome *c* polymer. Protein Sci. 2004;13(6):1684–92.
193. Bansal R, Helmus RA, Stanley BA, Zhu J, Liermann LJ, Brantley SL, et al. Survival during long-term starvation: global proteomics analysis of *Geobacter sulfurreducens* under prolonged electron-acceptor limitation. J Proteome Res. 2013;12(10):4316–26.
194. Londer YY, Pokkuluri PR, Orshonsky V, Orshonsky L, Schiffer M. Heterologous expression of dodecaheme "nanowire" cytochromes *c* from *Geobacter sulfurreducens*. Protein Expr Purif. 2006;47(1):241–8.
195. Pokkuluri PR, Londer YY, Duke NEC, Pessanha M, Yang X, Orshonsky V, et al. Structure of a novel dodecaheme cytochrome *c* from *Geobacter sulfurreducens* reveals an extended 12 nm protein with interacting hemes. J Struct Biol. 2011;174(1):223–33.
196. Londer YY, Pokkuluri PR, Erickson J, Orshonsky V, Schiffer M. Heterologous expression of hexaheme fragments of a multidomain cytochrome from *Geobacter sulfurreducens* representing a novel class of cytochromes *c*. Protein Expr Purif. 2005;39(2):254–60.

197. Morgado L, Fernandes AP, Londer YY, Pokkuluri PR, Schiffer M, Salgueiro CA. Thermodynamic characterization of the redox centres in a representative domain of a novel *c*-type multihaem cytochrome. Biochem J. 2009;420(3):485–92.
198. Edwards MJ, White GF, Norman M, Tome-Fernandez A, Ainsworth E, Shi L, et al. Redox linked flavin sites in extracellular decaheme proteins involved in microbe-mineral electron transfer. Sci Rep. 2015;5(1):11677.
199. Fonseca BM, Paquete CM, Neto SE, Pacheco I, Soares CM, Louro RO. Mind the gap: cytochrome interactions reveal electron pathways across the periplasm of *Shewanella oneidensis* MR-1. Biochem J. 2013;449(1):101–8.
200. Turner DL, Salgueiro CA, Catarino T, Legall J, Xavier A V. NMR studies of cooperativity in the tetrahaem cytochrome c_3 from *Desulfovibrio vulgaris*. Eur J Biochem. 1996;241(3):723–31.
201. Pessanha M, Brennan L, Xavier A V., Cuthbertson PM, Reid GA, Chapman SK, et al. NMR structure of the haem core of a novel tetrahaem cytochrome isolated from *Shewanella frigidimarina*: identification of the haem-specific axial ligands and order of oxidation. FEBS Lett. 2001;489(1):8–13.
202. Inoue K, Qian X, Morgado L, Kim B-C, Mester T, Izallalen M, et al. Purification and characterization of OmcZ, an outer-surface, octaheme *c*-type cytochrome essential for optimal current production by *Geobacter sulfurreducens*. Appl Environ Microbiol. 2010;76(12):3999–4007.
203. Catarino T, Turner DL. Thermodynamic control of electron transfer rates in multicentre redox proteins. ChemBioChem. 2001;2(6):416–24.
204. Keeler J. Understanding NMR spectroscopy. Wiley; 2005. 459 p.
205. Wüthrich K. NMR studies of structure and function of biological macromolecules (Nobel lecture). Angew Chemie Int Ed. 2003;42(29):3340–63.
206. Braun W, Bösch C, Brown LR, Go N, Wüthrich K. Combined use of proton-proton Overhauser enhancements and a distance geometry algorithm for determination of polypeptide conformations. Application to micelle-bound glucagon. Biochim Biophys Acta. 1981;667(2):377–96.
207. Orgel L. An introduction to transition-metal chemistry: ligand-field theory. London: Methuen; 1960.
208. Wüthrich K. NMR of proteins and nucleic acids. Wiley; 1986.
209. Bertini I, Luchinat C. NMR of paramagnetic molecules in biological systems. Menlo Park, Calif: Benjamin/Cummings Pub. Co.; 1986.
210. Wüthrich K. NMR in biological research: peptides and proteins. North-Holland Pub. Co.; 1976. 379 p.
211. Elantak L, Bornet O, Morelli X, Dolla A, Guerlesquin F. Sequential NMR assignment of the ferri-cytochrome c_3 from *Desulfovibrio vulgaris* Hildenborough. J Biomol NMR. 2002;23(1):69–70.
212. Santos H, Moura JJ, Moura I, LeGall J, Xavier A V. NMR studies of electron transfer mechanisms in a protein with interacting redox centres: *Desulfovibrio gigas* cytochrome c_3. Eur J Biochem. 1984;141(2):283–96.

213. Salgueiro CA, Turner DL, Santos H, LeGall J, Xavier A V. Assignment of the redox potentials to the four haems in *Desulfovibrio vulgaris* cytochrome c_3 by 2D-NMR. FEBS Lett. 1992;314(2):155–8.
214. Prudêncio M, Ubbink M. Transient complexes of redox proteins: structural and dynamic details from NMR studies. J Mol Recognit. 2004;17(6):524–39.
215. Mathews FS, Mauk AG, Moore GR. Protein-protein complexes formed by electron-transfer proteins. In: Kleanthous C, editor. Protein-protein recognition. New York: Oxford University Press; 2000. p. 60–101.
216. Bendall DS. Interprotein electron transfer. In: Bendall DS, editor. Protein Electron Transfer. Oxford: Bios Scientific; 1996. p. 43–64.
217. Crowley PB, Ubbink M. Close encounters of the transient kind: protein interactions in the photosynthetic redox chain investigated by NMR spectroscopy. Acc Chem Res. 2003;36(10):723–30.
218. Ubbink M. Dynamics in transient complexes of redox proteins. Biochem Soc Trans. 2012;40(2):415–8.
219. Fonseca BM, Paquete CM, Salgueiro CA. The role of intramolecular interactions in the functional control of multiheme cytochromes *c*. FEBS Lett. 2012;586(5):504–9.
220. Turner DL, Catarino T. Homotropic and heterotropic interactions in cytochromes c_3 from sulphate reducing bacteria. FEBS Lett. 2012;586(5):494–503.
221. Fernandes AP. Caracterização de um novo citocromo do tipo *c* que forma “nanofios” de hemos em *Geobacter sulfurreducens*. Faculdade de Ciências da Universidade de Lisboa; 2012.
222. Gordon EH, Steensma E, Ferguson SJ. The cytochrome *c* domain of dimeric cytochrome cd_1 of *Paracoccus pantotrophus* can be produced at high levels as a monomeric holoprotein using an improved *c*-type cytochrome expression system in *Escherichia coli*. Biochem Biophys Res Commun. 2001;281(3):788–94.
223. Turner DL, Salgueiro CA, LeGall J, Xavier A V. Structural studies of *Desulfovibrio vulgaris* ferrocytochrome c_3 by two-dimensional NMR. Eur J Biochem. 1992;210(3):931–6.
224. Pessanha M, Londer YY, Long WC, Erickson J, Pokkuluri PR, Schiffer M, et al. Redox characterization of *Geobacter sulfurreducens* cytochrome c_7: physiological relevance of the conserved residue F15 probed by site-specific mutagenesis. Biochemistry. 2004;43(30):9909–17.
225. McDonald CC, Phillips WD, Vinogradov SN. Proton magnetic resonance evidence for methionine-iron coordination in mammalian-type ferrocytochrome *c*. Biochem Biophys Res Commun. 1969;36(3):442–9.
226. Harada E, Fukuoka Y, Ohmura T, Fukunishi A, Kawai G, Fujiwara T, et al. Redox-coupled conformational alternations in cytochrome c_3 from *D. vulgaris* Miyazaki F on the basis of its reduced solution structure. J Mol Biol. 2002;319(3):767–78.
227. Harada E, Kumagai J, Ozawa K, Imabayashi S, Tsapin AS, Nealson KH, et al. A directional electron transfer regulator based on heme-chain architecture in the small tetraheme cytochrome *c* from *Shewanella oneidensis*. FEBS Lett. 2002;532(3):333–7.

228. Louro RO, Pacheco I, Turner DL, LeGall J, Xavier A V. Structural and functional characterization of cytochrome c_3 from *D. desulfuricans* ATCC 27774 by ^{1}H-NMR. FEBS Lett. 1996;390(1):59–62.
229. Piçarra-Pereira MA, Turner DL, LeGall J, Xavier A V. Structural studies on *Desulfovibrio gigas* cytochrome c_3 by two-dimensional ^{1}H-nuclear-magnetic-resonance spectroscopy. Biochem J. 1993;(Pt 3):909–15.
230. Coutinho IB, Turner DL, LeGall J, Xavier A V. Characterization of the structure and redox behaviour of cytochrome c_3 from *Desulfovibrio baculatus* by ^{1}H-nuclear magnetic resonance spectroscopy. Biochem J. 1993;294(3):899–908.
231. Pereira PM, Pacheco I, Turner DL, Louro RO. Structure-function relationship in type II cytochrome c_3 from *Desulfovibrio africanus*: a novel function in a familiar heme core. J Biol Inorg Chem. 2002;7(7–8):815–22.
232. Morgado L, Bruix M, Orshonsky V, Londer YY, Duke NEC, Yang X, et al. Structural insights into the modulation of the redox properties of two *Geobacter sulfurreducens* homologous triheme cytochromes. Biochim Biophys Acta. 2008;1777(9):1157–65.
233. Turner DL, Salgueiro CA, Schenkels P, LeGall J, Xavier A V. Carbon-13 NMR studies of the influence of axial ligand orientation on haem electronic structure. Biochim Biophys Acta - Protein Struct Mol Enzymol. 1995;1246(1):24–8.
234. Bolton JR, Fraenkel GK. Electron spin resonance study of the pairing theorem for alternant hydrocarbons: ^{13}C splittings in the anthracene positive and negative Ions. J Chem Phys. 1964;40(11):3307–20.
235. Sharma S, Cavallaro G, Rosato A. A systematic investigation of multiheme *c*-type cytochromes in prokaryotes. J Biol Inorg Chem. 2010;15(4):559–71.
236. Bertini I, Cavallaro G, Rosato A. Cytochrome *c*: occurrence and functions. Chem Rev. 2006;106(1):90–115.
237. Mowat CG, Chapman SK. Multi-heme cytochromes - new structures, new chemistry. Dalt Trans. 2005;302(21):3381–9.
238. Kletzin A, Heimerl T, Flechsler J, van Niftrik L, Rachel R, Klingl A. Cytochromes *c* in *Archaea*: distribution, maturation, cell architecture, and the special case of *Ignicoccus hospitalis*. Front Microbiol. 2015;6:439.
239. Pessanha M, Rothery EL, Miles CS, Reid GA, Chapman SK, Louro RO, et al. Tuning of functional heme reduction potentials in *Shewanella* fumarate reductases. Biochim Biophys Acta. 2009;1787(2):113–20.
240. Louro RO, Catarino T, LeGall J, Turner DL, Xavier A V. Cooperativity between electrons and protons in a monomeric cytochrome c_3: the importance of mechano-chemical coupling for energy transduction. ChemBioChem. 2001;2(11):831–7.
241. Liu J, Chakraborty S, Hosseinzadeh P, Yu Y, Tian S, Petrik I, et al. Metalloproteins containing cytochrome, iron-sulfur, or copper redox centers. Chem Rev. 2014;114(8):4366–469.
242. Breuer M, Rosso KM, Blumberger J, Butt JN. Multi-haem cytochromes in *Shewanella oneidensis* MR-1: structures, functions and opportunities. J R Soc Interface. 2015;12(102):20141117.

243. Schuetz B, Schicklberger M, Kuermann J, Spormann AM, Gescher J. Periplasmic electron transfer via the *c*-type cytochromes MtrA and FccA of *Shewanella oneidensis* MR-1. Appl Environ Microbiol. 2009;75(24):7789–96.
244. Paquete CM, Louro RO. Unveiling the details of electron transfer in multicenter redox proteins. Acc Chem Res. 2014;47(1):56–65.
245. Francis RT, Becker RR. Specific indication of hemoproteins in polyacrylamide gels using a double-staining process. Anal Biochem. 1984;136(2):509–14.
246. Paquete CM, Turner DL, Louro RO, Xavier A V., Catarino T. Thermodynamic and kinetic characterisation of individual haems in multicentre cytochromes c_3. Biochim Biophys Acta. 2007;1767(9):1169–79.
247. Dixon M. The acceptor specificity of flavins and flavoproteins. I. Techniques for anaerobic spectrophotometry. Biochim Biophys Acta. 1971;226(2):241–58.
248. Lambeth DO, Palmer G. The kinetics and mechanism of reduction of electron transfer proteins and other compounds of biological interest by dithionite. J Biol Chem. 1973;248(17):6095–103.
249. Neta P, Huie RE, Harriman A. One-electron-transfer reactions of the couple sulfur dioxide/sulfur dioxide radical anion in aqueous solutions. Pulse radiolytic and cyclic voltammetric studies. J Phys Chem. 1987;91(6):1606–11.
250. Louro RO, Catarino T, Paquete CM, Turner DL. Distance dependence of interactions between charged centres in proteins with common structural features. FEBS Lett. 2004;576(1–2):77–80.
251. Hückel E, Debye P. The theory of electrolytes: I. lowering of freezing point and related phenomena. Phys Z. 1923;24:185–206.
252. Marcus RA, Sutin N. Electron transfers in chemistry and biology. Biochim Biophys Acta. 1985;811(3):265–322.
253. Paquete CM, Saraiva IH, Calçada E, Louro RO. Molecular basis for directional electron transfer. J Biol Chem. 2010;285(14):10370–5.
254. Lagarias JC, Reeds JA, Wright MH, Wright PE. Convergence properties of the Nelder-Mead simplex method in low dimensions. SIAM J Optim. 1998;9(1):112–47.
255. Paquete CM, Louro RO. Molecular details of multielectron transfer: the case of multiheme cytochromes from metal respiring organisms. Dalt Trans. 2010;39(18):4259–66.
256. Fernandes AP, Alves MN, Salgueiro CA, Paquete CM. Unraveling the electron transfer processes of a nanowire protein from *Geobacter sulfurreducens*. Biochim Biophys Acta. 2016;1857(1):7–13.
257. Dantas JM, Morgado L, Aklujkar M, Bruix M, Londer YY, Schiffer M, et al. Rational engineering of *Geobacter sulfurreducens* electron transfer components: a foundation for building improved *Geobacter*-based bioelectrochemical technologies. Front Microbiol. 2015;6:752.
258. Pokkuluri PR, Londer YY, Yang X, Duke NEC, Erickson J, Orshonsky V, et al. Structural characterization of a family of cytochromes c_7 involved in Fe(III) respiration by *Geobacter sulfurreducens*. Biochim Biophys Acta. 2010;1797(2):222–32.
259. Morgado L, Dantas JM, Bruix M, Londer YY, Salgueiro CA. Fine tuning of redox networks on multiheme cytochromes from *Geobacter sulfurreducens* drives physiological electron/proton

energy transduction. Bioinorg Chem Appl. 2012;2012(298739):1–9.

260. Martínez-Fábregas J, Díaz-Moreno I, González-Arzola K, Janocha S, Navarro JA, Hervás M, et al. Structural and functional analysis of novel human cytochrome *c* targets in apoptosis. Mol Cell Proteomics. 2014;13(6):1439–56.

261. Martínez-Fábregas J, Díaz-Moreno I, González-Arzola K, Janocha S, Navarro JA, Hervás M, et al. New *Arabidopsis thaliana* cytochrome *c* partners: a look into the elusive role of cytochrome *c* in programmed cell death in plants. Mol Cell Proteomics. 2013;12(12):3666–76.

262. Studier FW, Moffatt BA. Use of bacteriophage T7 RNA polymerase to direct selective high-level expression of cloned genes. J Mol Biol. 1986;189(1):113–30.

263. Yanisch-Perron C, Vieira J, Messing J. Improved M13 phage cloning vectors and host strains: nucleotide sequences of the M13mp18 and pUC19 vectors. Gene. 1985;33(1):103–19.

264. Iobbi-Nivol C, Crooke H, Griffiths L, Grove J, Hussain H, Pommier J, et al. A reassessment of the range of *c*-type cytochromes synthesized by *Escherichia coli* K-12. FEMS Microbiol Lett. 1994;119(1–2):89–94.

265. Venkateswaran K, Moser DP, Dollhopf ME, Lies DP, Saffarini DA, MacGregor BJ, et al. Polyphasic taxonomy of the genus *Shewanella* and description of *Shewanella oneidensis* sp. nov. Int J Syst Bacteriol. 1999;49(2):705–24.

266. Sambrook J, Russell DW. Molecular cloning: a laboratory manual. 3rd ed. New York: Cold Spring Harbor Laboratory Press; 2001.

267. Shi L, Lin J-T, Markillie LM, Squier TC, Hooker BS. Overexpression of multi-heme *c*-type cytochromes. Biotechniques. 2005;38(2):297–9.

268. Costa NL, Carlson HK, Coates JD, Louro RO, Paquete CM. Heterologous expression and purification of a multiheme cytochrome from a Gram-positive bacterium capable of performing extracellular respiration. Protein Expr Purif. 2015;111:48–52.

269. Londer YY, Pokkuluri PR, Tiede DM, Schiffer M. Production and preliminary characterization of a recombinant triheme cytochrome c_7 from *Geobacter sulfurreducens* in *Escherichia coli*. Biochim Biophys Acta. 2002;1554(3):202–11.

270. Díaz-Moreno I, Díaz-Quintana A, Ubbink M, De la Rosa MA. An NMR-based docking model for the physiological transient complex between cytochrome f and cytochrome c_6. FEBS Lett. 2005;579(13):2891–6.

271. Worrall JA, Reinle W, Bernhardt R, Ubbink M. Transient protein interactions studied by NMR spectroscopy: the case of cytochrome *c* and adrenodoxin. Biochemistry. 2003;42(23):7068–76.

272. Lasdon LS, Waren AD. Generalized reduced gradient software for linearly and nonlinearly constrained problems. In: Greenberg HJ, editor. Design and Implementation of Optimization Software. Sijthoff and Noordhoff; 1978. p. 335–62.

273. Meyer TE, Tsapin AI, Vandenberghe I, de Smet L, Frishman D, Nealson KH, et al. Identification of 42 possible cytochrome *c* genes in the *Shewanella oneidensis* genome and characterization of six soluble cytochromes. OMICS. 2004;8(1):57–77.

274. Takayama Y, Akutsu H. Expression in periplasmic space of *Shewanella oneidensis*. Protein Expr Purif. 2007;56(1):80–4.

275. Bashir Q, Scanu S, Ubbink M. Dynamics in electron transfer protein complexes. FEBS J. 2011;278(9):1391–400.
276. Liu Z, Gong Z, Dong X, Tang C. Transient protein-protein interactions visualized by solution NMR. Biochim Biophys Acta. 2016;1864(1):115–22.
277. Fernandes AP, Turner DL, Salgueiro C. A biochemical LEGO® strategy to unveil the functional properties of 'nanowire' cytochromes. 2017.
278. Zuiderweg ERP. Mapping protein-protein interactions in solution by NMR spectroscopy. Biochemistry. 2002;41(1):1–7.
279. Malvankar NS, Vargas M, Nevin KP, Franks AE, Leang C, Kim B-C, et al. Tunable metallic-like conductivity in microbial nanowire networks. Nat Nanotechnol. 2011;6(9):573–9.
280. García-Heredia JM, Díaz-Moreno I, Díaz-Quintana A, Orzáez M, Navarro JA, Hervás M, et al. Specific nitration of tyrosines 46 and 48 makes cytochrome *c* assemble a non-functional apoptosome. FEBS Lett. 2012;586(2):154–8.
281. Ly HK, Utesch T, Díaz-Moreno I, García-Heredia JM, De La Rosa MA, Hildebrandt P. Perturbation of the redox site structure of cytochrome *c* variants upon tyrosine nitration. J Phys Chem B. 2012;116(19):5694–702.
282. García-Heredia JM, Díaz-Moreno I, Nieto PM, Orzáez M, Kocanis S, Teixeira M, et al. Nitration of tyrosine 74 prevents human cytochrome *c* to play a key role in apoptosis signaling by blocking caspase-9 activation. Biochim Biophys Acta. 2010;1797(6):981–93.
283. Rodríguez-Roldán V, García-Heredia JM, Navarro JA, De la Rosa MA, Hervás M. Effect of nitration on the physicochemical and kinetic features of wild-type and monotyrosine mutants of human respiratory cytochrome *c*. Biochemistry. 2008;47(47):12371–9.
284. Anraku Y. Bacterial electron transport chains. Annu Rev Biochem. 1988;57(1):101–32.
285. Kato S. Biotechnological aspects of microbial extracellular electron transfer. Microbes Environ. 2015;30(2):133–9.
286. Dulon S, Parot S, Delia M-L, Bergel A. Electroactive biofilms: new means for electrochemistry. J Appl Electrochem. 2006;37(1):173–9.
287. Cao X, Huang X, Liang P, Xiao K, Zhou Y, Zhang X, et al. A new method for water desalination using microbial desalination cells. Environ Sci Technol. 2009;43(18):7148–52.
288. Jacobson KS, Drew DM, He Z. Use of a liter-scale microbial desalination cell as a platform to study bioelectrochemical desalination with salt solution or artificial seawater. Environ Sci Technol. 2011;45(10):4652–7.
289. Luo H, Xu P, Roane TM, Jenkins PE, Ren Z. Microbial desalination cells for improved performance in wastewater treatment, electricity production, and desalination. Bioresour Technol. 2012;105:60–6.
290. Luo H, Jenkins PE, Ren Z. Concurrent desalination and hydrogen generation using microbial electrolysis and desalination cells. Environ Sci Technol. 2011;45(1):340–4.
291. Mehanna M, Kiely PD, Call DF, Logan BE. Microbial electrodialysis cell for simultaneous water desalination and hydrogen gas production. Environ Sci Technol. 2010;44(24):9578–83.
292. Cheng S, Xing D, Call DF, Logan BE. Direct biological conversion of electrical current into

methane by electromethanogenesis. Environ Sci Technol. 2009;43(10):3953–8.
293. Liu H, Hu H, Chignell J, Fan Y. Microbial electrolysis: novel technology for hydrogen production from biomass. Biofuels. 2010;1(1):129–42.
294. Logan BE, Call D, Cheng S, Hamelers HVM, Sleutels THJA, Jeremiasse AW, et al. Microbial electrolysis cells for high yield hydrogen gas production from organic matter. Environ Sci Technol. 2008;42(23):8630–40.
295. Gregory KB, Lovley DR. Remediation and recovery of uranium from contaminated subsurface environments with electrodes. Environ Sci Technol. 2005;39(22):8943–7.
296. Lovley DR, Nevin KP. A shift in the current: new applications and concepts for microbe-electrode electron exchange. Curr Opin Biotechnol. 2011;22(3):441–8.
297. Aulenta F, Canosa A, Majone M, Panero S, Reale P, Rossetti S. Trichloroethene dechlorination and H_2 evolution are alternative biological pathways of electric charge utilization by a dechlorinating culture in a bioelectrochemical system. Environ Sci Technol. 2008;42(16):6185–90.
298. Butler CS, Clauwaert P, Green SJ, Verstraete W, Nerenberg R. Bioelectrochemical perchlorate reduction in a microbial fuel cell. Environ Sci Technol. 2010;44(12):4685–91.
299. Fornero JJ, Rosenbaum M, Angenent LT. Electric power generation from municipal, food, and animal wastewaters using microbial fuel cells. Electroanalysis. 2010;22(7-8):832–43.
300. Liu H, Logan BE. Electricity generation using an air-cathode single chamber microbial fuel cell in the presence and absence of a proton exchange membrane. Environ Sci Technol. 2004;38(14):4040–6.
301. Ren Z, Ward TE, Regan JM. Electricity production from cellulose in a microbial fuel cell using a defined binary culture. Environ Sci Technol. 2007;41(13):4781–6.
302. Armaroli N, Balzani V. The hydrogen issue. ChemSusChem. 2011;4(1):21–36.
303. Obi CN, Asogwa GC. Electromicrobiology: an emerging reality – a review. OALib. 2015;02(11):1–10.
304. Anderson RT, Vrionis HA, Ortiz-Bernad I, Resch CT, Long PE, Dayvault R, et al. Stimulating the *in situ* activity of *Geobacter* species to remove uranium from the groundwater of a uranium-contaminated aquifer. Appl Environ Microbiol. 2003;69(10):5884–91.
305. Cologgi DL, Speers AM, Bullard BA, Kelly SD, Reguera G. Enhanced uranium immobilization and reduction by *Geobacter sulfurreducens* biofilms. Appl Environ Microbiol. 2014;80(21):6638–46.
306. Griffin BA, Adams SR, Tsien RY. Specific covalent labeling of recombinant protein molecules inside live cells. Science (80-). 1998;281(5374):269–72.
307. Hoffmann C, Gaietta G, Zürn A, Adams SR, Terrillon S, Ellisman MH, et al. Fluorescent labeling of tetracysteine-tagged proteins in intact cells. Nat Protoc. 2010;5(10):1666–77.
308. Cheng C, Shuman S. Recombinogenic flap ligation pathway for intrinsic repair of topoisomerase IB-induced double-strand breaks. Mol Cell Biol. 2000;20(21):8059–68.
309. Guzman LM, Belin D, Carson MJ, Beckwith J. Tight regulation, modulation, and high-level expression by vectors containing the arabinose PBAD promoter. J Bacteriol.

1995;177(14):4121–30.

310. Tsapin AI, Vandenberghe I, Nealson KH, Scott JH, Meyer TE, Cusanovich MA, et al. Identification of a small tetraheme cytochrome *c* and a flavocytochrome *c* as two of the principal soluble cytochromes *c* in *Shewanella oneidensis* strain MR-1. Appl Environ Microbiol. 2001;67(7):3236–44.
311. Meuskens I, Michalik M, Chauhan N, Linke D, Leo JC. A new strain collection for improved expression of outer membrane proteins. Front Cell Infect Microbiol. 2017;7:464.
312. Pokkuluri PR, Londer YY, Wood SJ, Duke NEC, Morgado L, Salgueiro CA, et al. Outer membrane cytochrome *c*, OmcF, from *Geobacter sulfurreducens*: high structural similarity to an algal cytochrome c_6. Proteins. 2009;74(1):266–70.
313. Lovley DR. Bug juice: harvesting electricity with microorganisms. Nat Rev. 2006;4(7):497–508.
314. Lloyd JR, Lovley DR. Microbial detoxification of metals and radionuclides. Curr Opin Biotechnol. 2001;12(3):248–53.
315. Rooney-Varga JN, Anderson RT, Fraga JL, Ringelberg D, Lovley DR. Microbial communities associated with anaerobic benzene degradation in a petroleum-contaminated aquifer. Appl Environ Microbiol. 1999;65(7):3056–63.
316. Lee K-Y, Bosch J, Meckenstock RU. Use of metal-reducing bacteria for bioremediation of soil contaminated with mixed organic and inorganic pollutants. Environ Geochem Health. 2012;34 Suppl 1:135–42.
317. Rosano GL, Ceccarelli EA. Recombinant protein expression in *Escherichia coli*: advances and challenges. Front Microbiol. 2014;5:172.
318. Keiler KC, Sauer RT. Sequence determinants of C-terminal substrate recognition by the Tsp protease. J Biol Chem. 1996;271(5):2589–93.
319. Mavridou DAI, Ferguson SJ, Stevens JM. Cytochrome *c* assembly. IUBMB Life. 2013;65(3):209–16.
320. Pettersen EF, Goddard TD, Huang CC, Couch GS, Greenblatt DM, Meng EC, et al. UCSF Chimera - a visualization system for exploratory research and analysis. J Comput Chem. 2004;25(13):1605–12.
321. Berman HM, Westbrook J, Feng Z, Gilliland G, Bhat TN, Weissig H, et al. The Protein Data Bank. Nucleic Acids Res. 2000;28(1):235–42.
322. Skoog DA, Holler FJ, Nieman TA. Principles of instrumental analysis. 5th ed. Saunders College Pub.; 1998.
323. Koradi R, Billeter M, Wüthrich K. MOLMOL: a program for display and analysis of macromolecular structures. J Mol Graph. 1996;14(1):51–5.
324. Dantas JM, Morgado L, Catarino T, Kokhan O, Pokkuluri PR, Salgueiro CA. Evidence for interaction between the triheme cytochrome PpcA from *Geobacter sulfurreducens* and anthrahydroquinone-2,6-disulfonate, an analog of the redox active components of humic substances. Biochim Biophys Acta. 2014;1837(6):750–60.
325. Morgado L, Bruix M, Pokkuluri PR, Salgueiro CAS, Turner DL. Redox- and pH-linked conformational changes in triheme cytochrome PpcA from *Geobacter sulfurreducens*. Biochem

J. 2017;474(2):231–46.